EXPERIMENTAL INVESTIGATION ON THE DYNAMICS OF INFLATABLE DAMS

by

Thoukidides A. Economides

Dissertation submitted to the Faculty of the
Virginia Polytechnic Institute and State University
in partial fulfillment of the requirements for the degree of
Doctor of Philosophy
in
Civil Engineering

APPROVED:

D. A. Walker, co-chairman
Engineering Science and Mechanics Dept.

R. H. Plaut, co-chairman
Civil Engineering Department

R. M. Barker
Civil Engineering Department

P. Diplas
Civil Engineering Department

D. P. Telionis
Engineering Science and Mechanics Dept.

S. Liapis
Aerospace and Ocean Engineering Dept.

October, 1993
Blacksburg, Virginia

EXPERIMENTAL INVESTIGATION OF THE DYNAMICS OF INFLATABLE DAMS

by

Thoukidides A. Economides

Committee chairman: Dana A. Walker, co-chairman
Department of Engineering Science and Mechanics
and
Raymond H. Plaut, co-chairman
The Charles Edward Via, Jr., Department of Civil Engineering

(ABSTRACT)

The dynamic characteristics of pressurized cylindrical membranes used as dams are considered here. Single-anchored air-inflated membranes are predominantly studied. Load-combinations are considered without any water, with impounding water, and with water overflow. The two major experimental variables are the dam's internal pressure and the stream's flow rate or the impounded water height. The existence of upstream water is shown to completely change the dynamic characteristics of the membrane-dam, now a structure-fluid system. Two aspect ratios are considered with the same height, at two separate open-channel facilities. The material used is modeled as an inextensible weightless membrane without any bending stiffness. It is shown that the ratio between the internal pressure head and the upstream water head, identified as the "pressure ratio", is the major controlling parameter. During overflow conditions, the pressure ratio is shown to have a critical value where the energy of vibration maximizes. In addition, the ratio of the upstream water head to the dam's height, identified as the "load ratio", is non-linearly proportional to the vibration's energy level. Both the pressure ratio and the load ratio are shown to be dependent on the model's aspect ratio. The pressure ratio is slightly non-linearly proportional to the natural frequencies of the system, while the load ratio is inversely proportional. Up-scaling of the results follows the Froude law. The source of vibrations either in the form of a driving force or a perturbation force is identified to be at the downstream base of the dam.

to my daughter

Eva Athena

Acknowledgements

My sincere appreciation to Dr. Walker and Dr. Plaut for their support and advice throughout the course of this work. Dr. Plaut's expertise on inflatable dams and dynamics, and his enormous patience in many ways but especially throughout the writing of the dissertation, made the completion of this work possible. Dr. Walker's guidance in the experimental fluid mechanics and the instrumentation science, made this work a reality and gave me a knowledge to cherish for years to come. I am grateful to Dr. Telionis for his advice and support. My gratitude to Dr. Barker whose suggestions further improved this work, to Dr. Diplas for his advice and the many hours he spent with me, and to Dr. Liapis for his suggestions and encouragement. The research grant from the National Science Foundation, No. MSM-9008518, is also acknowledged. I would also like to thank the following for their help: Dr. Rediniotis and Mr. Bob Simonds in the Department of Engineering Science and Mechanics, Mr. Billy Williams in the Chemical Engineering Department, Dr. Cox and Dr. de la Garza in the Civil Engineering Department (Hydrosystems and Construction divisions, respectively). Mr. E. R. Richmond of the Du Pont Polymers company provided the Mylar^{R} film material used during this work.

The inflatable dam industry provided ample information, although this work did not model an individual dam. Particularly, I would like to thank the Bridgestone Engineered Products Company, the Rodney Hunt Company, and the N. M. Imbertson and Associates.

My family and especially my wife deserves most of the credit as without her loving support what is presented here would not have been possible. Finally, it is the unconditional encouragement and support of my parents, Mr. and Mrs. Andreas and Nona Economides, that brought me to this position today. My deepest appreciation and respect goes to them, and I only hope that with His help, my wife and I will be able to offer our children as much as they did.

Preface

Inflatable dams have been in existence for less than 40 years. They received a global interest as a cheaper, thus marketable, alternative to other flow control structures. They attracted the attention of the engineering community because of the ingenuity of their concept and because of their initial problems. Given the attention this subject has already received, a question may arise regarding the need for the work presented here.

There are good reasons for predicting the dynamic behavior of hydraulic structures in general. As it is with conventional structures, excessive vibrations may threaten the structure itself and in turn its environment. Particularly for an inflatable dam used as a reservoir, its collapse may endanger lives and create property damage. If the conditions which lead to uncontrollable behavior are known, then design modifications may prevent a disaster. Moreover, in structures of this type vibrations may occur at "extreme" conditions, and there may be little or no time at all to react. Flow induced vibrations may be controlled by reshaping the structure (streamlining), but in this case there is not much of a choice. Instead, relocation of the flow separation point, which is likely to have a very important role in the dam's vibrations, is a good possibility. Also, the application of mechanical/hydraulic damping or active control are viable solution options.

Although a considerable amount of research has already been done, only a small portion of the published reports deal with experimental work. Since the first dam was introduced, their response to static loads was within predictable limits. Not much to be said about their static conditions, the attention is focused on their dynamic behavior. Thirty-five years ago, as well as today's inflatable dams, exhibit cases of undesirable behavior. Unlike other conventional structures but like most hydrodynamic structures, prototype tests cannot be carried out. This is primarily due to the lack of extreme cases like high overflows at will. It is therefore desirable to provide the

necessary information through model tests. There are limitations in solving this type of problem with only an analytical approach, which can be overcome with experimental input.

Empirical relations through experiments are consequently required and they are subsequently the next logical step. Previous experimental work is limited to observations on prototype failures and some model tests. Most of the tests were carried out during the sixties and early seventies, times when the inflatable dam industry was hindered by dam failures. Justified by the technology of that time, instrumentation practice may been interfered either with the water flow or with the model's structural characteristics. Moreover, measurements were not reportedly logged as digital (or analog) data in a form useful for post-processing, but instead they were logged as averages in the time domain. The need for new tests remains not only to repeat some of the previous experiments, but most importantly to offer new insights.

The first chapter gives an introduction on inflatable dams, a historical brief and statistics, their problems and an account of the work done by other workers. The second chapter describes the theoretical and practical aspects of modelling in this particular problem. This chapter includes many details so that future workers will have a good reference of the abilities and limitations of this work. Original instrumentation work is presented in some detail in Chapter Three. Included is an account of the measurement error through the various measurement techniques. Free vibration results are presented in Chapter Four as the dam model's response under impact excitation and various upstream water heights. Flow-induced response is presented in the fifth chapter for several flow rates. The results from two experimental facilities are also compared. Conclusions are summarized in Chapter Six.

Table of Contents

List of Figures

List of Tables

Chapter One

INFLATABLE DAMS

Inflatable dams represent a relatively new type of structure. They are an application of the more general category of air-supported membrane structures. It is because of their application as dams that they present difficulties in analysis that sometimes result in oversimplification. Historically, they have been used conservatively in a large part of the industrialized world. The idea of an inflatable bag retaining 5 meters (16.4 feet) of water is not welcomed at the beginning. This chapter puts in perspective the nature, the function, and the problems associated with inflatable dams.

1.1 Concept

The simplicity of inflatable dams' design is what makes them so attractive as fluid containment structures. They are inflated cylindrical membranes, length-wise attached on a foundation strip. In general, they are used as low-rise dams, not exceeding a six meters (20 feet) height. This cylindrical membrane can be inflated with air, filled with water, or pressurized with a combination of air and water. It may be anchored to a specifically made reinforced-concrete foundation strip, or an existing base, like the crest of a dam.

Anchorage may have the form of a single or double strip system. The double anchorage system results in a more stable dam, but is also more expensive. The sides of the dam may be attached to vertical or inclined abutments, according to the cross sectional shape of the stream. Many length (L) to height (H) ratio variations have already been installed, ranging from L/H=0.5

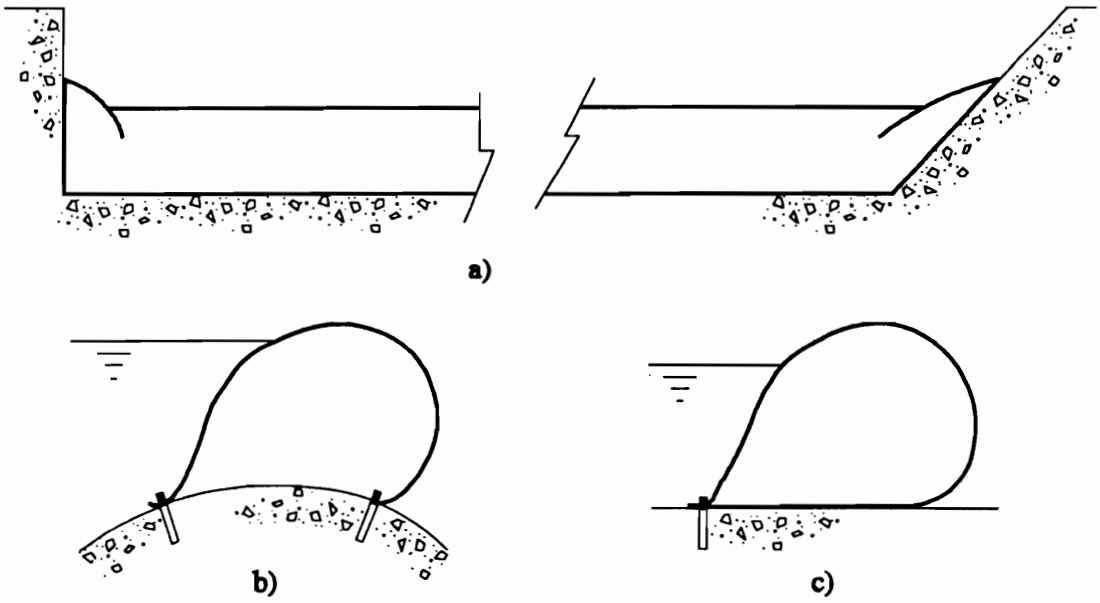

Figure 1.1 Typical inflatable dam: a) Longitudinal section with vertical (left) and inclined abutment (right); b) Cross section on a curved base (weir's crest) with double anchorage method; c) Single anchorage method.

to 229. A typical inflatable dam layout is shown in Figure 1.1.

Practical applications of this design are limited to conditions where there is little or no overflow. High overflows are associated with large-displacement oscillations and danger of failure of the structure. It is a common practice (when application permits) to partially or completely deflate the dam when an upstream surge is expected. These actions help to avoid upstream flooding and failure of the dam itself.

Structural behavior of inflatable dams is governed by the membrane's material characteristics, the upstream velocity (if any), and internal pressure. Although it is estimated that more than 2,000 dams are installed worldwide (approximately 78 in the U.S., 1990), design guidelines are very limited or not existing. This is primarily due to the competition between designers/manufacturers. This competition also generated variations of the basic principles about the material, the anchorage device and the vibration control method.

1.2 Construction

Construction simplicity is a major characteristic of inflatable dams. It allows them to be erected relatively fast. In fact, most of the construction time is taken by the concrete curing period,

while the actual material installation (nylon-reinforced rubber sheet) takes only a few days.

There are two types of anchorage systems. The first (original and improved versions) clamps the end(s) between and around one or two bars, providing a firm grip (Figure 1.2a). The other provides a combination of friction and shear resistance, with the anchorage bolts passing through the material and pressurized by two corrugated plates (Figure 1.2b). Disadvantages of the latter include required periodical re-tightening of anchorage bolts and probably extra reinforcement around the holes due to stress concentrations.

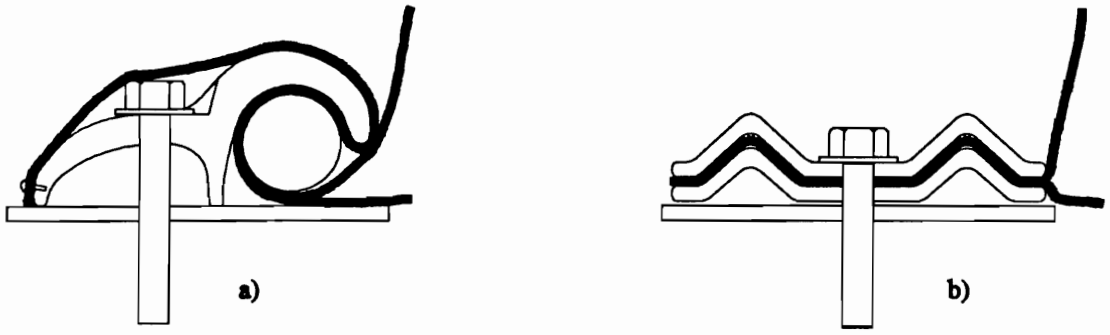

Figure 1.2 a) The clamping anchorage system concept. b) The friction and shear combination anchorage system concept.

The length of a continuous dam is only limited by the weight capacity of the carrier line (trucks, cranes, etc.). Rolled in massive spools during manufacturing, the membrane material can have unlimited length. At the construction site, the reinforced rubber-sheet spool is held by a crane and is unrolled on a suitable foundation strip. In case the project requires the installation of a very long dam, this is done in segments with intermediate piers. The longest single-span dam ever built is 125 meters (410 feet) long, 0.6 meters (1.96 feet) high, and was installed in Thailand by Bridgestone on the crest of a weir in 1985.

Maximum dam height is limited by the dynamic response of the structure. It is evident that design firms are reluctant to provide dams exceeding a twenty foot height, without special restraining systems (none was ever reported installed). Height may also be limited by the manufacturing process of the raw material, due to the maximum width capacity of the manufacturing equipment. For example, a 6 meter (19.6 feet) high dam will require roughly a $2\pi R$ wide material, which equals to 18.8 meters (61.7 feet).

Single or double anchorage practice is governed by the particular application and the size of the dam. Unless there are concerns about the stability of the structure, single anchorage is now

predominantly used because it is much cheaper to install. Double anchorage is used in the case of a reversed stream flow. Single anchored dams may be used for small reversed overflows, but double anchoring forces the dam to behave the same regardless of the flow direction. Another case where double anchorage is used, is when the downstream water level is high enough to create instability problems due to buoyancy (assuming air inflation). This behavior is notable with a downstream water level as low as one-fifth of the dam's height ($0.2H$). The result can be restricted to small vibrations, but it may also lead to large amplitude oscillations.

Major improvements of the material characteristics have taken place since the first two decades (fifties and sixties) after the rubber dams were introduced. Most important of all is the improvement that came with the technological advances on rubberized materials. Material degradation, the most significant problem, is not of a primary concern any more. Its life expectancy is now more than fifty years. It is also advertised by one company that a combination of materials (e.g. a "Hypalon" rubber layer) results in an abrasive resistance ten times that of iron! Moreover, some companies introduced thicker materials with more layers of rubber and reinforcement. Another company uses a special manufacturing process to enclose cross-sectional seams for crosswise reinforcement. Even a ceramic coating (CE article [1], 1992) was introduced for protection against gunshots in hunting areas, and against vandalism.

1.3 Inflation Method

Air is the inflation medium predominantly used today. This represents 87% of the dams built from 1959 to 1992, or 95% of the dams built since 1985. Figure 1.3 shows that water inflation was almost abandoned in the eighties. Water is now used only occasionally when its advantages are more important than its disadvantages. Missing from the graph are records from Imbertson and Associates Inc. [9], which do not specify inflation method.

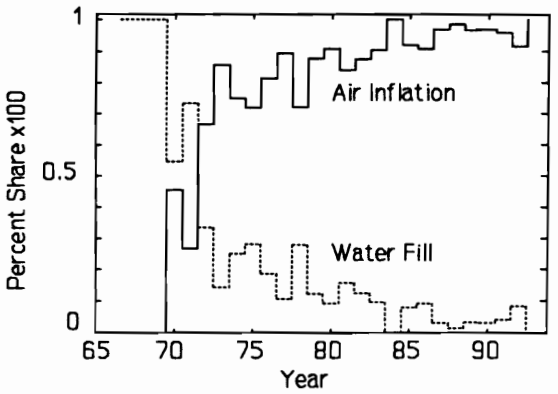

Figure 1.3 Inflation medium comparison through the history of inflatable dams (sources: Bridgestone [10], Sumitomo [11]).

Forty-nine percent of the water-filled dams installed have an L/H ratio of less than ten. The percentage goes to 82% for $L/H<20$, and only 4% for $L/H>50$. There are no water-filled dams longer than 69 meters (226 feet),

and 75% do not exceed 15 meters (49 feet) in length. For air-inflated dams, 53% have L/H<10, 87% have L/H<20, and only 2% have L/H>50. However, the actual installation numbers are leaning heavily to the side of air-inflated dams. Therefore, it may be assumed that the water-fill method is not practiced for long and slender dams. Disadvantages of water-filled dams include:

- Complex and more rugged piping system due to water inertia.
- Corrosion of pipes and equipment. This requires preventive measures, thus increasing the cost.
- Clogging from pipe or water-borne debris.
- Water may freeze in the piping system during cold weather. This may cause a complete system breakdown. It is important to point out that inflatable dams are especially good in icy climates when inflated with air.
- Longer inflation time (as opposed to air where its compressibility allows higher flow rates).
- Larger vibration amplitudes due to the added water mass.

The inflation practice may also reduce the construction materials needed (rubber sheet and concrete). An air-inflated cylindrical membrane requires less internal pressure to reach a circular cross-sectional shape. Water-filled dams tend to have an ellipsoidal cross-sectional shape. This requires more material for a given height, as well as a wider foundation to support the drained dam. A water-pressurized dam typically requires a $4.8H$ diameter length, compared to $3.5H$ for an air-pressurized dam.

A possible advantage of water filled-dams is the reduced vibration level they may experience, by using the water itself as a damping mechanism. An energy dissipation mechanism as shown in Figure 1.4 will have the drawback of requiring a low L/H ratio. Another drawback is that the valve must be adjusted according to excitation conditions, otherwise it will be ineffective or make the system unstable. A computerized control system can be implemented based on the intensity of the internal pressure variations. More complex vibration control systems are possible like active-control, as it will be mentioned in a latter chapter. It should be mentioned that with a small modification (an air-trap U tube), the system can be equally applied for air-inflated dams. However, water-filled dams have lower natural frequencies which are better suited for the water-damper shown. Design drawings and promotion brochures from two different manufacturers show

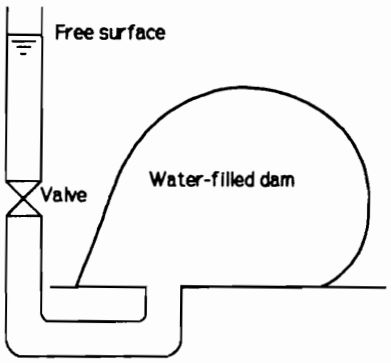

Figure 1.4 Water-fill dam with control valve as a hydraulic damper.

that a similar system is used. However, its purpose (based on the system's dimensions) is to serve as a pressure safety valve rather than a vibration control system.

1.4 Advantages and Disadvantages

Alternative structures are steel sluice gates, wooden flashboards (pinned or framed), steel hinged boards, and flap gates (torque or leaf types). The most attractive advantage of wooden flashboards is the availability of materials and the non-specialized labor requirement. Constructed up to 1.8 meters (6 feet) in height, flashboards cost only a fraction of the cost required for inflatable dams and steel-made gates or flaps (Kahl and Ruell [2], 1989).

Advantages of the rubber dams over their competitor structures include:

- Cheaper than steel-made alternatives. This is more evident when new foundations are not required. In case of a sandy bed, steel gates involve the construction of massive foundations.
- Short erection process with a small non-specialized labor force. For example, a 30m-span dam only requires a two-week period for piping, equipment's house construction, rubber body fixing and dam testing (Bridgestone [3], p. 30).
- Fail-safe for flood susceptible areas. In case of failure (eruption) the dams will deflate, thus allowing water to escape. In contrast, steel gates may fail by getting jammed, thus holding back the water and creating a flood-prone situation.
- Maintenance-free; however, the supporting equipment like water pumps, valve controls, and automation system, require periodic maintenance.
- Ice buildup jam-proof; proven in practice over years of service in icy conditions.
- Fewer intermediate piers do not cause blocking from ice or other floating parts.
- Suitable for corrosive fluids like sewage, sea water, industrial chemicals, etc.
- Reversible flow capable with no extra modifications. Specifically used because of this advantage in the New South Wales (Australia) flood mitigation project (Connor [4], 1969).
- Energy absorption capacity causes minimum damage to its foundation.
- Completely collapsible structure; not a restriction to the free streamflow.
- Can effectively withstand impacts from rocks and boulders, logs and trees.
- Exceeds life expectancy of steel gates which are limited due to corrosion, regardless of the rubberized material's exposure to the sun's ultraviolet light.
- Suitable for extreme and rapid temperature-fluctuating environments.
- Easiness of repairing damages.

Today's materials are considered fatigue resistant from frequent inflation/deflation cycles. Tests reported 400,000 cycles "without appreciable deterioration of body strength" (Bridgestone [3], p.9). Moreover, when air inflated they can raise the sediment deposited above them during their deflated periods. Therefore, they can be used as sediment transport control structures with selective interference (inflated or deflated).

Disadvantages of inflatable dams include:

- Vandalism vulnerability from gun shots, knife cuts, etc. Regardless of the material advances and special protection coatings, this remains a hinder to prospective buyers.
- Statically unstable during deflation (V-notch instability). Sudden V-shape formation at an unpredictable point along the dam. V-notch is possible at a 70-90% deflation. This creates an enormous concentration of discharge at the notch point. Riprap[1] along the dam is therefore required, to avoid downstream erosion and eventually foundation failure. Minimum useful height is restricted, therefore it cannot be considered as a fully operational "flow gate".
- Dynamically unstable at high overflows, under certain conditions.
- Maximum height is restricted to less than 6 meters or 20 feet (5.4 meters or 17.8 feet is Bridgestone's limit, 1992).
- Material transport problems with trucks and cranes (for very long dams).
- Uncertainty for future replacement fabric since the material is specialized for dams.
- Uncontrollable dynamic behavior in case of power failure. One way to control the dynamic behavior of the dams is to vary the internal pressure. Therefore, pressure pumps operated with electric motors or fuel engines could be out of line when they are needed most. As a result the dam owner may request backup systems, resulting in a cost increase.

Although it is advertised that the maximum overflow is designed to be generally 0.4 times the dam's height ($0.4H$), the dam's behavior is still a function of internal pressure which may render the dam unstable under such overflow conditions.

1.5 Historical Review

Inflatable dams were introduced in 1957 in the Los Angeles River, California. The first inflatable dam was used as a flow control structure by diverting low river flows for ground water

[1] Riprap is stream-bed lining with rubble, in order to prevent erosion. It is very common with downstream hydraulic structures like dams, spillways, piers, etc.

recharge, and at the same time being able to allow heavy river flows to escape. Its conception in 1956 is credited to the late Norman M. Imbertson (1975), chief operations engineer of the Los Angeles Department of Water and Power. Made of rubber-coated fabric by Firestone, it was launched with the name "Fabridam" by Norman M. Imbertson and Associates, Inc., and Firestone Coated Fabrics Co. (Firestone [5], 1968). This innovative structure found its way all around the globe. Countries in which inflatable dams are installed include Australia, China, Hong-Kong, Indonesia, Japan, New Zealand, Norway, Pakistan, the Philippines, Spain, South Korea, Taiwan, Thailand, and the U.S.A. These dams are used for height extension on existing dams, river diversion, flood control, sewage flow control, constant water level control, and many other applications (next section).

The early dams, during the fifties and sixties, suffered from ill-fated materials and unpredictable operating conditions. Pounding water would wear the base of the dam and rocks or other material could occasionally puncture the dam. Only a few survived their twenty-year projected life-span. The first company that marketed these dams, N.M. Imbertson & Associates Inc., Burbank, California, had considerable problems and setbacks from failures that occurred and resulting litigation. They parted with their first material supplier, Firestone, over material quality and marketing strategy disagreements. The Imbertson firm "...improved quality by switching suppliers...", said Norman E. Tabor, president of the company (Post and Stussman [6], 1989). The firm is now considering a strong comeback in collaboration with another material supplier (Imbertson [7], 1993).

Other firms include the Bridgestone Engineered Products Co. and Sumitomo Electric Industries, Ltd., originally licensees of the Imbertson firm, both based in Japan. Bridgestone had to suspend operations in 1964 until material improvements were made, and the company became active in the market again in the seventies. Currently, the company has a dominating role in the U.S. market. Bridgestone refers to its inflatable dam as "Rubber Dam", and Sumitomo as "Sumigate". They both design, manufacture, and market their dams, as opposed to the Imbertson firm which designs and then calls on a material supplier with specifications. Sumigate is marketed in the United States by Rodney Hunt Co., Orange, Massachusetts, which has a long history in water control since 1840 (Rodney Hunt [8], 1992). Compared with the installation records of Rubber Dams and Fabridams, Sumigates have a very long list of installations (over 1200), most of them found in Japan and Asia.

1.6 Applications Record

Inflatable dams successfully compete with other flow gate and flow barrier systems. They offer a good alternative, and they are also used in applications of a class of their own. The following is a record of applications thus far. The information was compiled from extensive records from N.M. Imbertson & Associates [9], Bridgestone Engineered Products [10], and Rodney Hunt - Sumitomo Electric [11]. Applications reported by manufacturers include:

- Increase of reservoir capacity, by increasing the height of existing dams.
- Storage pool for irrigation, water purification, water supply, manufacturing processes (iron ore plant, mining reservoir, plant cooling system).
- Flow stream diversion, including underground water replenishment projects.
- Recreation, and beautification (lake formation), maintaining water level in docks.
- Tide barrier (retaining seawater from polluting inland fresh water). This is accomplished with stainless steel anchor fittings and dual anchorage system for bi-directional overflow. During rainy seasons the dam can be deflated to allow floods to escape into the sea.
- Flood control structure. It can be installed at the sides of a flood-causing stream and inflated at will whenever there is heavy rainfall. Moreover, in areas where the advantage of high hill sides are not offered around a dam's basin, the erection of a permanent dam itself can cause flooding. A dam with adjustable height can effectively compensate for an incoming upstream surge, by reducing its height. At any given time when the upstream surge reduces, the height can be adjusted to maximize storage with no flooding (Wickham and McMahon [13], 1969).
- Mud barrier (Nebraska City Power Station, 1978).
- Sewage flow regulator and barrier.
- Navigation aid; acting as a flow valve, it is used to maintain constant water levels in canals, so that ships can pass through (Tsudae Bay, Lake Biwa, Japan, 1988).
- Hydroelectricity; by increasing the water head, thus increasing the output power.

Inflatable dams may also be used as transportable structures to temporarily divert streams for construction purposes, military maneuvers, and flood protection of cities and farmlands susceptible to flooding under high rainfalls.

Low-rise dams can effectively control sediment transport. Sediment, either in the form of suspended load or bed load, is highly dependent on the bed shear stress. This is correlated with the mean velocity of the stream. Therefore, reducing the head difference between the upstream and downstream water levels, the mean velocity is also reduced and similarly the rate of sediment

transport. Moreover, it is advantageous to have a dam with the capacity to be removed (deflated) during floods and the ability to be raised even if there is sediment on it.

Storage dams, in general, have the problem of sedimentation in their basin which may significantly change the reservoir's capacity over the years. In addition, these dams are not built to a maximum possible height because of flooding during rainy seasons. However, an inflatable dam installation on the dam's crest can maximize its capacity without creating any flood danger, nor going through extreme expense to clean the basin.

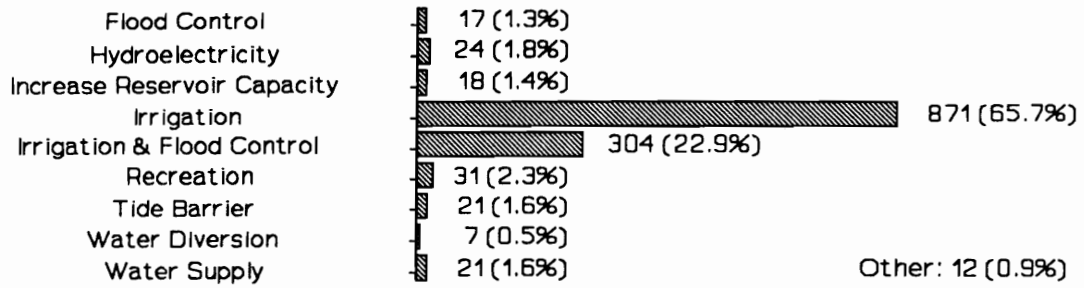

Figure 1.5 Application histogram of inflatable dams (worldwide). In the U.S., the most popular applications are Recreation (22%), Increase Reservoir Capacity (21%), Water Diversion (21%), and Hydroelectricity (15%).

Regardless of the long list of applications, rubber dams are used in their vast majority for irrigation, flood control, and their combination. Figure 1.5 provides a perspective on the level of their major group applications. The data used to compile the graph are based on references [9, 10, 11]. The distribution shown is somewhat misleading to the conclusion that inflatable dams are particularly good in irrigation applications. However, in the U.S. the irrigation, irrigation and flood control, and flood control applications have only a 7.5% share. On the other hand, recreation, water diversion, increase of reservoir capacity, and hydroelectricity have a 79% share! This application difference is explained by the fact that Japan, a relatively small country, has high needs for water for irrigation purposes. The U.S., on the other hand, does not have a massive need for irrigation, or wherever there is such a problem it is not remedied with inflatable dams.

Historically, Japan and Asia in general were more positive (or more desperate) in using these structures. The market in the United States and abroad was pioneered by the Imbertson firm. Regardless of Imbertson's lead in the U.S. and elsewhere, today Japan has the first place in installations (by Sumitomo and Bridgestone). Europe remains a highly conservative market, with only a handful of installations thus far. The worldwide market trend over the years is shown in

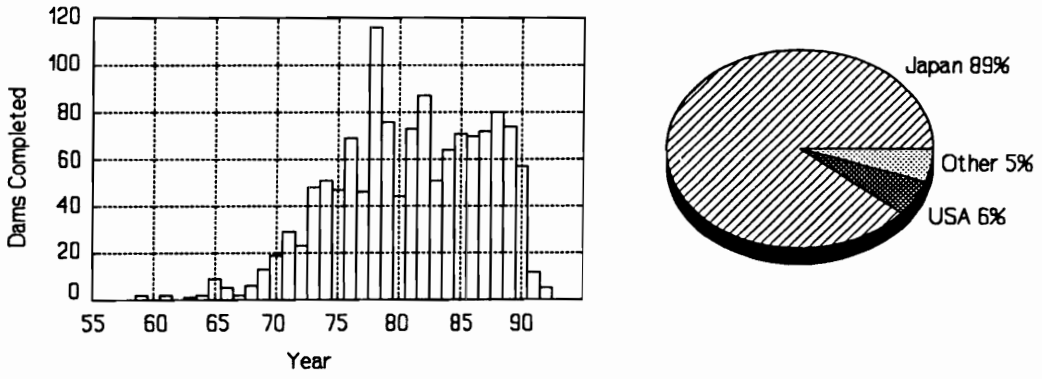

Figure 1.6 Inflatable dams worldwide completed annually (left), total number of dams' percentage per country (right).

Figure 1.6. The data for Figure 1.6 (total of 1326 dams) are made available from the same records that compiled Figure 1.5. Bridgestone claims another 350 dam installations in Japan, but no records were provided (Bridgestone [10], 1990). This number was recently raised to 500 but still no records were made available (Bridgestone [12], 1993). Should these extra 350 or 500 dams be considered, then Japan holds 91% or 92%, respectively, of the dams installed. Moreover, the Sumigate records are also dated back to 1990. Projecting the installations for 1990 through 1992 from Figure 1.6 (60 per year), and adding the 500 extra dams claimed by Bridgestone, the total number of installed dams adds up to just over 2000.

1.7 Literature Review

Almost a decade after the introduction of Fabridams, related literature started appearing in the form of research reports, journals, magazine and newspaper articles, etc. Other work useful to problems encountered in Fabridams was also in progress. For example, in 1965 Paidoussis dealt with low pressure wave propagation in horizontal liquid-filled flexible tubes. A few years later, reports on Fabridams with longitudinal wave surging (like Binnie *et al.* [14] in 1973), showed the connection with that work.

Many references are directly related to the theoretical analysis of inflatable dams. One of the major analysis difficulties (in addition to the turbulent flow) is the fact that the shape of the dam can only be defined when loads are applied. Inflatable dams depart at this point from conventional structures, where it is assumed that the applied loads do not significantly alter the shape of the structure.

Of great interest is the work done employing tests on prototypes and models, as well as the reports of prototype dams' failures. A summary of the main features of significant previous experimental work in inflatable dams, is presented in Table 1.1.

1.7.1 Experimental Work and Reports of Prototype Dams

Baker *et al.* [15] in 1965 worked on model tests for the proposed Mangla Dam project in Pakistan. Their work examined the cross-sectional behavior of model Fabridams under overflow conditions. Models were inflated with water or a water-air combination. Information was derived for the upstream water head, discharge capacity, fabric tensile forces, foundation forces applied from the fabric, cross-sectional shape, cross-sectional vibrations, and nappe ventilation[2]. Measuring techniques and instrumentation involved strain gages on the fabric for tension level and fluctuation (vibrations). Pressure tappings across the dam's crest provided readings for surface pressure. An upward stretch of the dam was observed at very high overflows. Increased vibrations could be partially controlled with nappe aeration and/or introduction of small air quantities in the dam. The downstream effect on dam vibrations was least with water filled models. Natural nappe aeration (or ventilation) was shown to be limited by the stream flowrate.

Paidoussis [16] dealt with the longitudinal wave propagation in flexible liquid-filled tubes. Flexible barges can be used to transport fluid cargo by sea. The subject is also connected with blood flow in arteries. His experiments involved velocity measurements of propagating waves. Excitation was provided using an oscillating water hammer. Pressure differences were determined from cross-sectional displacement measurements, based on capacitance variations. Given suitable excitation, inflatable dams may exhibit traveling waves as well.

Anwar [17] in 1967 designed experiments to check his theoretical work. These involved the cross-sectional behavior of models inflated with air or water and their coefficients of discharge. Models were tested under static and hydrodynamic conditions (overflow). The shape of the dam was determined by measuring displacements with a point gage. Relations were given between the internal pressure, upstream head, overflow head and cross-sectional shape. Skin vibrations were observed in air-inflated models. These vibrations could be partially controlled using a trip rod and nappe aeration. Water-inflated models showed vibrations only at high

---

[2] Nappe ventilation is considered here to be the free air-stream aeration of the downstream base of the dam, from the one abutment-end to the other.

overflows (trip-rod included). Streaklines, which were made visible by injected dye, showed no flow separation and no alteration of the flow pattern (for the case of trip-rod use).

Shepherd [18] in 1969 did model tests on a proposed inflatable dam to be used as an extension of the Koombooloomba dam of the Tully Falls Hydro-Electric Power Project, Queensland. The tests aimed to determine cross-sectional stability, behavior of the spillway, discharge characteristics and likelihood of cavitation. This Fabridam was a dual-anchor type as opposed to those with a single anchor. The concrete crest of the dam was curved upwards, something that aided to the instability observed later on the prototype. The double anchorage was specifically chosen to avoid this instability. Unsteadiness phenomena were not observed on the models, merited to improper membrane material and physical modelling. Dynamic similarity was based on the Froude number with geometric similarity of a scale ratio L_r=50 (L_r is the ratio of prototype length over the model length). The ratio was recommended by Firestone to be suitable for the 6.6 ounces per square yard nylon coated fabric provided by the company (for modelling). Inflation was normally done by water, and air was only included for comparison purposes. Results from nylon material modelling showed "slight vibration or undulation" of 3Hz, with "barely detectable amplitude" whenever the upstream head was equal to the internal pressure head. This was not observed for the stiffer coated nylon fabric. At much higher overflows, vibrations of 5Hz with 1 to 2 inches amplitude and 10Hz with 3 inch amplitude were observed (always in prototype scale). Introduction of air pockets in the water-filled dams created localized undulations or longitudinal waves. The coated nylon was "completely stable" even under higher overflows, with a 3Hz oscillation of immeasurable amplitude. The downstream side of the model showed a slow heaving of 0.5Hz and 12 inch amplitude (for the nylon material). In all cases, nappe aeration eliminated vibrations.

A detailed report on the construction and behavior of the Proston weir and Fabridam (1969) was given by Wickham and McMahon [13]. An application report on Fabridams as flood control structures in New South Wales, Australia, was reported by Connor [4] in 1969.

Binnie, G.M., *et al.* [14] in 1973 reported on the investigation of the failure of two sections of the Mangla Dam, Pakistan (1966). They reported that three-dimensional model tests were also carried out at the Irrigation Research Institute at Nadipur, Pakistan, for the purpose of designing the concrete base. Two-dimensional cases were investigated at the British Hydromechanics Research Association (Baker *et al.* [15]), to study the dam's performance during overflow. Binnie presented graphs showing the relation of "weir pressure above upstream water

level" versus "discharge". The graphs coupled the cases of nappe ventilation with vague regions of dam vibrations. During the prototype's failure, the upstream water level was seen to have a significant effect on the dams. Moreover, the concrete foundation showed signs of pitting. At 40,000 cusecs ($ft.^3/sec.$) overflow the vibrations could be felt at the foundation. Both lateral and longitudinal vibrations became progressively unstable. Eventually, one of the three water inflated dams erupted at 52,000 cusecs.

Beesten [19] in 1974, in his discussion of Binnie's paper, reported that research at the Irrigation Research Institute at Nadipur, Pakistan, showed nappe instabilities. With the introduction of air in the water-filled models, longitudinal surges were observed. Whenever air was the primary inflation medium, V-notch instability was also observed. Immediately before the bag failure at the Mangla Dam, it was reported that the dam exhibited longitudinal "snaking". This was never observed in the model tests. Stodulka [20], in his discussion of Binnie's paper, reported his own analysis and model tests results. He used strain gages capable of measuring 20% strain to determine fluctuations in membrane tension and vibration frequency.

Nemura [21] did some work on inflatable dams' modelling in 1986, that was left unfinished. Her suggestions, though, about the measuring and instrumentation techniques are worth noting. Cross-sectional deformations could have been collected photographically through reference grids and then digitized. Then, the transformation from camera coordinates to model coordinates could have been processed numerically.

Alwan [22, 23] in 1986 did model tests and finite element analysis to obtain relationships between headwater, tailwater, overflow and internal pressure. Water, air, and their combination were used for inflation. Displacement measurements of the dam were logged using point depth gages. Nine strain gages were used for membrane stresses. The ends of the model were modified to minimize any stiffening effect on the model's response. The results described the average behavior of the dam under overflow conditions and variable tailwater head. Measurements with respect to the dynamic behavior of the dam were not reported. In 1988, he enhanced his findings by working with three length to base-width ratios. Discharge coefficients were derived, including a relationship between the upstream water head (h_u), overflow height (h_o) and dam height (H),

$$0.70h_u = h_o + H \tag{1.1}$$

Bridgestone reported in July of 1991 that the discharge coefficient (C) of their dams is governed by the overflow water height h_o and the dam's height H,

Table 1.1 Summary of previous experimental work.

Test Model:	L(in.)	L/H	t(in)	Material	Use
Paidoussis (1965)	70.9	73.4	0.0007	Latex rubber	Longitudinal wave propagation velocities. Modelling of extensible tubes.
			0.0015	Polyethylene	
Baker *et al.* (1965)	18.0	2.21	n/a	Rubberized cloth (supplied by Firestone)	2D static and overflow conditions. Modelling of proposed Fabridams in Pakistan.
	60.0		n/a		
Anwar (1967)	24.0	2	0.01	Polyethylene. T=1.1-2.4 ksi (Tensile strength).	2D Static and overflow conditions. Verification of analytical work.
		2.67			
Shepherd (1969)	47*	39*	2.5 oz/yd²	Nylon	2D static and overflow conditions, plus some longitudinal reports Modelling of proposed dam.
			6.6 oz/yd²	Nylon fabric (neoprene coated)	
Binnie (1973) Stodulka (1974)	Reported tests done in Pakistan and Britain, (L_r=30). Reported his own tests, in Binnie's discussion.				
Alwan (1986)	15.6	n/a	n/a	n/a	2D overflow conditions.
Alwan (1988)	15.6	3.5**	n/a	n/a	2D overflow conditions. Derivation of discharge coefficient.
		2.2**			
		1.6**			

L: length, H: height, t: thickness, n/a: not available, *: calculated, **: L/Base width

$$C = 1.77\frac{h_o}{H} + 1.05$$
$$Q = CLh_o^{1.5} \tag{1.2}$$

where Q is the discharge volume (m^3/s), and L is the dam's length (m) [3]. To get discharge volume in cubic feet per second, the discharge coefficient C is multiplied by 1.81.

Besides the work on inflatable bags used as dams, McCarty [24] reported in 1990 that ongoing research at the University of Michigan, funded by NASA, is investigating the use of inflatable arms. These pressurized cylindrical membranes are proposed to substitute for the Shuttle's manipulator system as a light and compact alternative. The material used is 11 mil thick (0.011 inches) neoprene-coated Kevlar. An inflatable cantilever beam (1 meter long, 6 inch

diameter), transversely loaded at the end, showed an almost linear response, with 4.89lb/in (end displacement) at 10psi, and 8.87lb/in at 30 psi internal pressure.

1.7.2 Other Work

Anwar [17, 25] was the first to report detailed analytical work in 1967. His work dealt with two-dimensional static and hydrodynamic conditions of air or water-filled double anchored dams. He assumed a fully aerated nappe, inextensible and weightless membrane, no membrane stiffness, and internal pressure proportional to the height of the dam height, H, plus the overflow water head, h_o. The proposed closed-form solution (in terms of elliptic integrals) did not require the upstream and downstream anchors to be at the same level, thus creating a step. The downstream side of the dam was assumed to be tangential to the base, thus there was no restriction with regard of the length of the membrane. Later on, in 1985, Watson [?, 26] pointed out some errors in Anwar's solution.

Harrison [27] used a finite element iterative procedure in his analysis in 1969-70, including the material weight and the material extensibility. The iteration process was reported to be rapid at internal pressures in excess of critical values. His analysis showed an unorthodox reduction of tensile stresses throughout the membrane with upstream head increase. He considered inflation with air, water, and air/water combination, under various upstream heads including overflow conditions.

A paper published in Japanese by Ogiwara *et al.* [28] presented theoretical and experimental results. The weight of the membrane was taken into account. Air and water inflation were considered under various overflow heads.

Binnie, A.M. [29] in 1973 presented a study of water-filled dams with impounding water. One basic difference from Anwar's analysis is that the upstream side of the dam is circular. For an air-inflated dam, the downstream side is circular instead. The results of Binnie do not show the step that appears in Anwar's analysis. The solutions for the shape of the downstream side of the dam require the use of elliptic integrals as well.

Parbery [30, 31] in 1976 compared a finite element method with Harrison's method. Water-fill and air/water combination were considered. In 1978 he considered air-inflated dams that showed the effects of the membrane weight and extensibility to be minor. It was also concluded that there are dual equilibrium solutions in some cases, which can be avoided with shorter perimeter lengths.

A numerical integration method (Runge-Kutta-Merison) was used by Hitch and Narayanan [32] in 1983. Only the water-fill and impounding water case was considered. The results are in agreement with those of Binnie and Watson. Watson [26] in 1985 also presented a study on the static shape of the dam. It was the first time that somebody identified the error in Anwar's equation (13) (1967) that relates the dam's tension to the height and the differential pressure on the upstream face.

Plaut and Fagan [33] in 1988 treated free vibrations of air-inflated, inextensible, double-anchored circular membranes. It was shown that the effect of membrane weight was a slight reduction of the natural frequencies. Plaut and Leeuwrik [34] considered free non-linear 2D oscillations of air-inflated double-anchored cylindrical membranes (1988). The material was assumed to be inextensible and its weight was neglected. The formulation was based on Galerkin's approximation method with one and two terms. Hsieh *et al.* [35] in 1989 considered vibrations of liquid-filled cylindrical membranes. Some experiments were also reported. Hsieh and Plaut [36] reported free vibrations with impounding water (1990), based on the finite difference method. Plaut [37] considered parametric excitations with oscillatory internal pressure.

Indirectly related to inflatable dams is the work presented in references [38]-[47]. Of particular interest are the reports by Szyszkowski and Glockner [38] in 1985, and Watson [26] 1985, who dealt with parachute dams. Very useful is the book by Firt [39] which covers a wide spectrum of inflatable structures.

Chapter Two

MODELLING

Correct interpretation of experimental results relies heavily on the modelling practice. In this work, the modelling practice includes both physical and analytical considerations. The first deals with construction details, and the second with similitude and dimensional analysis. The test facilities used are also described, as well as the necessary modifications and developments during this investigation.

2.1 Introduction

It is always perceived (at least initially), that a model is smaller than its prototype. However, it is well-known that it is possible and sometimes prudent to have a prototype-size test model, or even a larger than a prototype-size model. Just for the sake of argument, let us consider the case of an existing prototype-size model dam. Instrumentation options are increased, similitude analysis is simplified, and laboratory running costs do not exist. On the other hand, the prototype inflatable dam has to be located downstream of a flow control structure (possibly another dam). Moreover, test to failure is enormously expensive, flow visualization becomes difficult, and the bed-stream is representative of a particular location. It is very clear that using a prototype dam is not a viable option, even if such a dam was made available for tests. Therefore, in this problem the model has to be a fraction of the prototype's size.

The inflatable dam model is studied with and without flow interaction (forced and free vibrations). Free vibration tests can define the model's structural characteristics. Combining forced

and free vibration tests is sometimes sufficient to determine unknown applied forces. One of the requirements for combining the results of these two types of tests, is that their modelling details have adequate similarity. Even better (if possible), the mathematical model should be derived from the same test model used for both free and forced vibrations.

2.2 Physical Considerations and Assumptions

Investigating the *dynamic response* of a structure, requires that the prototype is modelled in a way that its time domain characteristics of interest are transferred to the model. If it is not possible to transfer all or most of these characteristics, then here lies the challenge of choosing those characteristics that dominate over the others. Specifically in this problem, previous reports mentioned two and three dimensional vibrations on prototypes occurring before catastrophic failures (Chapter One). It is therefore important that the model behaves likewise. Previous work with model tests did not emphasize enough (or any at all) in their reports on a three-dimensional (longitudinal) response, presumably due to modelling practices.

Intuitively, it is expected that an inflatable dam has a predominantly two-dimensional (cross-sectional) behavior at a small length over height ratio, L/H. A three-dimensional response may be observed at a sufficiently high L/H ratio, but it may not necessarily dominate over a two-dimensional behavior. Given the laboratory facilities available, 61cm (2 foot) and 183cm (6 foot) wide channels, the L/H ratio is consequently limited. For practical purposes (given later), the minimum model dam height H is set approximately to 6.3cm (2.5 inches). This results in a maximum L/H ratio of 9 and 29 at full inflation, for the 61cm (2 foot) and 183cm (6 foot) wide channels, respectively. Partially inflated dams do not reach the maximum height, because they do not assume a cylindrical shape, and therefore they have higher L/H ratios.

It is customary in flow-induced vibrations involving two critical structural sizes (like the length of cylinder over its diameter), to refer to similar ratios (L/H) as *aspect ratio* (Blevins [48], 1990). The terminology will be employed here as well, but no special symbol will be assigned and the aspect ratio will be identified as L/H.

Equally important is a determination of how the models' aspect ratios compare to the real world. It is assumed that the aspect ratios in models and prototypes, being dimensionless numbers, are congruous and comparable with each other. Figure 2.1 shows the distribution of the aspect ratio for prototype structures already installed, compared with the test models' maximum ratios at full inflation. The source of the data is the same as in Chapter One. It should be noted that 51%

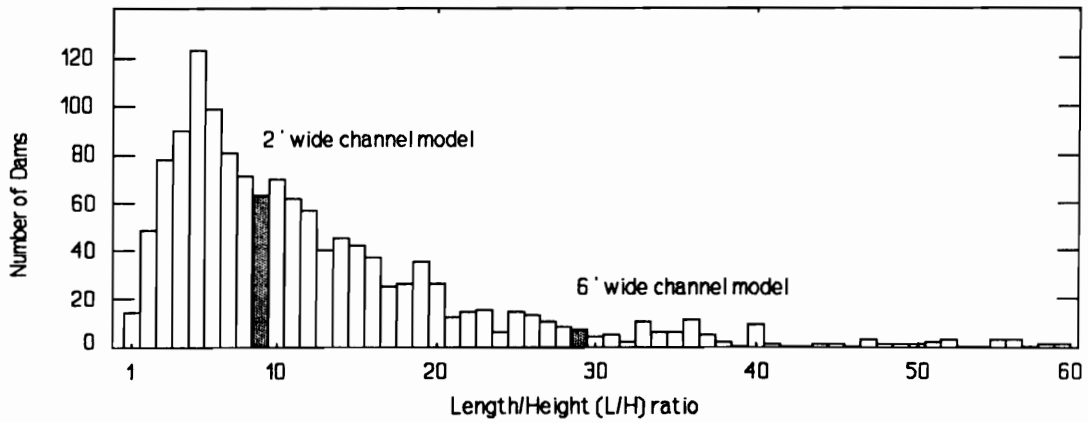

Figure 2.1 Distribution of aspect ratio (L/H) for prototype dams from 1326 records, in comparison with the models' ratios 9 and 29. $(L/H)_{max}$=229 and $(L/H)_{min}$=0.5.

of the prototypes have an aspect ratio (L/H) greater than nine. Therefore, a model with L/H=9, as used here, is very close to the mid-percentage value of the prototypes, thus representative of the prototype dams. Only 7.5% have an aspect ratio greater than 29. The two models' aspect ratios are shown in Figure 2.1 as highlighted bars.

The graph (Figure 2.1) does not distinguish between air and water inflated dams, nor material fabrication and thickness. This generalization appears to be inappropriate, since water fill is expected to lower the critical L/H ratio, where a longitudinal response is notable. This is due to the increase of mass, thus reducing the fundamental frequency, resulting in bigger oscillation amplitudes. However, a distribution analysis of air inflated and water filled dams produces similar distributions to the one in Figure 2.1.

Material thickness affects the three-dimensional behavior if it exhibits sufficient bending stiffness. In order to increase the likelihood of a notable three-dimensional response, the membrane material is chosen to be as thin as possible. This reduces or completely eliminates membrane bending stiffness. It has been assumed here that the prototype material can be modeled as a membrane. This is true for the majority of the dams already installed (Sumitomo and Firestone). In some cases, though, prototypes were built with a membrane material that definitely exhibits significant bending strength (Bridgestone).

Materials obtained from the current manufacturers of inflatable dams, personal contacts, as well as literature information, suggest that the material thickness and stiffness vary beyond any

simplistic modelling considerations. For example, one manufacturer used a thick rubberized multilayer material of 1.9cm (0.75 inches) thickness (more like a tire construction) for a 60cm (2 foot) high dam. Another manufacturer used a 0.63cm (0.25 inch) thick, more flexible, multilayer rubber for a higher dam.

This huge material difference does not only account for the different design philosophies (shell versus membrane), but also for the different dam applications, their safety factor, and perhaps most important, liability concerns. The first manufacturer was installing the dam for recreational purposes, where in case of a failure lives could be threatened (U.S.). The second manufacturer installed the dam for irrigation purposes, and presumably no lives would be in an immediate danger (Japan). These two cases present the essence of the material modelling dilemma, that is, whether these are inflatable shells with some bending stiffness or inflatable membranes with only tensile strength. Material thickness and reinforcement design is primarily based on the dam's height. It is assumed here that the prototype material does not have any appreciable bending stiffness, and therefore the materials chosen for modelling are sufficiently comparable.

Dam models are constructed only with vertical abutments, to maximize their *effective aspect ratio*. The effective aspect ratio is basically related to the abutment inclination and a *critical aspect ratio* such that a three-dimensional behavior becomes notable. In the real world, the sides of an inflatable dam take the inclination of the stream's abutment inclination. The vertical sides restriction here is imposed due to the model's length limitation and construction simplification. It is assumed that dams with inclined side-banks have a smaller effective length (or effective aspect ratio, L/H) than dams with vertical sides.

2.3 Model Construction

A standard method of construction is developed to expedite the model construction process. The priorities for this method are outlined below. These *requirements* affect not only the efficiency of the erection process, but also modelling details.

a) Repeatability; the design is made simple enough to warrant sufficiently accurate replications, so that comparison between measurements of different models is possible. This results in the use of a permanent sealant (like silicon), instead of a rubber gasket that would allow alignment errors during assembly.
b) Rapid assembly and erection; the model is available for erection within 48 hours, and the

erection time is kept to a minimum of 1 hour. This limits the selection of sealants to those that are curable within 24 hours. Moreover, the clamping method is a mechanical device, instead of a glue-bond that has the advantage of minimum flow interference, but the disadvantage of a longer installation period.

c) Backup availability; a follow-up model is made available in cases of tests to failure, accidental tearing during erection, or any other unintentional failure.

From the requirements above, the most demanding is the backup availability. Due to the instrumentation practice, it is not always possible to have two instrumented models at the same time. Instead, the backup model is used for general information input and for internal pressure variations.

Modelling details are devised and modified, with instrumentation and material characteristics having priority over efficient and correct construction practice. Such a case is the construction detail of the side clamp, through which the instrumentation wires pass. The presence of the cable increases the step (Figure 2.3) made by the clamping strip by 100 to 200%, and consequently increases the flow interference. Alternative solutions were not successful. Moreover, the interference is minimum, as explained in the next section.

2.3.1 Two Foot Long Model, $(L/H)_{max}=9$

This model is constructed in a 61cm (2 feet) wide water tunnel. The glass-made test section is 61cm (2 feet) wide and 76.2cm (2.5 feet) high. The top of the test section is removed so that it can be used as a water channel. Flow converging constructions made by other lab workers forced the model to be elevated at approximately mid-height. The flow is forced to pass only over the dam by using a water-tight barrier below the dam. An aluminum frame supporting-structure is constructed, that also provides the platform where the dam is fixed. Figure 2.2 shows details of the construction of the supporting structure. The panels of the supporting structure, made with Plexiglass(R) sheets, are also used as shear panels for additional strength. Aluminum structural sections are used for their clean oxidizing property. Clear Plexiglass sheets are used for the needed flow visualization.

Originally the support structure offered only a 66cm (26 inch) long platform, which was proven to be inadequate. Flow visualization showed that there was a flow disturbance made from the leading edge of the platform that was propagating up to the dam. Moreover, the short downstream length of the platform (15cm long) was thought to be significantly altering the

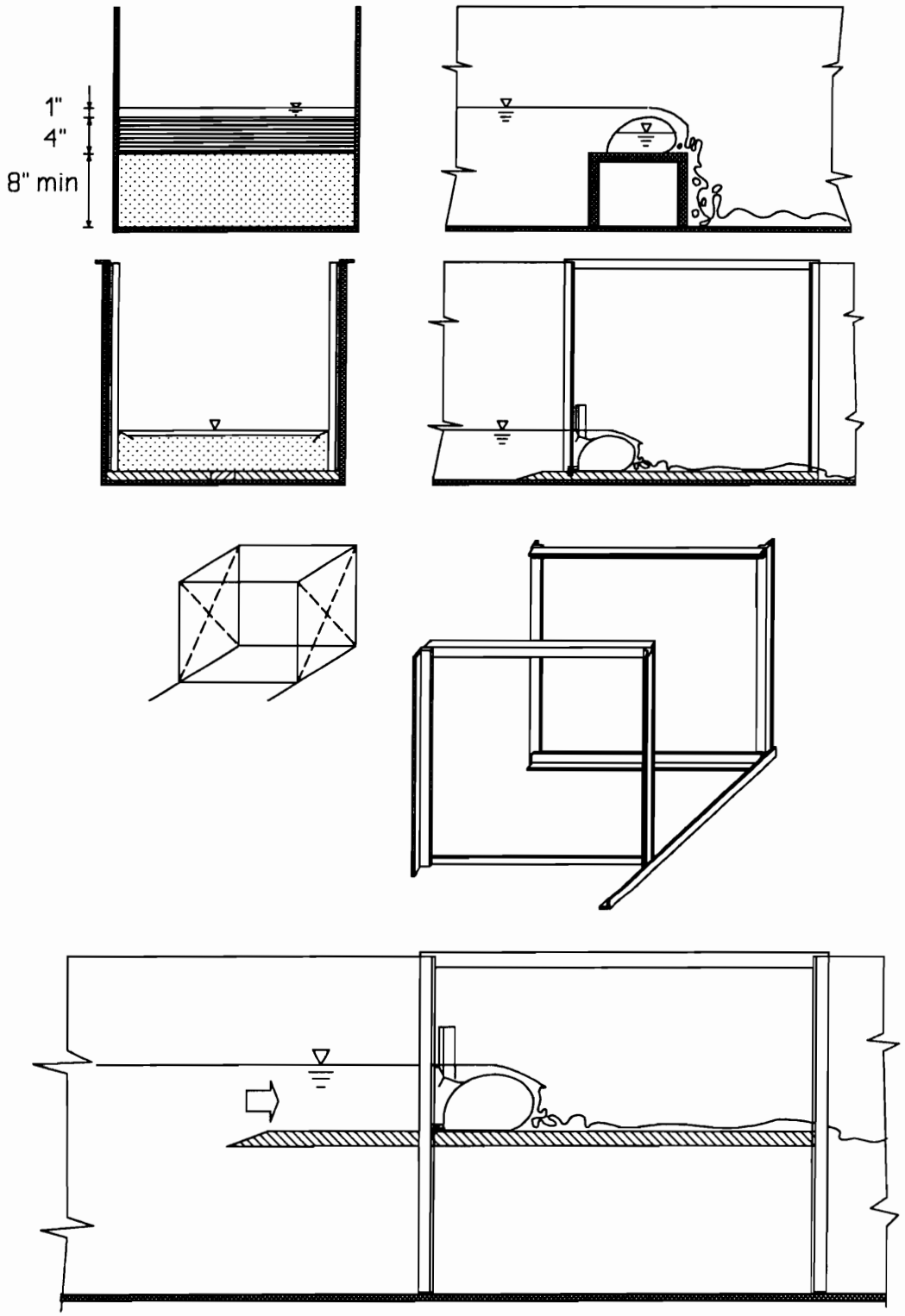

Figure 2.2 2 feet wide channel model and supporting structure development history.

model's vibrations. This is particularly important, since the vibrations on a dam are primarily induced from the action of water falling on its downstream base. A longer platform (122cm long) was later fabricated that substantially improved the situation. The platform could not be made longer than 122cm (48 inches), because it would interfere with the ends of the testing section.

Several anchoring methods were attempted. Their main objective, besides retaining the model, was minimum flow interference. The final method that is used throughout the experiments

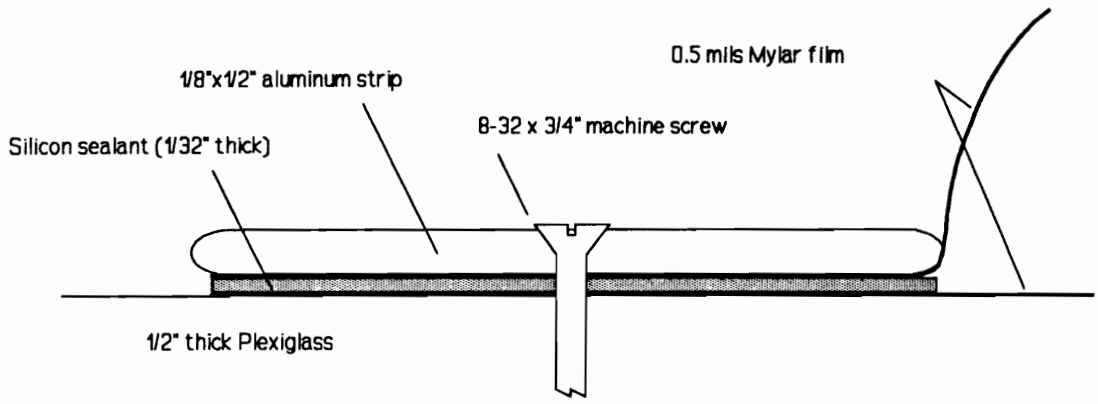

Figure 2.3 Anchorage detail for the 61cm (2 feet) wide water channel setup. Friction (by pressure action) and adhesion are the only effective retaining forces.

in this water tunnel (converted to channel), employs aluminum strips and silicon sealant as shown in Figure 2.3. The clamping concept behaves adequately as long as the silicon sealant is allowed to fully cure. The curing period, however, is approximately 24 to 48 hours. Attempts to find other types of sealants, or otherwise shorten the curing period, were not successful.

The membrane size measures 20cm (8 inches) by 53cm (21 inches) at the seam lines, with 74° side cuts. Therefore, the actual aspect ratio is 8.4 (L/H=53/6.3). Normally the side cuts are 45° as in the prototypes. This 45° inclination is required in the prototypes to be able to fully flatten when deflated. Having no such requirement in the models, however, a 74° inclination gives the best fit, in order to ensure minimum folds at the model's ends. This provides less flow disturbance at the model's ends.

In a fully inflated condition with no impounding water, the model assumes a completely cylindrical shape. Its height measures very close to the diameter of a circle with perimeter $2\pi R$;

$$\text{let} \quad 2\pi R = 8 \text{ in.} \qquad \therefore \qquad H_f \approx 2R = \frac{8}{\pi} \approx 2.5 \text{ in.} \tag{2.1}$$

where H_f is the dam's height, free of loading. Only the maximum length over height ratio is used,

L/H=9. This results in a dam height of H_f=2.5 in. (6.3cm), under no external loads (no impounding or overflowing water). With overflow or statically impounded water, the height of the dam may be increased slightly ("heaving"). During overflow the height may also tend to be reduced, depending on the internal pressure.

Particular problems encountered in this setup are some occasional minute membrane ripples, presumably due to the membrane misalignment at the anchorage arrangement; wakes due to the front edge of the short platform; tunnel vibration at very high velocities due to the partially filled water tunnel pipes; surface waves at very low velocities due to the pump action; inability of the system to perform impounding water tests; and a model installation success ratio of only 20 to 30%. The latter is in fact a result of limited time share of the laboratory facilities and the resultant need to compress the work done within the required time limits. As mentioned before, the silicon sealant seams require a 24 to 48 hour curing period.

Flow interference of the clamping device at the abutments of the channel is minimum. This is due to the ends of the dam which are naturally raised above the rest of the dam's body. Photographs (35mm) in Figure 2.4 show the details of the construction at the corner, and the wakes generated by the dam's raised end. The effect is more clear under smaller overflow conditions, where the ends of the dam are actually shown above the water level. In the case of a 45° membrane side cut as in the next model, the ends are raised above the dam to a height approximately equal to the height of the dam. This makes it impossible to be overtopped in any realistic situation. It will require an upstream water head of h_u=2.86H to create an overflow height h_o=H, based on equation (1.1).

2.3.2 Six Foot Long Model, $(L/H)_{max}$=29

The testing facility is developed using a 30.5x1.8 meters (100x6 feet) concrete towing tank, and a 10cm (4 inch) diameter PVC pipe water recirculating system. Advantages of the new water channel over the water tunnel are the width increase, a 12m (40 foot) long "test section", absence of pump-induced vibrations, absence of an elevated platform, and better availability of the facilities. Disadvantages include the need to actually construct the recirculating system, the limited access available for flow visualization (only side windows), and the limited capacity of flow rate due to the available water pumps.

Particularly troublesome is the development of the water recirculation system, since the channel's bed is below ground level (where the two water pumps are located). The following

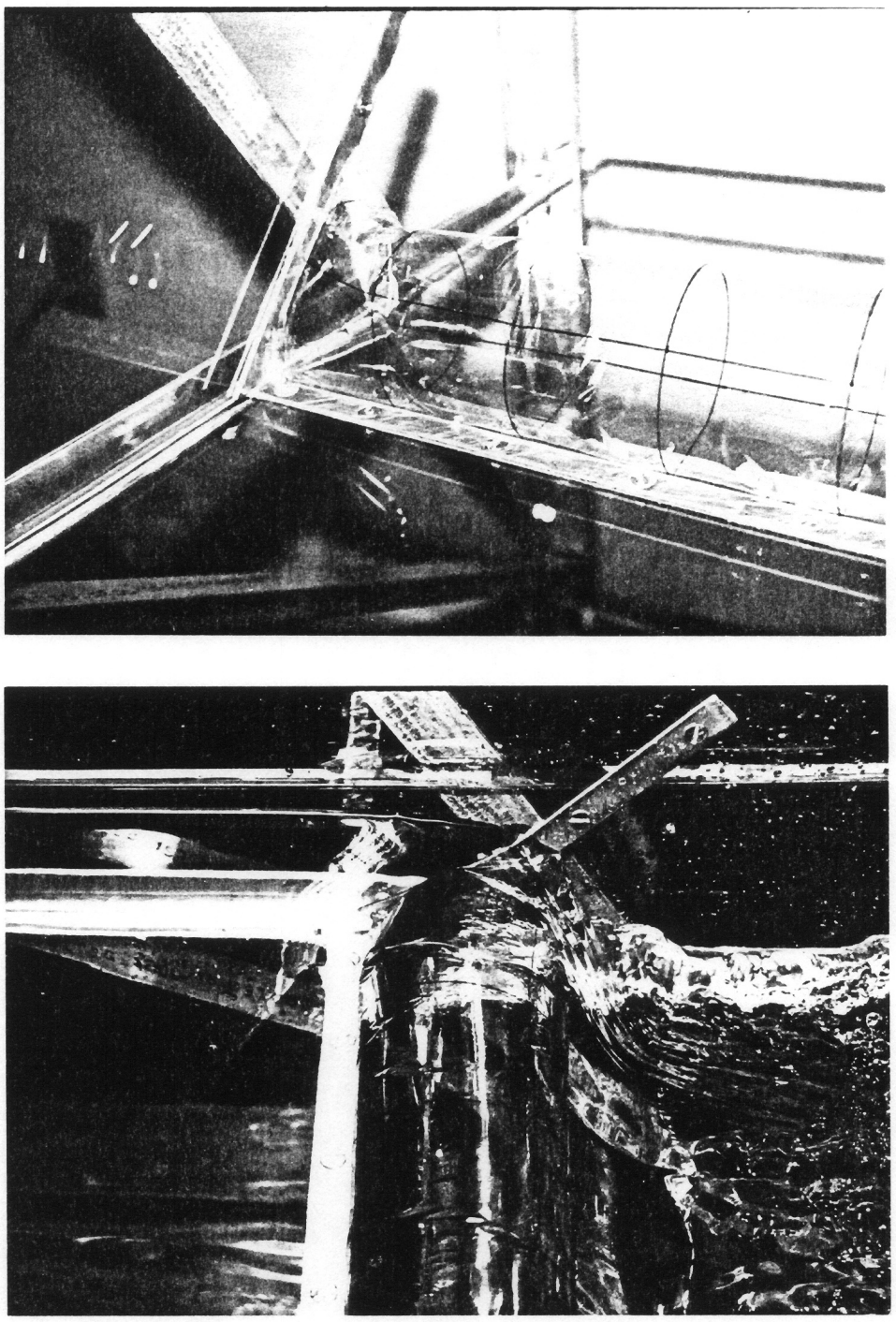

Figure 2.4 Photos of the 21.5x2.5 inches model. *Above:* View of the anchorage arrangement between the horizontal and vertical clamping strips. *Below:* Overflow conditions at the same location.

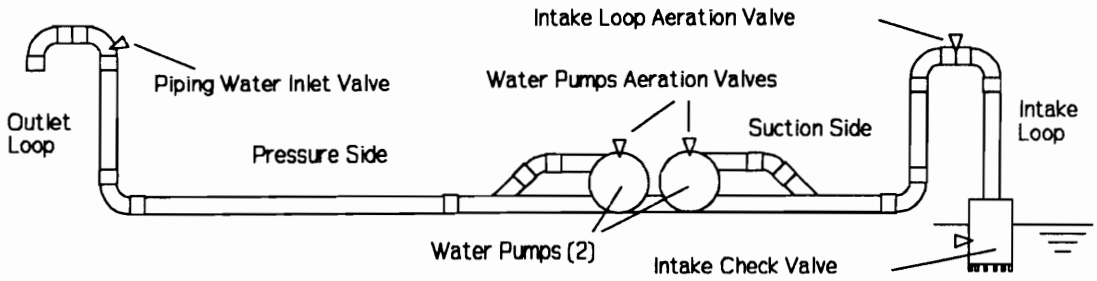

Figure 2.5 Pipe system configuration of the circulation system in the 6 foot wide channel. The total length of the system is 27.5 meters (90 feet) long. Its 3hp pumps can deliver 26.2 l/s (55.6 ft^3/min).

drawing (Figure 2.5) shows the system developed. In order for the system to operate, the pipes have to be filled with water and at the same time air-bled. It is therefore necessary to design, construct and install a check valve at the intake of the pipe system, positioned below the channel's water level. An air escape-valve is also needed at the top of the intake loop, for the water to reach the check-valve.

The pipe-fill intake valve is located at the outflow loop. This loop has to be elevated so that the water will first overflow into the intake-loop and therefore fill that section of the pipe. Furthermore, the bleeding valve of the pump itself has to be used before the water is allowed to reach the suction pipes.

For economy reasons the pressure side of the piping system is constructed with thin-wall Sewer and Drain PVC pipes. In order to minimize the initial inertia shock delivered to the pipe system when the pump is switched on, the entire pipe system is filled with water. The suction side of the system was originally made with thin-wall Sewer and Drain pipes, too. Their suction capacity, though, was proven inadequate under the full pump capacity and they flattened.

Surface waves and variable velocity profile along the width of the channel are the first problems encountered. These effects are generated from the relatively rough side walls and from the absence of a flow-diverging structure. Figure 2.6 shows the arrangement that partially remedied the problem. The "sluice gates" at the beginning of the channel serve the purpose of reducing or eliminating surface waves. Honeycomb filters are used for streamlining. Concrete cylinders are used to roughly diverge the flow. Most of the air bubbles introduced at this point escape during the 15.2 meters (50 feet) trip before the model. Smaller bubbles that remain are useful for flow visualization using light sheets.

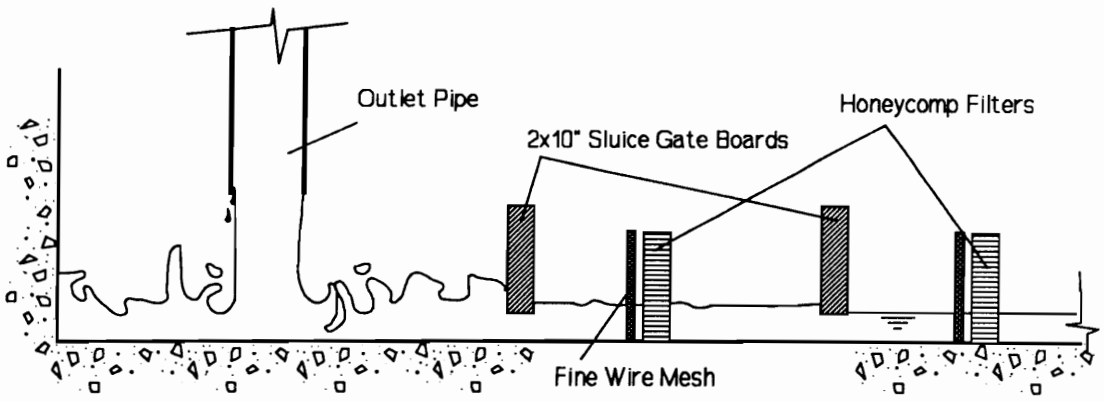

Figure 2.6 Filter and Sluice Gate arrangement of the 1.83 meters (6 foot) wide water channel. Four more honeycomb and wire-mesh filters are installed further downstream, ending 4.6 meters (15 feet) before the model dam.

The anchorage system here (Figure 2.7) resembles the system used by some manufacturers on prototype dams. Instead of a friction/shear device used earlier, it offers a mechanical lock. Although a superior anchoring device, the arrangement creates a step of 5/16×7/8 inch, as opposed to a 1/8×1/2 inch step in the previous experimental setup.

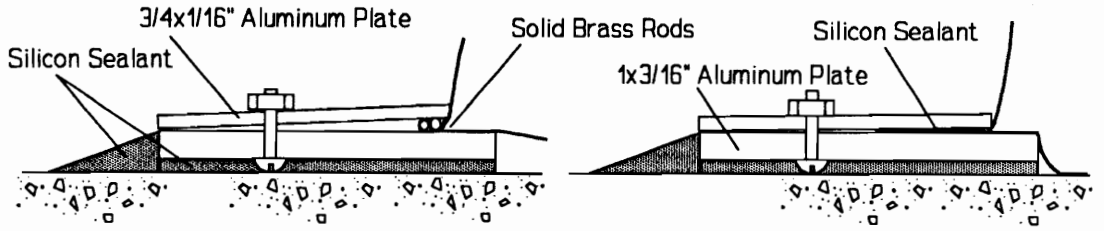

Figure 2.7 Anchoring arrangements for the 6 foot long model. Both have the same basic clamping units. The silicon made ramp is used to minimize wake effects.

Flow visualization did not show any particular change in the flow pattern. Moreover, since the highest vibration amplitudes are generated from the downstream action of the water (at the base of the dam), it is assumed that there is no significant alteration in the dam's excitation. Besides, this particular anchorage system offers a better air-tight seam, since it does not rely on pressure that is limited to the vicinity of the anchoring bolts. The installation process is also much simpler and consequently faster. Based on the same clamping arrangement, a second method is also used (right sketch of Figure 2.7) which facilitates an even faster and more accurate process. This is a combination of the clamping method in the previous section and the anchoring base of this setup.

Side banks are kept vertical in this model as well, to take advantage of a longer effective length, as in the previous setup. Instead of 74° inclination cuts on the material, though, 45° cuts are used as in the prototypes. This change in the cuts' angle is necessary to achieve complete channel draining when needed. However, such an arrangement increases the flow disturbance at the ends, by increasing the membrane material folds.

2.3.3 Membrane Material Characteristics

It is mentioned earlier that the material characteristics of the dam's membrane play a significant role in its behavior. Failure to deal with the problem of material selection may inhibit a significant part of the model's structural response. Previous workers used polyethylene, nylon, rubber, and their fiber-reinforced derivatives. These materials are under the general category of *organic synthetic polymers* (inorganic polymers include silicon-rubber). A brief description of synthetic polymers is given in the next paragraph.

Synthetic polymers are further classified [49] as *elastomers*, *plastics*, and *fibers* depending on their elastic (mechanical) properties. The upper limit of extensibility of an elastomer is 100-1000%, for plastic 20-100%, and for fiber less than 10%. Based on their response to heat, they can be even further classified as *thermoplastic* and *thermosetting* polymers. Rubber is an elastomer polymer, polyethylene is a thermoplastic-plastic polymer, and Nylon is a fibrous polymer. In search of a relatively inextensible material, though, none of the above is appropriate. Instead, polyester, a fibrous polymer, has the inextensibility (tensile strength) required to be used in very small film thicknesses. From the different brands of polyesters available, Mylar(R) manufactured by DuPont is the one chosen.

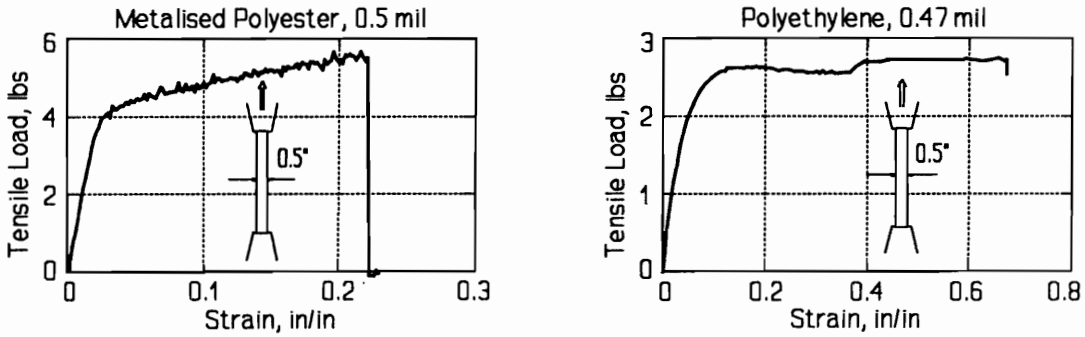

Figure 2.8 Tensile tests on the two materials chosen for model construction. The rough line in the metalized polyester plot is generated by signal noise.

Samples of polyethylene, metalized polyester, and other types of film material are tested for their tensile strength and plastic properties. Specimen sizes are 0.5" wide and 3" to 4" long (initial test length). Characteristics of interest are the modulus of elasticity, viscoelastic properties, and fatigue. Tensile test results are shown in Figure 2.8 for polyethylene and metalized polyester. The modulus of elasticity is calculated to be 690 ksi and 21.3 ksi for the metalized polyester and polyethylene, respectively. Similarly, their yield strength is found to be 14 ksi and 0.64 ksi, respectively. These, and other types of polymer materials, initially show a linear response. Viscoelasticity, though, quickly becomes apparent during load cycles.

Mylar (polyester) is the material of choice because of its high tensile strength at very small thickness. However, because of its "brittle" characteristic it can only withstand a limited number of folding-stretching cycles. As mentioned before, folds always exist at the sides of inflatable dams (prototypes and models). These folds have the tendency to go through stretching cycles during overflow vibrations. Mylar showed that it can resist only a few hundred cycles before microscopic holes start appearing. Consequently, polyethylene is also used, primarily for its resistance to stress fatigue.

Some of the material characteristics of clear Mylar are presented below, as listed by the manufacturer (DuPont [51-53]). The characteristics presented are those that are judged to be useful as inputs for a numerical analysis.

- Thickness (48 Gauge) ..... 0.00048 inch (12 μm)
- Modulus (Elasticity) ..... 550 ksi (3790 MPa)
- Ultimate Tensile Strength ..... 27 ksi (186 MPa)
- Unit Weight ..... 10.4 lb/ream (16.9 g/m^2)
- Elongation at break ..... 110 %

As mentioned earlier, modelling of the various material types and thicknesses is not applicable in this case, therefore no scaling ratios will be attempted. Similar characteristics for polyethylene were not made available, thus the modulus of elasticity is considered to be the one found in the tensile tests shown before.

Information on the tensile strength of the prototype material was not made available, but it is certain that this varies based on the number of nylon reinforcement layers. For modelling purposes, however, it is assumed that under nominal stress levels it is virtually inextensible and its bending stiffness will not appreciably change the response of the dam. Unfortunately, it is not possible to guess any possible tensile strength scale ratio since the factor of safety for designing

the dams is also not known. Down-scaling the material characteristics based on the thickness of the material is also not acceptable since it can lead to other problems.

2.3.4 Instrumentation Setup

Instrumentation setup and practice procedure are fully guided by the particular requirements of the problem to be studied. A full description of the instrumentation approach is given in the synonymous chapter (Chapter Three). Only the arrangement details are presented here, to promptly respond to previous comments about "minimum model height". It is explained how requirements on flow and structural disturbance limit the selection, as well as the positioning, of instruments.

In this vibration problem there is a large-amplitude response and a free-surface flow over the dam. The large amplitudes prohibit use of laser beams for flow velocity measurements at the vicinity of the model's surface. Use of lasers for structural response (displacement, velocity, acceleration) is also not practical. The surface of the dam has translational and rotational response. Therefore, a measuring method that would require the collection of the reflected laser beam would not be successful. Moreover, the presence of the water's free surface restricts the laser beam from approaching from the top, due to the presence of waves and ripples. An oncoming beam from the sides would require reflecting mirrors upstream or downstream the dam. Also, use of any instrumentation probe from the outside of the dam is not permissible due to similar flow disturbances.

It is therefore clear that in order to avoid any flow disturbance, the instrumentation has to be located inside the model. On the other hand, in achieving a maximum length over height ratio, it is required that the model height be as small as possible. Moreover, the requirement that the instrumentation should not touch the model remains. Considering the material used (very thin with no bending stiffness), the most sensitive probe could still be interfering enough to have the effect of a local membrane support.

One of the two non-intrusive instrumentation techniques developed for this work is small enough to fit into a model of 5.1cm (2 inch) diameter. Due to miniaturization problems in constructing the actual model, a minimum of 6.3cm (2.5 inch) diameter is used instead. The method requires that a magnetic field source is placed on the point from which a response is sought. A permanent disk magnet of 3/16 inch diameter by 1/16 inch thickness, and 0.2 grams (7.4 g/cm^3), is used.

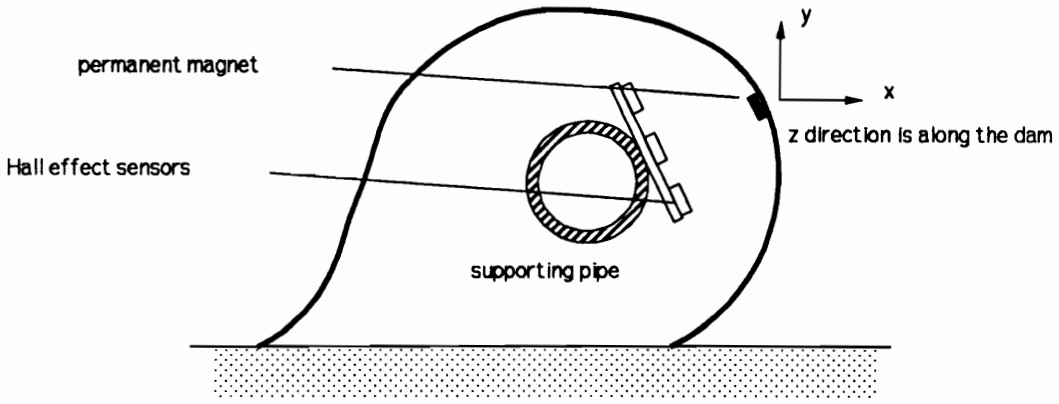

Figure 2.9 Cross sectional view of the model dam, with the magnetic field instrumentation and the permanent magnet installed.

It can be argued that the magnet weight changes the local structural characteristics of the model. There is a local weight increase factor of 665 for the area where the magnet is attached, or up to a factor of 42 for the strip of material on which it is used. Regardless of this enormous mass increase, the structural characteristics of the model do not change appreciably. This is so because this structure's response is stiffness dominated. Stiffness for an inflatable dam results largely from the internal pressure and up to a point from the membrane tensile strength. Therefore, its dominant response cannot be deduced by just observing the membrane tensile strength over its unit weight ratio, as can be done with steel structures. Instead, a full analysis is needed or better, free vibration tests. The response characteristics of the inflatable dam, with and without the magnets attached, are sufficient to determine the level of their disturbance.

The instrumentation setup as shown in Figure 2.9 is very inexpensive and it is possible to be developed in great numbers. Several of these sensors are currently available (tested and calibrated). The whole idea, however, is not used further for the response measurements because of financial constraints in other parts of the research budget. Therefore, the minimum height of the dam of 5.1cm (2.5 inches) which now appears to be superficial, remains the same for compatibility concerns with all the preliminary tests (response data and visualization results).

2.4 Similitude

Geometric similarity between the model and the prototype is achieved with the *scale ratio*, L_r. Although a specific scale ratio is not required in this work, and in addition the facilities available restrict the choices even further (if a maximum aspect ratio, L/H, is to be attained), it

is proper to report its details. The scale ratio L_r is defined as in Daugherty *et al.* [50],

$$L_r = \frac{L_p}{L_m} \tag{2.2}$$

while other authors consider $L_r = L_m / L_p$. The reciprocal of the scale ratio is actually the *model ratio*, $\lambda = L_m / L_p$, or model scale. The subscripts "p" and "m" refer to prototype and model, respectively. Areas vary with L_r^2 and volumes with L_r^3.

Surface scaling here does not follow the same scale ratio, L_r. The bed roughness in the prototypes varies according to geological formations, as well as possible man-made works. However, this study does not attack the problem of the dam's vibrations with respect to the particular arrangement of a river bed. This can be the topic of another investigation. Therefore, the model channel bed is fabricated in such a way to induce and maintain a turbulent flow, so that the boundary layer is as thin as possible. This is accomplished with sandpaper self-adhesive strips across the channel bed. The effectiveness of this action is evaluated on the basis of laser-sheet flow visualization.

The surface of the prototypes' membrane is considered smooth. Similarly, the models have a very smooth surface for the membrane, which coincides with an approximate surface roughness scaling. Again, there are concerns that the model membrane surface must have an adequate roughness, to successfully simulate any flow separation phenomena that may exist in the prototypes. However, such a membrane material will depart from the requirements of being as thin as possible, creating other errors related to the vibration characteristics of the model.

The dimensions of the model, channel, and water level(s) are also scaled according to the scale ratio. Based on the maximum aspect ratios (L/H) possible in this setup (namely 9 and 29 as explained in previous sections), the two models may refer to scale ratios ranging from 9.4 to 45 for $L/H \approx 9$, and 8 to 34 for $L/H \approx 29$, if they are scaled with respect to the dam's length, L. If they are scaled with respect to the dam's height, H, then the scale ratios may range from 9.4 to 43, and from 8 to 33, for $L/H \approx 9$ and $L/H \approx 29$, respectively. The choice between length (L) or height (H) depends on whether there is an interest in the longitudinal or the cross-sectional response. Therefore, the results may be presented with separate scale ratios' application limits, depending on the response of interest.

Kinematic similarity is defined with a velocity ratio, $V_r = V_p / V_m$, which implies that a geometric similarity also holds. It is hardly ever used by itself, as whenever dynamic considerations are of interest then dynamic similarity is also used.

2.4.1 Dynamic Similarity

In a general problem, forces that may act on a fluid (or structural) element are those due to pressure F_p, viscosity F_v, gravity F_g, and elasticity F_e. For dynamic equilibrium to exist, the summation of all forces (the resultant) must be equal and opposite to the inertia force F_i. Therefore, all the force vectors must add to zero,

$$\mathbf{F}_p+\mathbf{F}_v+\mathbf{F}_g+\mathbf{F}_e+\mathbf{F}_i=0 \tag{2.3}$$

where $\mathbf{F}_i$=*-Resultant vector*. These forces may include a contribution from both structure and fluid elements. For a dynamic similarity to be achieved, then,

$$\frac{F_{p_p}}{F_{p_m}} = \frac{F_{v_p}}{F_{v_m}} = \frac{F_{g_p}}{F_{g_m}} = \frac{F_{e_p}}{F_{e_m}} = \frac{F_{i_p}}{F_{i_m}} \quad \therefore \quad \left(\frac{F_i}{F_g}\right)_m = \left(\frac{F_i}{F_g}\right)_p, \left(\frac{F_i}{F_v}\right)_m = \left(\frac{F_i}{F_v}\right)_p, \ldots \tag{2.4}$$

Of great contribution in the inflatable dam's vibrations are the inertia forces, the gravity forces, and the unsteady forces. Here, unsteady forces are considered to be time-dependent forces not already accounted for. This is made more clear later in equation (2.9).

It is assumed that viscous forces present are very small compared to inertia forces and therefore are neglected. This assumption remains valid as long as there is a high enough Reynolds number (**Re**=*VL*/ν) to maintain a fully-developed turbulent flow (in both prototype and model). The Reynolds number is related to the laminar/turbulent characteristics of the flow, and is interpreted as the ratio of inertia to viscous forces. Alternatively, it may be interpreted as the ratio of the flow of kinetic energy to the rate of mechanical energy loss (Gerhart and Gross [54]).

In a closed-conduit flow the typical Reynolds number for which turbulent flow is generally considered fully developed is **Re**>8000. For the case of an open channel, the range of 500<**Re**<2000 is considered transitional, and **Re**>2000 is generally considered fully-developed turbulent flow (Round and Garg [55], 1986). Solving for the minimum required velocity in the model tests, assuming that the governing length is the height of the upstream flow, where h_u=10cm, then,

$$V = \frac{\mathbf{Re}\,\nu_w}{L} = \frac{2000\times1\times10^{-6}}{0.1} = 2\,\text{cm/s} \tag{2.5}$$

Therefore, the model tests must be run with an upstream velocity of 2 cm/s or more for a water level of 10 cm, or with a velocity of

$$V_{\min} = \frac{20}{h_u}\,\text{cm}^2/\text{s} \tag{2.6}$$

where h_u is the upstream height in centimeters. All overflow tests are well above the minimum requirement of equation (2.6) and therefore it is considered that there is actually a turbulent flow. This flow characteristic is also verified by various visualization techniques.

Pressure and structural-elastic forces do exist in this problem, and in fact it may be possible that in certain cases they dominate the response of the inflatable dams. They could be considered, however, dependent on other variables and consequently neither a pressure coefficient **Cp** ($\mathbf{Cp} \propto F_p / F_i$) nor the Euler's number **Eu** ($\mathbf{Eu} \propto F_i / F_p$) is used, nor the Mach number **Ma** ($\mathbf{Ma} \propto [F_i / F_e]^{1/2}$). On the other hand, a new non-dimensional number may be introduced that will consider the effect of internal pressure and upstream water head, or even the dam's elastic properties. Elastic forces from the fluid element do not exist since water is incompressible. The dam's elastic forces are part of the structural stiffness of the dam, which is directly related to its response. A good response characteristic in this work is the frequency of vibration of the dam, or the maximum amplitude of oscillation, for example.

There are some concerns with respect to the Weber number, **We**, which relates the inertia forces with the surface tension forces ($\mathbf{We} \propto F_i / F_\sigma$). The Weber number is usually used to describe flows with a two-fluid interface. During the tests in this work as well as in other reports, nappe aeration resulted in complete vibration damping. The fact that there is full aeration, or stable air pockets are present in the stream, creates a fluid interface (air/water). Surface tension could be a factor in this phenomenon, and therefore caution should be exercised before interpreting such observations.

From equation (2.4), it can be deduced that the ratio of the inertia forces to the gravity forces, is the square of the Froude number, **Fr**,

$$\mathbf{Fr}^2 = \frac{F_i}{F_g} = \frac{\rho L V^2}{\rho g L^2} = \frac{V^2}{gL} \quad \therefore \quad \mathbf{Fr} = \frac{V}{\sqrt{gL}} \tag{2.7}$$

Alternatively, the Froude number can be derived directly from the Navier-Stokes equations and the continuity equation (Sabersky *et al.* [56]). The Froude number is generally used in flow systems with a free surface. For open channel flows the governing length is usually considered to be the water depth. In the case of a ship model, the ship's length at the water-line is considered the governing length. Therefore, in this case the height of the dam may also be a good governing length alternative, or the overflow height. The Froude number is considered one of the basic scaling laws in this work. One of the manufacturers reported that their model test results are based indeed on the Froude number (Bridgestone [10]), but unfortunately no further information was

made available. It was not possible to verify any type of experimental research of this kind from any of the existing companies.

Mathematical scaling of the conditions under which a response is measured, as well as the response itself, are very important, since this is a flow-induced vibration problem. Turbulence exists in the oncoming water stream but is also generated by the structure itself. Moreover, the highly turbulent characteristics of the flow at the downstream side of the dam further complicates the oscillation mechanisms. It is possible that initially stable phenomena may be amplified by the model's vibrations to create an unstable oscillating system, of fluid and structure. Alternatively, otherwise simple turbulent flow becomes part of a dynamically unstable structure.

Considering a single oscillator in a flow field, the classical equation of motion may be written as

$$(k+k_w)x + (c+c_w)\dot{x} + (m+m_w)\ddot{x} = F_w(t, x, \dot{x}, \ddot{x}) \tag{2.8}$$

where subscript w refers to the parameters added by water (Kolkman [57], 1989). Theoretically these added parameters may be positive or negative, something that could create an unstable system (i.e. a negative damping coefficient). If the dominant excitation frequency f is known, then the Strouhal number, **St**, may be established. Although the Strouhal number is largely associated with the frequency of vortex shedding behind a cylinder and its resulted vibrations, it will be used here in a similar way. The dominant excitation frequency comes from the non-stationary part of the total force F_w,

$$F_w = \bar{F}_w + F'_w \tag{2.9}$$

where $\bar{F}_w$ is the time-averaged (static) part, and F′ is the time-varying (dynamic) part. The excitation and primary oscillation frequency f, the governing length L, and the stream velocity V define the non-dimensional Strouhal number,

$$\mathbf{St} = f\frac{L}{V} \tag{2.10}$$

The governing length, in this case, could be the dam's height or the dam's length, depending on what type (transverse or longitudinal) of vibration the Strouhal number refers to. The governing length in other problems may be the upstream water head or just the height (diameter) of the structure. However, in this problem considering the upstream water depth or only the dam's height is certainly not sufficient, and it can lead to misinterpretations.

The latter, as well as other non-dimensional numbers mentioned earlier, may be derived from the Navier-Stokes equations of motion. It will be shown that the Strouhal number is a measure of the ratio of unsteady forces to inertial forces.

The general form of equations of motion for Newtonian fluids (linear relationship between the viscous stress tensor and the rate of deformation tensor), is given by the Navier-Stokes-Duhem equations, equation (2.11), which are presented here in their vector form and indicial notation

$$\rho\frac{D\mathbf{v}}{Dt} = -\nabla p + (\lambda+\nu)\nabla(\nabla\mathbf{v}) + \mu\nabla^2\mathbf{v} + \rho\mathbf{f}$$

or (2.11)

$$\rho\dot{v}_i = -p_{,i} + (\lambda+\nu)v_{j,ji} + \mu v_{i,jj} + \rho f_i$$

form. Assuming incompressible flow, $v_{i,i}=0$, the Navier-Stokes equations for incompressible flow are obtained. Also, considering only the equation in the x direction (Cartesian coordinate system), and that $\nu=\mu/\rho$, where ν is the kinematic viscosity, μ is the viscosity, and ρ is the density of the fluid, then

$$\frac{\partial u}{\partial t} + u\frac{\partial u}{\partial x} + v\frac{\partial u}{\partial y} + w\frac{\partial u}{\partial z} = -\frac{1}{\rho}\frac{\partial p}{\partial x} + \nu\left(\frac{\partial^2 u}{\partial x^2} + \frac{\partial^2 v}{\partial y^2} + \frac{\partial^2 w}{\partial z^2}\right) + f_x \tag{2.12}$$

The equation may be re-written by introducing the non-dimensional variables

$$u^* = \frac{u}{V_o}, \quad x^* = \frac{x}{L_o}, \quad t^* = \frac{t}{T_o} = tf_o, \quad p^* = \frac{p}{p_o}, \quad \text{... etc.} \tag{2.13}$$

giving,

$$f_o V_o\frac{\partial u^*}{\partial t^*} + \frac{V_o^2}{L_o}\left(u^*\frac{\partial u^*}{\partial x^*} + v^*\frac{\partial u^*}{\partial y^*} + w^*\frac{\partial u^*}{\partial z^*}\right) =$$

$$= -\frac{1}{\rho}\frac{p_o}{L_o}\frac{\partial p^*}{\partial x^*} + \nu\frac{V_o}{L_o^2}\left(\frac{\partial^2 u^*}{\partial x^{*2}} + \frac{\partial^2 v^*}{\partial y^{*2}} + \frac{\partial^2 w^*}{\partial z^{*2}}\right) + f_x \tag{2.14}$$

Multiplying equation (2.14) by L_o/V_o^2, and considering that the x direction may as well be the gravity direction so that f_x=g, results in equation (2.15). Equation (2.15) shows the relation of several non-dimensional numbers, all of them discussed earlier. The Strouhal number, **St**, also shown, may also be interpreted as the ratio of the time scale of the flow to the time scale of the oscillating boundary (Gerhart and Gross [54]). The oscillating boundary in this problem is the

$$\mathbf{St}\frac{\partial u^*}{\partial t^*}+\left(u^*\frac{\partial u^*}{\partial x^*}+v^*\frac{\partial u^*}{\partial y^*}+w^*\frac{\partial u^*}{\partial z^*}\right)=$$

$$=-\mathbf{Eu}^{-2}\frac{\partial p^*}{\partial x^*}+\mathbf{Re}^{-1}\left(\frac{\partial^2 u^*}{\partial x^{*2}}+\frac{\partial^2 v^*}{\partial y^{*2}}+\frac{\partial^2 w^*}{\partial z^{*2}}\right)+\mathbf{Fr}^{-2} \tag{2.15}$$

dam's membrane which exhibits localized vibrations, or membrane "undulations". An oscillating boundary in this case may also be the water free surface, where nappe instabilities occur as mentioned in the literature review in Chapter One. Parenthetically, these nappe instabilities should not be associated with any wave generation (which do not exist), but rather the dam's oscillation.

The Strouhal number may be an independent dimensionless parameter if the excitation frequency f is an independent parameter. However, if the frequency is a dependent variable as in the case of vibration of cylinders perpendicular to flow, or vibration of suspension bridge cables, then the Strouhal number is a function of the other parameters of the problem. In the well-investigated case of flow around a cylinder, the vibration frequency is dependent on the Reynolds number, for **Re**<1000 and **Re**>100,000 (Blevins [48], 1990). In the present problem, flow visualization showed no vortices shed after the dam, but chaotic flow instead. Therefore, it is possible that the dominant vibration frequency is structurally driven and not associated with any fluid periodic motion. In such a case, it is acceptable to assume that the Strouhal number is independent of any viscous effects and consequently the Reynolds number. However, should the mechanism of vibrations also include flow separation near the downstream base of the dam able to drive or perturb the dam to large oscillations, then the results may depend on viscous effects.

Considering the case that the primary non-dimensional parameters are at least based on the Froude and the Strouhal laws, two relations are made available for the scale ratio L_r. Starting from these two numbers (which are equal for both model and prototypes), then

$$\mathbf{Fr}=\left(\frac{V}{\sqrt{gL}}\right)_p=\left(\frac{V}{\sqrt{gL}}\right)_m \qquad \therefore \qquad \frac{(gL)_p}{(gL)_m}=\frac{V_p^{\,2}}{V_m^{\,2}}$$

$$\mathbf{St}=\left(f\frac{L}{V}\right)_p=\left(f\frac{L}{V}\right)_m \qquad \therefore \qquad \frac{L_p}{L_m}=\frac{f_m V_p}{f_p V_m} \tag{2.16}$$

Gravity acceleration g is the same for model and prototype; therefore, the gravity acceleration ratio g_r is always a unit value. Combining the results in equations (2.16),

$$\text{(a)}\quad \sqrt{\frac{(gL)_p}{(gL)_m}} = \frac{f_p}{f_m}\frac{L_p}{L_m}, \qquad \text{(b)}\quad \frac{g_m}{g_p}\frac{V_p^2}{V_m^2} = \frac{f_m}{f_p}\frac{V_p}{V_m} \tag{2.17}$$

From equations (2.17), the following very useful equation is derived:

$$f_r = \frac{f_p}{f_m} = \left(\frac{g}{V}\right)_r = \left(\frac{g}{L}\right)_r^{1/2}$$
$$\text{for } g_r = 1 \quad \therefore \quad f_r = V_r^{-1} = L_r^{-1/2} \tag{2.18}$$

where L_r is defined in equation (2.2) and $V_r = V_p / V_m$. With the use of equation (2.18), the frequency of oscillation from the model measurements can be translated to prototype values. In dealing with the Froude and Strouhal numbers, it must be emphasized that the first is a requirement for model scaling, while the other is a scaling of the model test's results. Therefore, it is not a surprise that the Froude number does not affect the scaling law, as demonstrated in the next section in Table 2.1.

2.4.2 Scale Ratios

The most important parameters in this problem are set to be the Froude number and the Strouhal number. It is assumed that the statement holds true as long as the model flow is a fully-developed turbulent flow, as is the case for the prototype.

The following table is developed to assist in the quick interpretation of any model quantity to the corresponding prototype quantity. The first two columns show the scale ratios related to the Froude number and the second with the Strouhal number. It is assumed that the Strouhal number remains independent of the Reynolds number, otherwise the combination of the latter with the Froude number creates the requirement of a unity scale ratio. The third column shows the scale ratios when both Froude number and Strouhal number are considered, as was done for the derivation of the frequency ratio, in equation (2.18).

It is clear that combining the two numbers (Froude and Strouhal) does not result in any advantage over the use of the Froude number alone. Alternatively, the problem may be approached with dimensional analysis, or with statistical analysis applied directly to the results.

Table 2.1 Similitude scale ratios on Froude and Strouhal Laws

Quantity	Dimension	Froude Law (general)	Froude Law $g_r=\rho_r=1$	Strouhal Law (general)	Strouhal Law $g_r=\rho_r=1$	Froude and Strouhal Law
Geometric						
Length	L	L_r		L_r		L_r
Area	L^2	L_r^2		L_r^2		L_r^2
Volume	L^3	L_r^3		L_r^3		L_r^3
Kinematic						
Time	T	$(L/g)_r^{1/2}$	$L_r^{1/2}$	f_r^{-1}		$(L/g)_r^{1/2}$
Velocity	LT^{-1}	$(gL)_r^{1/2}$	$L_r^{1/2}$	$(fL)_r$		$(gL)_r^{1/2}$
Acceleration	LT^{-2}	g_r	1	$(f^2L)_r$		g_r
Discharge	L^3T^{-1}	$(gL^5)_r^{1/2}$	$L_r^{5/2}$	$(fL^3)_r$		$(gL^5)_r^{1/2}$
Frequency	T^{-1}	$(g/L)_r^{1/2}$	$L_r^{-1/2}$	$f_r=(V/L)_r$		$(g/L)_r^{1/2}$
Dynamic						
Mass	M	$(\rho L^3)_r$	L_r^3	$(\rho L^3)_r$	L^3	$(\rho L^3)_r$
Force	MLT^{-2}	$(\rho g L^3)_r$	L_r^3	$(\rho f^2 L^3)_r$	$(f^2L^3)_r$	$(\rho g L^3)_r$
Pressure	$ML^{-1}T^{-2}$	$(\rho gL)_r$	L_r	$(\rho f^2 L^2)_r$	$(fL)_r^2$	$(\rho gL)_r$

Chapter Three

INSTRUMENTATION

Frequently, experimental work requires the development of specialized measurement techniques and instruments. It is no surprise that the response measurement of an unusual structure, such as an inflatable dam, requires unusual instruments. This chapter gives a detailed description of the instrumentation practice and the measurement techniques used. Discussion of measurement error for each instrumentation and for measured quantities is also presented.

3.1 Measurement Techniques

The literature review (in Chapter One) showed that previous workers used strain gages and depth gages. Strain gages were used to measure the membrane's strain at selected points. Point gages were used to measure maximum displacements during vibrations, static deformations under various loading cases, and water levels (upstream, downstream, and overflowing).

It was not mentioned whether the strain readings were logged as a time series or just maximum values. Assuming that a time-log was the case, strain readings are an excellent source of information of the membrane force's magnitude and oscillation frequency. The drawback is that the strain gage itself has the effect of causing a local stiffening on a model material that is only a few thousands of an inch thick. Moreover, the adhesive used to fix a strain gage adds to the stiffening of the area. As a result, the magnitudes recorded are not representative of reality. Furthermore, the structural behavior of the dam may be significantly altered, depending on the number of strain gages used and their stiffening effect.

One more drawback is that at large-amplitude vibrations the membrane undergoes stretching and bending cycles. Because of the eccentricity of the bending plane of the strain gage, these bending cycles will also have an effect on the final reading. Therefore, it is impossible to distinguish between strain readings representing bending stresses and in-plane stresses.

Except for the structural response measurement, the direct or indirect measurement of the excitation forces is also required. Pressure taps on the surface of the dam could provide very useful information on pressure distribution. However, the tubing and taps would interfere with the model characteristics again. As mentioned in the previous chapter, laser velicometry in the vicinity of the dam surface is not feasible either, because of large membrane displacements. Therefore, the response measured in this work is only related to the upstream average velocity, V, and the upstream water head, h_u.

3.1.1 Internal Pressure Variations

Instead of strain variations, pressure variations are used here to determine the primary oscillation frequency. The maximum static internal pressure applied in the model dam is approximately 1.5 psi (approximately 100cm of water head). However, most of the test cases have an internal pressure not exceeding two times the upstream water head (0.3 psi). Nevertheless, even at the pressure level of 1.5 psi, air is generally considered incompressible. This can be demonstrated with the *general gas law*,

$$\frac{P_1 V_1}{n T_1} = \frac{P_2 V_2}{n T_2} = R \tag{3.1}$$

from the *ideal gas law* $PV=nRT$, where P is pressure, V is volume (for this equation only), T is temperature, n is the number of moles[1], and R is the *gas constant.* In deriving equation (3.1) it was assumed that the quantity of gas (i.e. the number of moles n) is constant, which is the case for sealed containers such as inflatable dams.

A cylindrical air-inflated membrane at internal pressure p_i, produces a membrane tensile stress of $p_i\, r/t$ per unit length. For a radius r=1.25 inches (3.175cm), a thickness t=0.5 mils (0.013mm), and a pressure variation of δp_i=0.07 psi maximum, the circumferencial tensile stress on the membrane is 175 psi (1.21 N/m^{m2}). The strain resulting for a modulus of elasticity E=550

[1] Mole (mol) is the amount of substance that contains the same number of atoms as there are in 12 grams of carbon-12 isotope.

ksi (Mylar(R)) is 0.00031, which results in a circumferencial extension of 2.4 mils (0.061mm). The area increase is of the order of 0.06%.

Assuming that there are no other volumetric or temperature changes, the pressure difference resulting from a volumetric change of 0.06% is also 0.06%. This translates approximately to 4.2×10^{-5} psi, which is too small to be read from the instrumentation used. Such a pressure level represents a signal level of $3\mu V$, which is smaller than the minimum noise level produced by the pressure transducers. Therefore, any volumetric change resulting from the model's material extension is negligible. Consequently, any pressure variations logged are considered to be solely due to volumetric changes resulting from other causes. If it is also assumed that there are no temperature variations, then it is concluded that the pressure variations are only a function of the cross-sectional shape of the dam. This conclusion is not restricted to a two-dimensional response, and it may be extended to longitudinal and cross-sectional shape deformations for a 3D response.

The instrumentation required for acquiring pressure variation data consists of a low level pressure transducer, and a suitable signal amplifier. During the first phase of tests, two transducers are used. The first is placed inside the dam and the other outside the dam. The outside transducer is connected with a tubing length of 13cm (5 inches), and 1.6mm (1/16 inch) internal diameter. True pressure levels are considered to be the levels registered by the internal transducer. The inflatable dam model has only 54.5cm (21.5 inches) length and therefore traveling pressure waves are assumed to be negligible. The assumption is further supported by the fact that there are no significant three-dimensional responses observed.

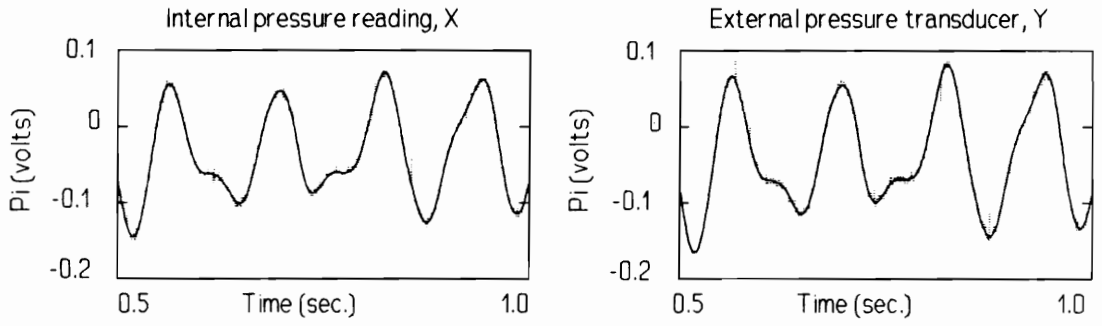

Figure 3.1 Internal pressure variations, $P_i/h_u=3.5$, $h_o=0.25H$, $h_u=1.3H$, upstream velocity $V=2.8H$/s, and dam height $H=6.2$cm. [C13]

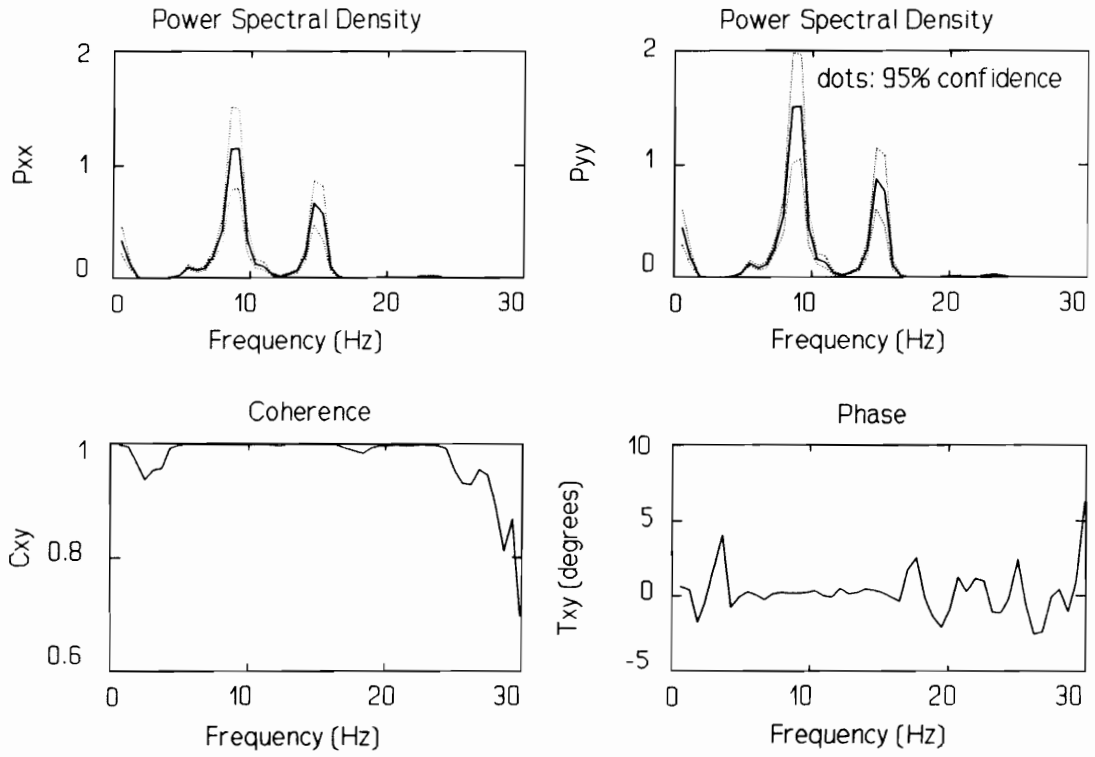

Figure 3.2 **Analysis of internal pressure variations, P_i/h_u=3.5, h_o=0.25H, h_u=1.3H, V=2.8H/s, and dam height H=6.2cm.** [C13]

Comparing the signal outputs of the two transducers, it is shown that there is little to no apparent difference between the two signals (Figure 3.1). Power spectrum analysis on both signals leads to the same conclusion (Figure 3.2). If it is assumed that the one signal ("Internal pressure reading, X") is the input of a system, and the second ("External pressure transducer, Y") is the output of the same system, then the "system response" may be determined. Obviously the "system's" primary parameters here, are the tubing length and diameter.

Comparison of the graphs in Figure 3.3 and Figure 3.4 shows that the conclusions are valid for different input waveforms, or oscillation frequencies. This point can be made clearer if an exciter is available, driven by a random function (white noise). Spectral analysis of those response signals can show a continuous spectral function with respect to the frequency range of interest.

As expected, the output shows no variation in the frequency spectrum analysis, but there is certainly some degree of phase shifting (Figure 3.2 and Figure 3.4). At the frequency region of interest (6 to 16 Hz), this phase shifting is less than 1/2 of a degree with an apparently random

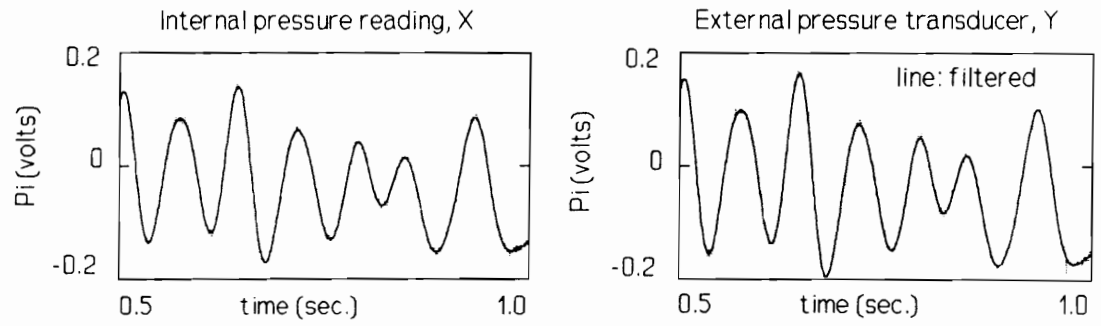

Figure 3.3 **Internal pressure variations, P_i/h_u=2.8, h_o=0.25H, h_u=1.3H, upstream velocity V=2.8H/s, and dam height H=6.2cm.** [C14]

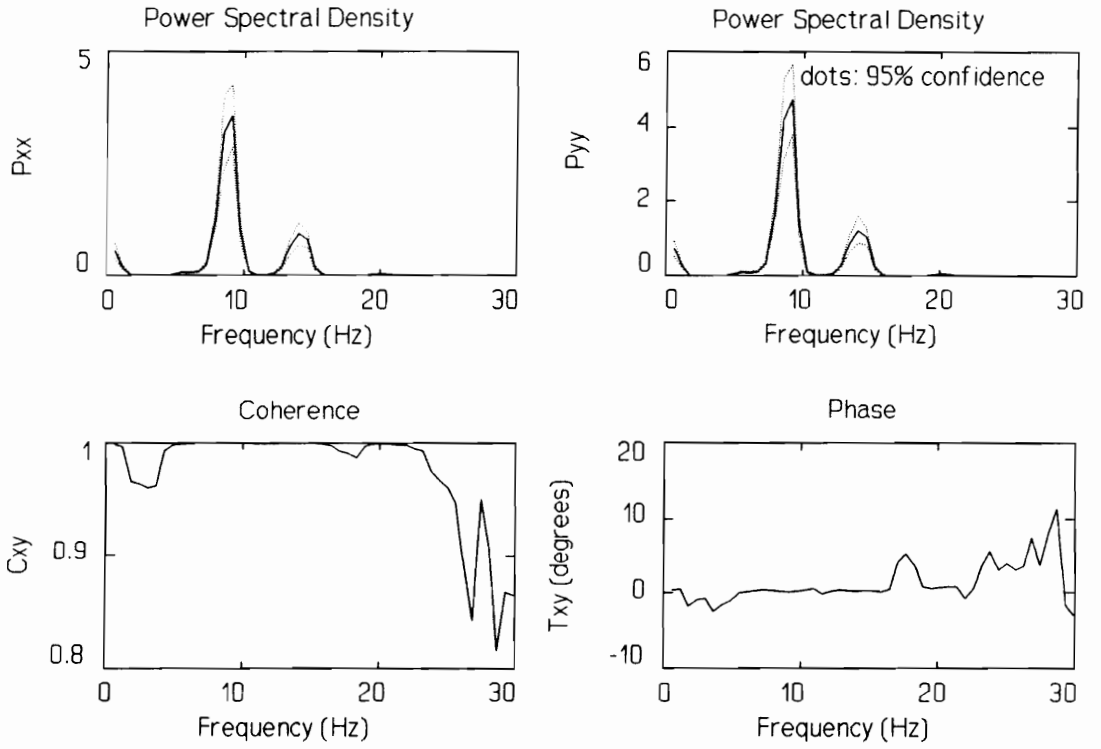

Figure 3.4 **Analysis of internal pressure variations, P_i/h_u=2.8, h_o=0.25H, h_u=1.3H, V=2.8H/s, and dam height H=6.2cm.** [C14]

variation about its mean. The conclusion is even further strengthened by observing the coherence distributions. Again, over the frequency region of interest the coherence is better than 99% which is considered an excellent result by all means. "Frequency region of interest" is the frequency range where the primary frequency of oscillation appears. The results presented are based on 90% overlapping windows, with a Hanning-window function.

Similar analyses for all the tests in the water-tunnel facilities (over 63 combinations), lead to similar conclusions. Variations of the maximum signal phase shifting and coherence vary according to the amplitude of internal pressure variations. Higher amplitude levels tend to have much less phase shifting and much better coherence. The graphs also show the 95% confidence range of the power spectral densities. The power spectra here exhibit a crude resolution which is a direct result of the number of data samples. However, the frequency components presented in later chapters are extracted with special curve-fitting processes.

Concluding, the practice of this work to use the 13cm (5 inch) length, 1.6mm (1/16 inch) diameter tubing is acceptable with respect to the frequency and phase response characteristics of the signal. Therefore, the pressure variation measurements may be adequately compared with other response measurement methods of displacement. Furthermore, the model construction is greatly simplified, allowing multiple models to be prepared and cured well before they are needed. In addition, comparisons may be made from pressure transducers placed at each end of the dam for detection of longitudinal pressure waves based on the phase lag of the two input signals. One more advantage of the use of pressure signals is that the acquired volume of data is much smaller for the volume of information they produce. This substantially reduces the data storage requirements and computer processing time.

3.1.2 Stream Velocity Measurements

Velocity measurement of a stream can be accomplished by many ways. Perhaps the most accurate point measurement method is Laser Doppler Velicometry (LDV), or Particle Image Velicometry (PIV). The simplest method and possibly most crude is the floating body method. LDV requires an enormous amount of time for setup and is usually used to measure velocity components in the vicinity of submerged bodies. PIV would have been an excellent method for this application, if the equipment were available. With PIV, an unlimited number of points from suspended particles in water, or from the lit cross-section of the dam, can be identified simultaneously. Therefore, the stream average velocity, the 2D flow pattern and the 2D membrane velocities can be identified. Setting-up the several light-sheet sequences along the dam, a 3D picture will be available.

The floating body method may be used for average velocity reading in flumes where the velocity does not exceed 50 cm/s (Yang [58]). This is one of the methods used here. As an improvement with respect to the time recording device, a video camera and a timer system with

better than 1/100th of a second accuracy are used to record the floating body's path.

The float method may provide good measurements when the flow is uniform with a minimum of surface disturbances (waves), which is the case here. The average velocity V is generally 0.85±0.05 of the float velocity (Daugherty [50]), depending on the boundary layer. Another method for determining the average velocity V, is by averaging the velocities at $0.2h_u$ and $0.8h_u$ (Roy [59]), if pitot tubes were useful. However, since the velocities here are as low as 5cm/s the pitot tubes are useless. Instead, hydrogen bubbles are used as suspended travelling particles. The process requires high water salinity which renders it catastrophic for the dam's metal supports. Alternatives to salt additive are available but at a high cost.

The method used for the primary average stream velocity measurement, involves the time a given volume of water takes to discharge from the pipe system outlet. A point gage provides the water depth measurements two feet from the dam. Readings of the point gage are recorded through a miniature CCD camera positioned 2.5cm (1 inch) from the gage, resulting to a better than 0.0063mm (0.00025 inch) accuracy. This method is proven to be very dependable, and perhaps most important, there is no concern about calibrating the system, since the method is a basic calibration technique.

This type of flow rate measurement method, though primitive as is the floating method, is unquestionably the true average velocity measurement, as defined by the average velocity relationship,

$$V=\frac{Q}{A} \tag{3.2}$$

where V is the average velocity, Q is the flow rate, and A is the water cross-sectional area. The flow rate is calculated from the volume/time readings, and the cross-sectional area is calculated with the point-gage readings. There are many other methods for flow rate measurement but they all require considerable calibration procedures which brings us again to the method used here.

As an example of the theory that does not always apply to practice, another method is temporarily used. A pitot tube is placed at the outlet of the pipe recirculation system. The pipe is elevated from the bottom of the channel, so that the outflow is always unrestricted, thus eliminating any possible errors. With the pitot tube positioned exactly at the pipe's edge, the velocity equation is simplified to,

$$V=\sqrt{\rho g h} \tag{3.3}$$

where ρ is the water's density, g is the acceleration of gravity, and h is the pitot tube water head. Equation (3.3) may be derived from Bernoulli's equation upon recognizing that around the water jet there is atmospheric pressure, and therefore the location of the pitot tube in the cross sectional plane is irrelevant. Moreover, it is further assumed that the effect of flow disturbance is marginal. Based on actual results, however, this pitot arrangement does not work as assumed, and basic calibration is necessary again.

3.1.3 Statically Deformed Shape

The static deformation shape of the model is measured by point gages. The accuracy of the gages is better than one mil (0.001 inch). The method is simple and very reliable to warrant extremely accurate results. This is an extremely time-consuming process and it is only used for preliminary results. In the case of continuous vibrations the method is good only for average readings, and its accuracy drops dramatically.

3.1.4 Dynamic Displacements

Traditionally, structural response is measured in displacement, velocity, or acceleration of strategically chosen points on the structure. The inflatable dams (prototype and models) were reported to have large-amplitude low frequency oscillations. It is therefore appropriate that displacement measurements are chosen to be acquired.

Three separate methods were developed for this task. The first is based on an infrared beam, which produces a voltage output as a function of the width of the beam. Extension arms are required to support a light barrier in order to avoid light dispersion from the free surface (Figure 3.5). Inherently, the extension/light barrier adds a small weight on the dam, which is made with lightweight material to have only a marginal effect.

During large oscillations the light barrier vibrates at the same frequency as its base, the model. Therefore it is necessary to be able to distinguish between the base-driven vibrations and the light-barrier induced vibrations. As a result, this method is only used for free vibrations to verify or calibrate the other instrumentation, where the light-barrier is not used.

The second instrumentation is the Hall-effect 3D displacement transducer, whose principle setup is shown in Chapter Two. A permanent magnet is required on the membrane. The additional

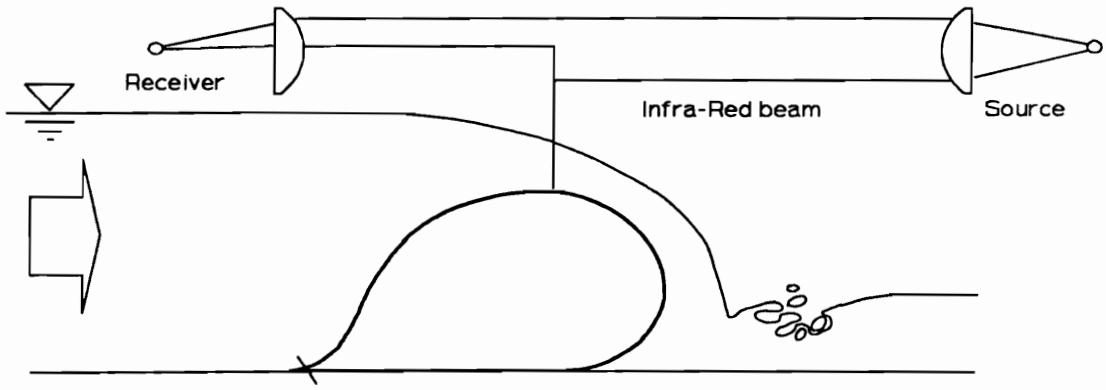

Figure 3.5 Principle setup of the use of the Infra-Red beam displacement transducer on the inflatable dam models.

weight (0.2 grams) did not show any structural response changes. This was tested with the infra-red optoelectronic instrumentation described before, by testing the models with and without the magnets in position.

The video and timer setup used for velocity measurements is the third method used. The video tapes are searched at slow motion and it is possible to identify the primary frequency components. Regardless of a bad frame resolution (only 29.9 frames/sec.), these slow motion movies are an excellent source of information not only for the primary vibration frequency but also for the mode of vibration and maximum oscillation amplitudes.

3.2 Instruments and Sensors

Data acquisition is primarily performed with an Analog Device TI-860 A/D (analog to digital) card, plugged in a simple PC 80286/87 compatible machine. The data acquisition card has a 12-bit resolution, resulting in a 2.5mV minimum voltage resolution, in a ±5V possible range. The throughput sampling capacity of the A/D card can reach 250kHz, which was proven to be plentiful even when all 16 single-ended inputs were used. The sampled data (in ASCII) are post-processed on other available machines, usually on 32-bit PC compatible computers with hardware and software supporting full IEEE arithmetic.

Another instrument used occasionally for real-time data acquisition is a Hewlett Packard 3562A Dynamic Signal Analyzer. It has a 0.064mHz to 100kHz range, with span/800 resolution, a 10.24mHz to 100kHz possible span at 800/span seconds, and a ±0.015% absolute accuracy. Most measurements were stored on magnetic media through an IEEE-488 (HPIB) interface, for comparison with the post-processed results.

3.2.1 Instrumentation Amplifiers (IA)

There are many practical methods for voltage signal amplification [60-62], but the instrumentation amplifier is the one predominantly used. This is primarily due to the very high impedance (10^{12} ohms) in both inputs, and due to its ability in achieving third and fourth order amplifications without significant side-effects. It is compatible with single-ended signals, but in such a case the non-inverting single op-amp configuration is used instead.

Instrumentation amplifiers are readily available by several manufacturers in a single integrated circuit (I.C.) with excellent response characteristics [63, 64]. It is cost effective though (10 to 100 times less than the I.C. IA value) to develop the instrumentation amplifiers from basic

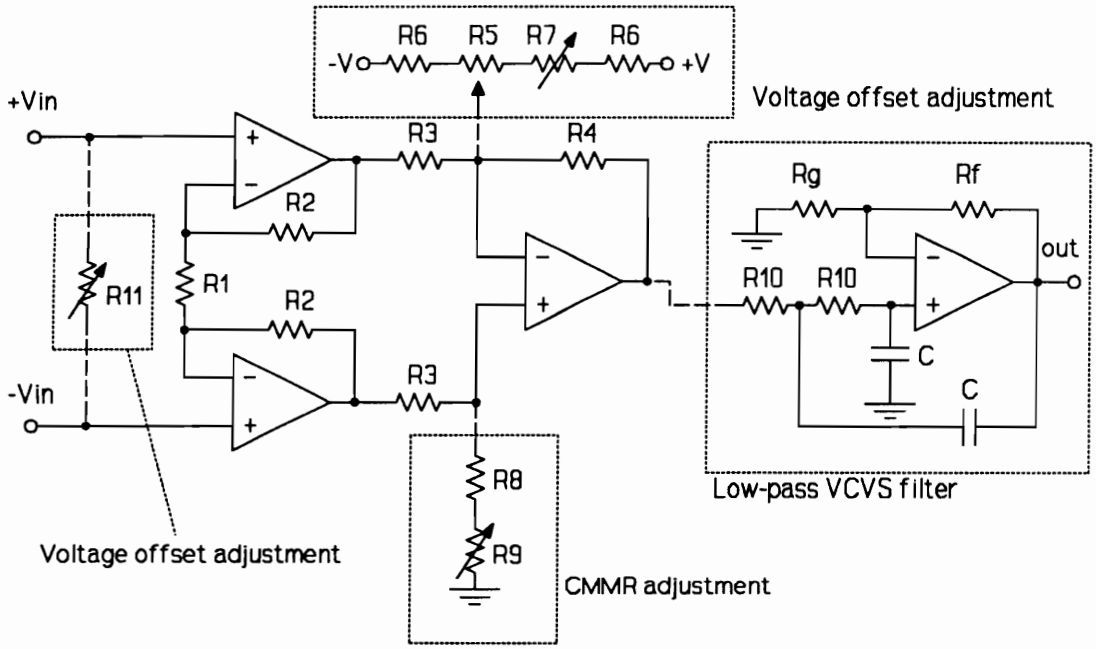

Figure 3.6 Basic schematics of the instrumentation amplifier and signal control circuits, used in various instrument end-products.

components, especially if an exact amplification magnitude is not a primary concern. The basic building block used throughout this work is shown in Figure 3.6, with several added control circuits (in the dotted-line boxes).

The governing equation (network equation, transfer function) is well known and is available in many references (Carr [62]) as,

$$A_v \doteq \frac{E_{out}}{E_{in}} = \left(2\frac{R_2}{R_1} + 1\right)\frac{R_4}{R_3} \tag{3.4}$$

where A_v is the voltage gain, E_i is voltage differential (V-volts), and R_i is resistance (Ω-ohms). From this basic building block, simple or complex add-on circuits may be used to control its response according to specific needs.

In this work the IA is used with differential voltage sources as the Wheatstone bridge, and with pressure transducers equipped with active piezoelectric diaphragm. Amplifications used in these cases are 10 and 500, respectively. The supply voltage (not shown in Figure 3.6) is from a ±5V power supply, and therefore the useful range of the IA is limited within that range.

The operational amplifiers used here are based on the TL074 I.C. [65], which is classified as a low-noise JFET-input quad op-amp. The JFET (Junction Field Effect Transistor) technology provides the high input resistance (10^{12} ohms) so useful in this case. It has a high slew rate of 13V/μs, suitable for dynamic signals of much higher frequency than what is found in the response of the dam's models. In fact, the frequency of vibration of inflatable dams is so low that almost any inexpensive operational amplifier would be sufficient (like the well known 741).

3.2.2 Pressure-Signal Amplifier/Filter

It was shown in an earlier section that the pressure variations inside the model dam are very small. The pressure transducers used (ENDEVCO(R) series 8510B) are suitable for a pressure range of 0-2psi. Their sensitivity is typically 150(±50)mV/psi. Therefore, at an internal pressure of 1.5 psi maximum applied pressure, the transducer output is 225mV. However, the pressure variations being two to three orders of magnitude smaller than the average pressure, would not even register in the A/D card, unless properly amplified. It is therefore required that the signal is first shifted to a zero mean, and then amplified by a factor of approximately 500.

Ideally, this would first require the use of a preamplifier/conditioner, to adjust the signal to zero voltage and reject a given bandwidth. In this case the rejected bandwidth requires the use of a low-pass filter, that would cut off the noise inherently produced in the signal by the pressure transducer. This noise is typically 5μV with a maximum value of 50μV (dc to 50kHz). Amplified by 500, the noise will appear as 2.5-25mV signal interference.

For practical reasons the order of signal conditioning stages is changed, with the low-pass filter being at the end of the modules arrangement. The filter used is a Voltage-Controlled Voltage-Source (VCVS) active filter of the Sallen and Key realization type, employing a 4th order low-pass Bessel approximation function. Many other approximation functions are possible with the VCVS Sallen and Key type, but the Bessel function is chosen for its particularly favorable

dynamic transfer characteristics. Of primary interest is the immunity of the Bessel approximation to self-oscillate in a step-function, a problem commonly known as ringing [66].

3.2.3 VHS Camera with 1/100s Timer

Some NTSC-standard VHS-type home video cameras, have a frame grabbing frequency of 29.9 frames per second. This means that each frame contains a theoretically possible maximum time of approximately 0.03 seconds of events. Therefore a vibrating body with a response frequency higher than 15Hz (the Nyquist frequency) would very well be an excellent example of aliasing. From preliminary tests on the inflatable dam models in the 61cm (2 feet) wide water tunnel/channel, it was shown that the response of the dam was ranging from 5 to 25 Hz. As a result, this video camera was of little use in getting accurate vibration information.

It is possible, though, to get very accurate velocity measurements of a travelling body if a suitable timer is used. An internal real-time VCR can provide an exact time interval with only an initial and final frame error associated with the frame-grabbing time-delay of the camera. However, since such video cameras are generally not available, then an external time reference is necessary for a typical camera to be useful in this regard.

The timer developed here provides this time reference with an accuracy of 0.01 seconds. Higher precision requires only the addition of extra sets of components. Four digits provide a 10s to 1/100s counter, complimented with a 1/100 second bar graph. There are four 7-segment LEDs (Light Emitting Diode) and a ten LED bar display. The fourth digit and the LED bar are synchronized but half a cycle. This feature makes possible an accuracy of 0.005 seconds, when it is possible to read the fourth digit.

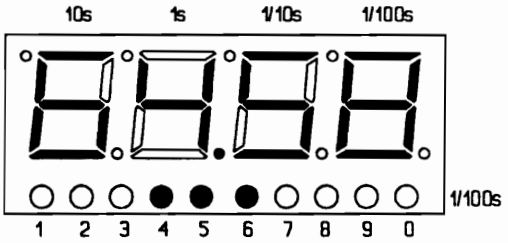

Figure 3.7 External video-camera timer layout, yielding 1/100s video accuracy.

The electronic circuit is based on decades-old technology. However, it is designed in a way not available in the market as consumer electronics or technical reference. It is a hybrid CMOS (Complementary Metal Oxide Semiconductor), TTL (Transistor-Transistor Logic) and special function circuit. An I.C. timer generic device number 555, is the heart of the instrument. The timer is set in the astable configuration, providing a continuous pulse (square wave).

The frequency of oscillation is a function of the resistors and capacitor present, with an approximate formula (Berlin [67]):

$$f=\frac{1.443}{(R_1+2R_2)C}\ \text{Hz}, \qquad \%\ \text{duty cycle}=\frac{R_1+R_2}{R_1+2R_2}\times 100\ . \tag{3.5}$$

It is calibrated with the potentiometer available (R_1), to a very precise timing. Because the 555 is a very stable circuit, the signal does not shift significantly (±1 second per 5 minutes) from its calibration point.

Figure 3.8 shows the timer schematics. There is only one 7-segment LED shown, where the carry-out signal of n/10 goes to the next module and so on. It is obvious that it is a matter of simple repetition of this module to create as many digits, and as a result, as much accuracy desired. Using the quad-NOR gate to synchronize the CMOS counter/divider 4017, and the TTL decade counter 74LS90, creates the half a pulse lag mentioned before.

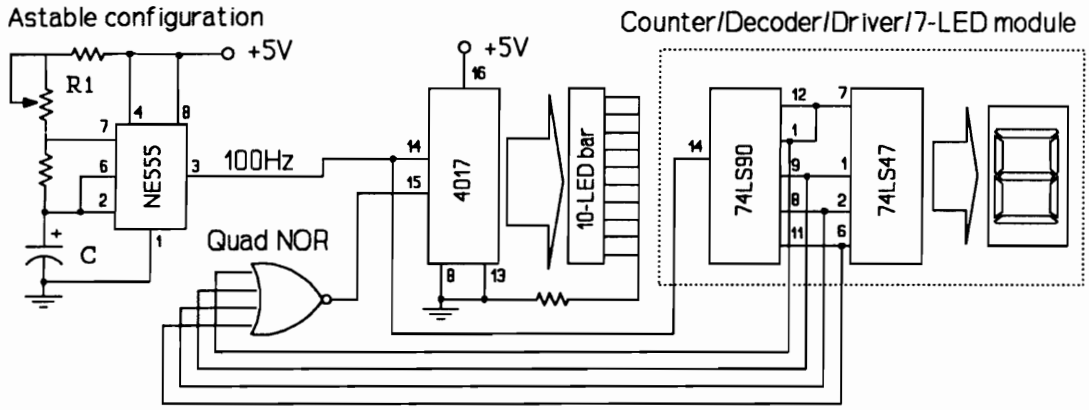

Figure 3.8 Partial circuit schematics of the Video Timer.

Alternatively, the same instrument (timer) may be designed based on readily available clock/timer I.C.s that incorporate the timer and 7-segment LED drivers all in a single chip. Such chips are more expensive but require much less time to be designed and be assembled. Moreover, the more chips (especially TTLs) the more the current requirement, to the point that a dedicated power supply is unavoidable.

3.2.4 Instrumented Impact Hammer

This instrument is required for free vibration tests to provide a measured excitation method. From modal analysis and testing experience [68], impact excitation is the simplest method to use. The "hammer" is made with an aluminum shaft, and the force sensor is made with a passive piezoelectric force transducer. Because of the use of a cantilever type of sensor, the resulted signal level is up to 15V for relatively small magnitude excitations.

3.2.5 Support Instruments

Numerous other instruments were developed that had only a support role in the data acquisition process. These include a sinusoidal, square, and triangular function generator based on the XR2206 I.C. (EXAR [69]), with variable frequency, amplitude, mean, and curvature. The developed function generator was primarily used to verify the input/output relationship (or transfer characteristics) of the other circuits.

Other instruments include a 3D-axis-system automatic calibration base. It is developed based on manual xyz traversing platforms. Motion control is established through geared DC motors (available as power screw-drivers), and an elaborate DC motion control circuit. The main purpose of this instrument is to calibrate the 3D displacement transducers which require repetitive calibration at 30x30x20 grid paths.

A 32 to 16 channel multiplexer based on the CMOS 4053 is also developed to make possible multiple input signals to fit into the 16 channel data acquisition card. The 4053 chips are analog multiplexers which are controlled (ON/OFF) by a simple square wave input. This makes it particularly simple to be synchronized with the D/A card, as long as a carry out pacing signal is available.

A power supply is the foremost important support instrument. Several units are made available to accommodate the needs of this work. The basic philosophy behind their development is that each individual instrument regulates the voltage supply on its own circuit board. This way heavy duty voltage regulators are not needed, and (most important) the voltage supply of the instruments does not pick up noise through long wire lines.

3.3 Measurement Error

This error is associated with the measurement technique, the transfer characteristics of the signal conditioning/amplification instruments, and sometimes with the limitation of the sensor itself. It is necessary to provide such information, so future workers will have a basis for evaluating this work's limitations themselves. It is expected that technological advancements will make the methods and instrumentation used here, look like primitive practices in need to be redone. As a matter of fact, the experimental work done 20 years ago on inflatable dams, is in need to be redone on the basis of technological advancements alone. It is not the purpose of this work to do this particular task, since there are no references of experimental dynamic response of inflatable dams, which is the goal of this work.

3.3.1 Internal Pressure Variations

The pressure transducers used are the miniature ENDEVCO(R) series 8510B. Characteristics of primary interest are listed in Table 3.1, taken from the specification sheet of the transducer. The values listed are considered to be correct without any verification. Especially the hysteresis characteristics are much more favorable than listed, because the frequency of interest is very low (1-30 Hz). These characteristics are especially important as they form the basis of the validity of the data. Because the signal variations are one to three orders of magnitude smaller than the signal average, the hysteresis characteristics are even better. As a result of these favorable characteristics, there is no reason for further dynamic calibration of the pressure transducers.

Table 3.1 Specifications of the pressure transducer EDEVCO 8510B

Characteristic:		
Sensitivity	150±50	mV/psi
Hysteresis (max)	1.5	%
non-linearity	1.0	%
non-repeatability	0.2	%
pressure hysteresis	0.2	%
Resonant frequency	70	kHz
Acceleration sensitivity	0.0002	psi/g
Thermal transient resp.	0.003	psi/°F
Noise, dc to 50 kHz	5-50	μV

Signal noise after amplification is below 5mV under controlled laboratory conditions. However, the same noise reaches levels up to 20mV in some instances in the water channel area, according to the machinery in operation at the time, inside the building. Therefore, weak signals (during low vibration levels) are susceptible to this noise and further digital signal processing (DSP) is necessary.

DSP at IC level inside the Hewlett Packard analyzer provides excellent results. Even for some cases where the instrumentation "clamps" at the supply voltages going through self-oscillations, the analyzer is able to provide a clean signal output. A similar process is followed through numerical post-process analysis of the results. The FFT routines themselves are by nature filters of frequencies above the Nyquist frequency. In addition to that, the acquired data are processed through low-pass digital filters. The result is a clean output as the one shown in Figure 3.1 (solid line), in comparison with the actual data (dotted line). It is the conclusion from all the cases analyzed, that there is only a marginal difference between the power spectrum analyses of raw and filtered data.

The power spectra produced are further semi-automated processed for identification of frequency components at a resolution of 0.001Hz. However, it is possible to verify the results with

the HP signal analyzer at a resolution of only 0.01Hz, and therefore this value is considered the applicable accuracy level. The exact level of internal pressure variations is not of primary concern in this work, and therefore any errors related to calibration of the instrumentation or even slight non-linearity of the transducers is irrelevant.

3.3.2 Dynamic Displacements

Displacement measurements based on the infra-red optoelectronic circuit are analog RMS values. The signal has a maximum 5mV noise at instrumentation-lab control conditions. Different signal amplifications are possible, and the one used offered 1.7 volts/inch. Considering the noise level, this results in a typical resolution of 0.0085 of an inch. During vibration tests, however, the actual resolution approaches an infinitesimal value that is limited by the data acquisition process.

The Hall-effect 3D displacement sensor is very sensitive to a complicated calibration process. In addition, the use of non-temperature compensated Hall effect elements generated a temperature-dependent calibration. Moreover, the low-cost permanent magnets used showed susceptibility to moisture by showing a high corrosion rate. These, as well as other difficulties found in the supporting mechanisms inside the models, made the error evaluation of this sensor a formidable task.

3.3.3 Average Velocity

Errors involved here are related to the actual volume of water in the container, the timer switch ON/OFF factor, the point-gage reading, the cross sectional area measurement, and the existence of small surface ripples. The timer factor is considered very small in lieu of an error identification method (for this particular problem). This assumption is acceptable since the ON/OFF human error may be overly estimated to be one second, which represents less than a 0.3% error for the least volume of water measured during the tests.

Volume measurement errors involve the capacity of the receiving container, and the actual volume of water in the container at the end of the timing period. Two separate methods of correct water level are used. One is based purely on optical observations, and the other on a combination of optical and acoustical observations. This is possible due to the particular shape of the receiving container (Figure 3.9).

At the first level (capacity 90 liters) the correct level is identified only by sight. However, at the second level (capacity of 124 liters) the outlet pipe sound-level diminishes as the water level

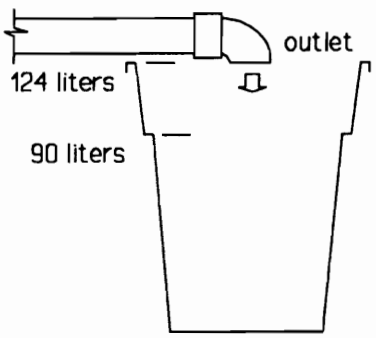

Figure 3.9 Setup of pipe outlet and receiving container.

reaches the outlet, until the sound is completely eliminated. At this point the water level has reached the right point. It is estimated that the error due to the turbulent nature of the water plane in the container is no more than 3 liters. This represents errors of 3% and 2% for the 90 liter and 124 liter capacities, respectively.

The flow rate process was shown to be very successful, as repetitive measurements showed in some cases a timing error of less than 1%, sometimes approaching to zero. Because of this accuracy, any data logs with a variation greater than one standard deviation were specified in the analysis algorithm to be dropped out. Figure 3.10 best describes the differences between the two methods. It is obvious that the second method (right graph) shows a reduction of the error about the mean at lower flow rates, something that was expected. The first method (left graph) appears to have the same levels of errors through the flow-rate range. This is probably due to the fact that at that level of the container the water plane was always highly turbulent regardless of the flow rate.

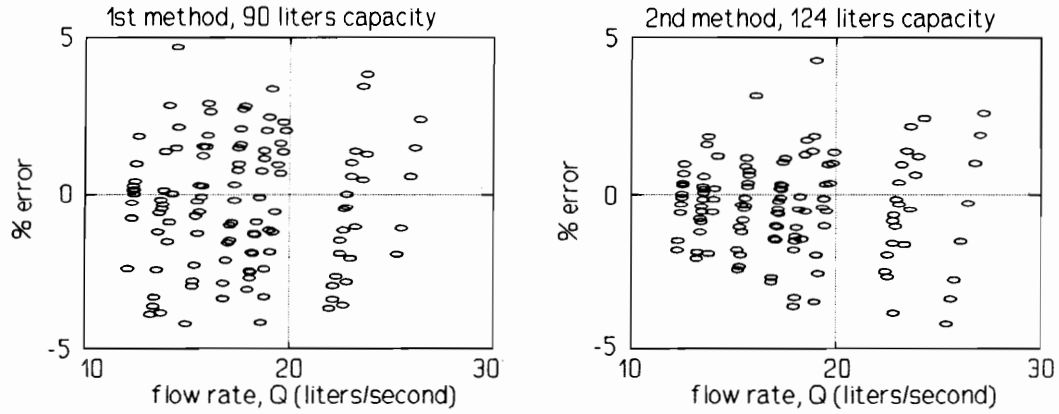

Figure 3.10 Flow-rate error distribution (about the mean) for the first method (optical) with a capacity of 90 liters, and the second method (opto-acoustical) with a capacity of 124 liters. [C151-233]

Average velocity error is further amplified with the error induced by the cross sectional measurements. As mentioned before, these measurements have a very good accuracy. Although the point gage and CCD camera setup can actually give a resolution of better than 0.0063mm (0.00025 inch), experiments showed that for a few cases this is reduced to 0.13mm (0.005 inch),

due to the surface waves. This results in an (overestimated) error of 0.15%, which is nevertheless considered marginal with respect to the error resulting from the flow rate measurements. Parenthetically, it must be clarified that the small surface waves mentioned are not a result of the dam's vibrations. Instead, these are waves propagated from the pipe outlet (Chapter Two).

Statistical analysis of several hundreds of cases may be required to provide a better accuracy than that shown in Figure 3.10, which are not available. Therefore the average velocity measurements will be considered that include an error not exceeding 5%, which is an acceptable value. In most of the cases, however, it must be emphasized that the error is well overestimated, but since it is under an acceptable level it will only be considered as conservative.

Chapter Four

FREE VIBRATIONS

The previous chapters dealt with the requirements for obtaining the response of inflatable dam models. This chapter deals with the models' response in terms of internal pressure variations. Models are tested free of loading and at different impounding water levels. Instead of treating impounding water loads as a distributed loading on a structure, the dam and the load are considered to be a system. The response of this system is governed by variables such as the internal pressure and the upstream water head.

4.1 Pressure Variations

Other civil engineering structures' response is usually measured in terms of displacement, velocity, or acceleration. These responses are dependent on the location and direction of the excitation, as well as the location and the sensitivity direction of the response sensor. Inflatable dams depart from these restrictions. In a sense the internal pressure variations tend to be the same regardless of the location of the excitation. This is due to the fact that any pressure excitation always acts perpendicular to the membrane and it always travels longitudinally (with respect to the dam). Therefore, the pressure response is sensitive to all types of loads, excitation direction, and excitation point. As a result, the natural frequencies of the system may be identified from a single point excitation.

In this respect, inflatable dams could be the "dream model" of experimental dynamicists. The traditional methods in civil engineering and mechanical engineering vibration testing, require

a cumbersome procedure of testing enough degrees of freedom (and the correct ones) to make sure that the natural frequencies of interest are detected. Parenthetically, it should be mentioned that other advanced methods, made available in the last few years, can acquire the structure's response from hundreds of points simultaneously.

4.2 Response without Hydrostatic Loading

During these free vibration tests, the models are fixed in the same conditions that occur when they are tested under water overflow. This way it is assured that details such as clamping position and membrane size are exactly the same as for the cases of impounding water or overflow. Technicalities such as these may seem to be trivial, but at such small model scale as the one used in this work, such details could make quite a difference.

There are thirty-six test cases on response measurements addressing these loading conditions. Parameter variations are based on the internal pressure of the dam. Each case has one measurement at each end of the dam. These two measurements are identified with the position of their pressure transducers, at the left or the right side of the dam, and they are both considered as "system inputs". Their spectral densities are identified as Pxx and Pyy.

Without any impounding water and with air as the inflation media (instead of water) the system, or better the model dam, has literally no mass. Previous experience on lightweight models suggests that such structures need to be tested under continuously monitored loading. One reason for not using impact excitation, is because the signal output fades rapidly (Figure 4.1).

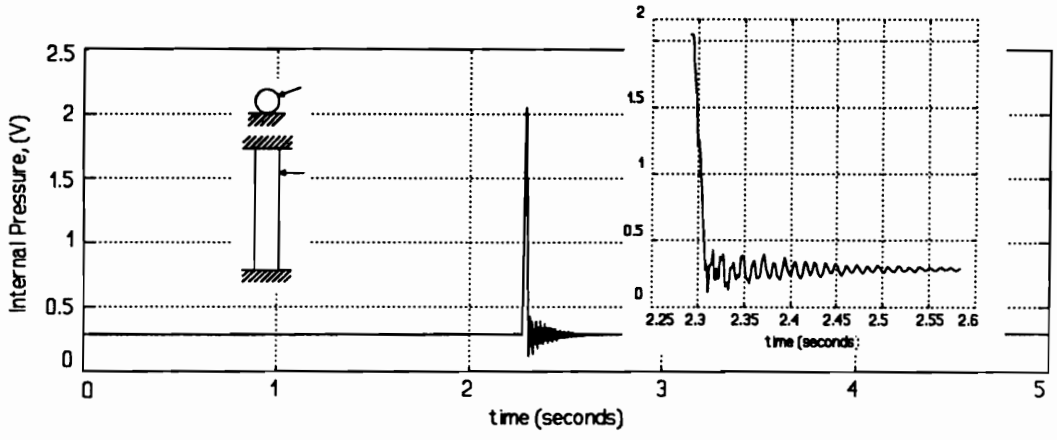

Figure 4.1 Typical response of model dams without impounding water, under impact excitation, P_i=12.75cm of water, L/H=27, H=6.7cm. [C325]

Usually, harmonic loading is used for being easy to generate as well as because it has been well studied. Such a load system would require an analog-controlled exciter with a force transducer attached on its receiving head. The excitation signal is fed into a signal analyzer as the input, and a measured response (in this case internal pressure variations) is the output. Frequency response functions and further analysis (commonly known as Modal Analysis [70]) to determine natural frequencies, damping ratios, and modes of vibration are the customary practice.

In lieu of such instruments the tests are restricted to power spectrum analysis of the response measured under impact excitation. Some measurements were done with an instrumented impact hammer which was specially developed for the inflatable dam models. Resulting frequency response functions (FRF) were used for comparison purposes with the frequency spectra.

The response shown in Figure 4.1, is typical of this experimental setup. The exploded view of the graph shows the highly damped characteristics of the dam. The impact excitation is applied approximately at $0.25L$, with an approximately 20° inclination from the horizontal. The location of excitation (or initial displacement) is not particularly relevant to the internal pressure response of the dam, as was determined by a number of trial tests.

4.2.1 Natural Frequencies

The structural response of the model dam is in a sense completely damped. Few oscillations are observed at a high internal pressure. At lower levels of internal pressure the response of the dam tends to be overdamped. Early during this work, it was identified that the internal pressure is by far the most significant parameter in the response of the inflatable dams. Internal pressure controls the stiffness as well as the damping characteristics of the system.

In these tests, there are no frequency components within the primary frequency-spectrum of interest (up to 30Hz). Auxiliary spectral analysis up to 100Hz reveals a weak frequency component between 80Hz and 90Hz. Anti-resonants before and after the resonant frequency are usually well formed. Further analysis up to 500Hz, showed that there are no other significant frequency components. Figure 4.2 shows a typical spectral density for both response signals, from the two pressure transducers at each end of the dam.

The sampling rate was originally set at 600Hz for a duration of 10 seconds, and later it was changed to 1200Hz for a duration of 5 seconds. The two sets of experiments were similar in nature, over the same static internal pressure variations. As expected, both data sets produced similar results. Figure 4.3 shows the relationship of the frequency components from spectral

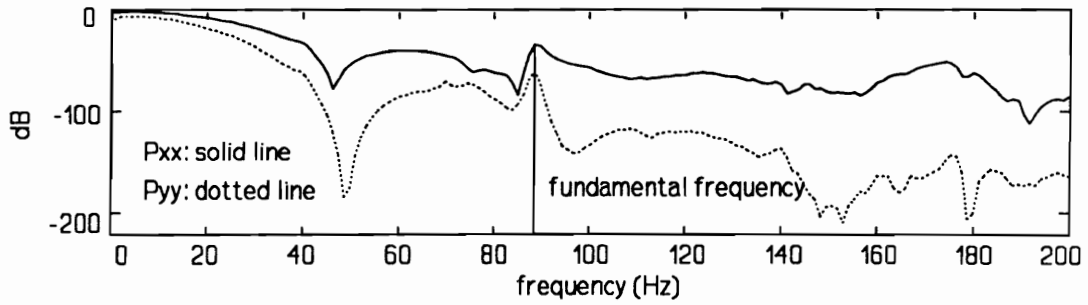

Figure 4.2 Spectral analysis for at test case with P_i=10.74cm. The spectral curves are shown with only a quarter of their original frequency resolution. [C326]

analysis, versus the internal pressure water-head.

There are three components displayed (in Figure 4.3) where the one is between 40 and 50Hz, exactly half the value of the component shown varying from 80 to 90 Hz. However, the power level of this component is very low and it disappears after a relatively high internal pressure head. On the other hand, the second component has the highest power levels throughout the pressure head variation, and a harmonic component in the 170 to 180Hz range. Therefore, this frequency component (80-90Hz) is considered to be the fundamental frequency. The asterisks and the circles in Figure 4.3, do not have any significant meaning except that they identify the two groups of data acquired at different time periods.

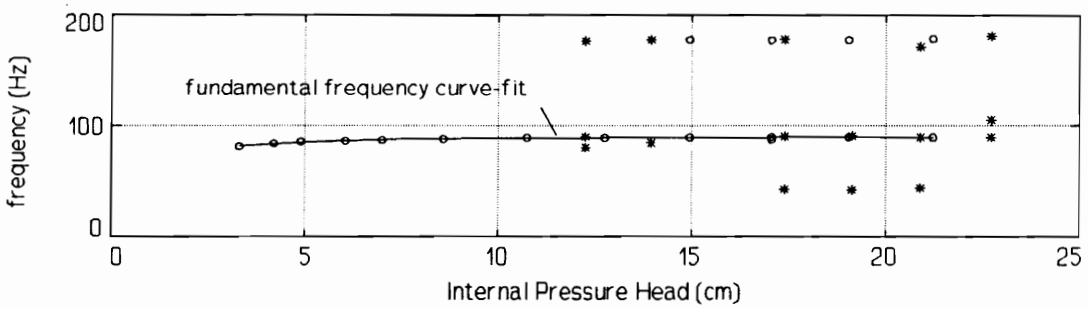

Figure 4.3 Primary frequency components of the free vibration cases without impounding water, H=6.7cm. The solid line is a polynomial curve-fit. [C255-260,C321-332]

This is in contradiction to the customary definition which uses the lowest spectrum peak frequency as the fundamental frequency. Instead, what appears here to be the fundamental frequency is probably a subharmonic frequency, an indication of non-linearities in the system. In this regard, the frequency components varying within the 170-180Hz region may as well be

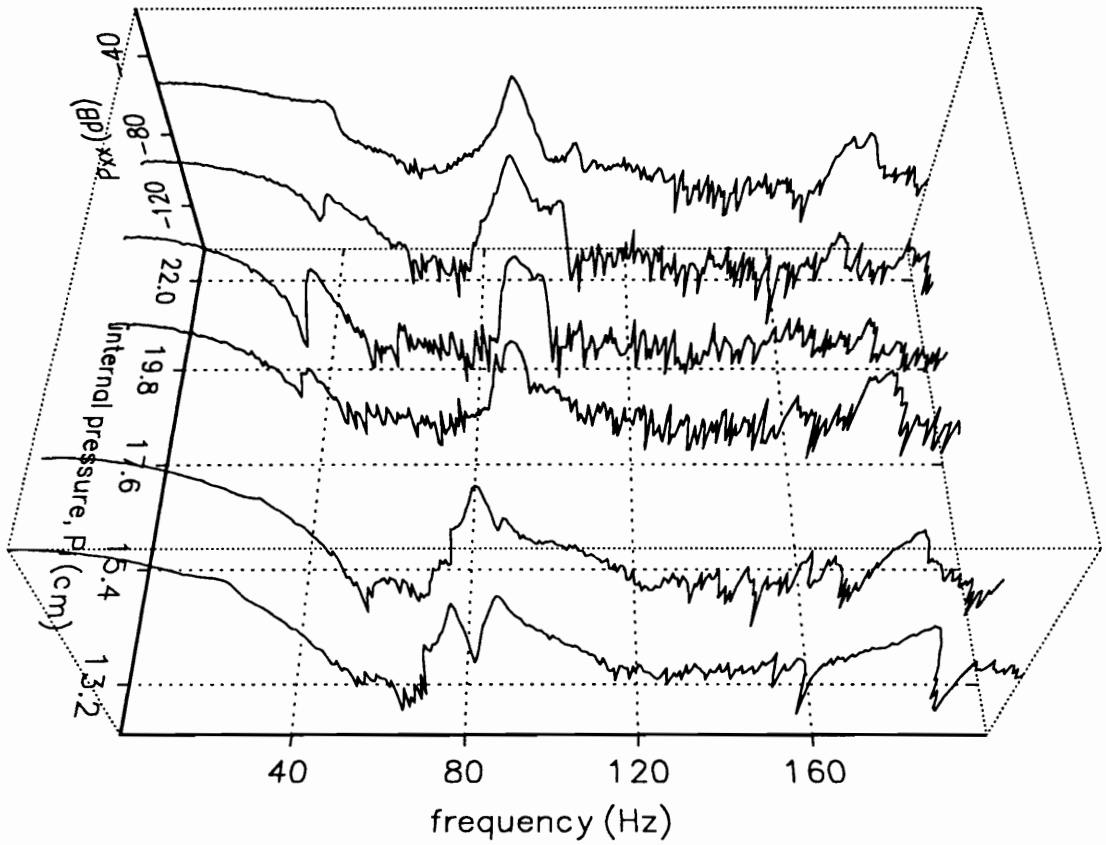

Figure 4.4 Power spectra of the cases who appear as asterisks in Figure 4.3. The noise shown in the spectra resulted from low sampling frequency (F_s=600Hz). [C255-260]

considered as superharmonics, rather than natural frequencies. Figure 4.4 puts in perspective the power relation of these subharmonic and superharmonic frequencies mentioned. It is evident that there are probably other frequencies as well, like the one shown in the front spectra (P_i=12.3cm). The resolution of the graphs in Figure 4.4 is reduced to one point every four data points for practical reasons related to word-processing.

At the scale of Figure 4.3 the fitted data appear to be linearly related. However, expanding the area of interest as shown in Figure 4.5, it is clear that the pressure-frequency relationship is non-linear. In fact the actual result from the regression analysis produced a fourth order polynomial,

$$\omega_d(p) = c_4p^4 + c_3p^3 + c_2p^2 + c_1p + c_0 \qquad \text{for} \quad 3<p<20\,\text{cm}$$
$$c = \{c_0, c_1, \ldots\} = \{69.121, 5.3560, 0.55949, 0.026264, 0.00045765\} \tag{4.1}$$

where ω_d is the damped frequency of the system, along the same lines as the single degree of

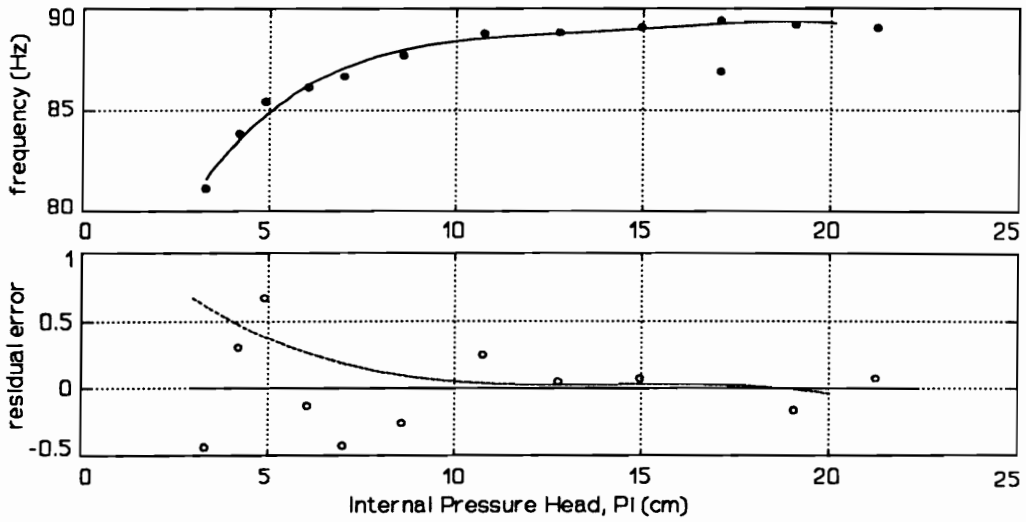

Figure 4.5 *Above:* expanded view of the fundamental frequency shown in Figure 4.3. *Below:* residual error of the fit function (circles), and its slope (dashed line).

freedom system damped frequency is defined (next section). The data appear to form an asymptotic line close to 90Hz. The polynomial derived, however, does not behave like that outside the range specified, and therefore its usefulness is restricted. Other trial functions produced the required asymptotic line but they were deficient in the internal pressure region of interest, 3 to 25cm of water head.

Unlike the overflow cases, here the non-dimensional parameters are not as clearly defined. For example, the frequency data in Figure 4.5 appear to fit an asymptotic function which has an upper limit around 90Hz. This upper limit could have been used to non-dimensionalize the frequency components. However, this would have no practical meaning in the overflow vibrations. As mentioned earlier, the frequency range of interest is up to 30Hz, mainly because there is no significant response after this limit. This is equally true for cases with impounding water as well as for overflow cases. Therefore, it will be unrealistic to non-dimensionalize based on these particular tests here.

It should be mentioned, however, that the same frequency component (deviating around 90Hz) does exist in all loading cases (impounding water and overflow). The power level of this frequency component is usually 20 to 30 orders of magnitude less than the primary component, but yet clear and well shaped. An ensemble of frequency spectra is shown in Figure 4.6, where the "empty" region up to 30Hz and the distinct anti-resonances are very clearly displayed.

Similarly with the frequency data, internal pressure can not be non-dimensionalized with a meaningful parameter as well (in this set of experiments). Many make-up parameters are available, e.g., the pressure required to bring the membrane material to its yield point, the maximum possible upstream head, etc. However, they offer only minimum information about the dynamic state of the dam, either in free or overflow vibrations, as is the case for the frequency values. It will be shown later on, that the cases including hydrostatic or hydrodynamic loads are dissimilar systems to the cases presented here. This is one more reason that the internal pressure head, P_i, was not non-dimensionalized.

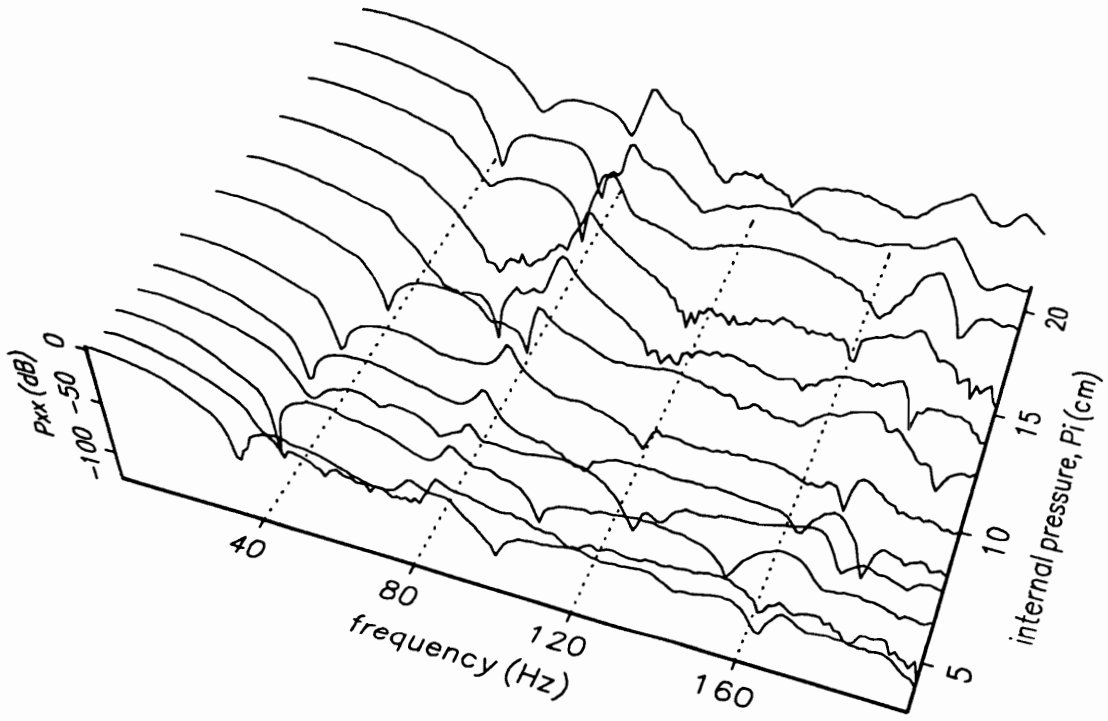

Figure 4.6 View of the frequency spectra ensemble versus the average internal pressure, (h_u=0) for the cases that appear as circles in Figure 4.3. [C321-332]

4.2.2 Single Degree of Freedom Approximation

The response of the model is measured in terms of its internal pressure variations. It was mentioned earlier that, since the models are made with a membrane-like material any load or deformation applied on the membrane always translates to pressure variations. Therefore, if the pressure response shows only one dominant frequency component, then the whole dam may be approximated with a single degree of freedom system. The advantage of using the internal

pressure variations as the system's response is that, the same formulation is valid for both longitudinal and transverse oscillations.

The assumption is made that the pressure variation $p(t)$ is governed by a linear equation of motion. Therefore, a single degree of freedom oscillator with viscous damping can be based on equation (2.8), which can be written as

$$(m+m_w)\ddot{p} + (c+c_w)\dot{p} + (k+k_w)p = 0$$

$$\text{for} \quad m_s = (m+m_w), \quad c_s = (m+m_w), \quad k_s = (k+k_w) \tag{4.2}$$

$$\therefore \quad m_s\ddot{p} + k_s\dot{p} + k_s p = 0$$

where p is the internal pressure variation around the mean internal pressure Pi. Following the usual steps for solving this equation of motion, for $p=Ce^{qt}$, the characteristic equation and its solution are,

$$m_s q^2 + c_s q + k_s = 0 \qquad \therefore \qquad q_{1,2} = -\frac{c_s}{2m_s} \pm \sqrt{\left(\frac{c_s}{2m_s}\right)^2 - \frac{k_s}{m_s}} \tag{4.3}$$

The relationship of the coefficients in the square root determines the nature of the system. For an underdamped system, which is the case here, the roots of the characteristic equation are complex conjugates.

Substituting into the general solution of the equation of motion, equation (4.2), and with the use of exponential relations (Euler's equations), the general solution is well known to have the form

$$p(t) = e^{-(c_s/m_s)t}(A\cos\omega_d t + B\sin\omega_d t) \tag{4.4}$$

or better,

$$p(t) = Ce^{-\xi\omega t + i\omega_d t} \tag{4.5}$$

where A and B are constants of integration, ω_d is the damped frequency of the system and ξ is the damping ratio (c_s/c_{cr}, where $c_{cr}=2m\omega=2k/\omega$). For clarity reasons the system's mass m_s, damping c_s, and stiffness k_s, will be simply referred to as m, c, and k respectively. Through trigonometric

$$p(t) = Ce^{-\xi\omega t}\cos(\omega_d - \alpha) \tag{4.6}$$

manipulations, the solution takes another well known form, with a periodic cosine part and a decaying exponential part, equation (4.6). This form of the solution is particularly useful as will

be shown in the following section. The phase difference, α, need not to be defined as the periodic part of the equation is of no interest at this point.

4.2.3 Damping Characteristics

Figure 4.1 clearly shows that the response of the models without any impounding water is highly damped. Nevertheless, the damping coefficient of an SDOF system can be identified experimentally by initiating free vibration oscillations, in the same manner as done here. At the impact excitation moment, the initial internal pressure peak may be considered as the initial pressure condition p_o.

The method used to determine the damping ratio ξ, is commonly known as the logarithmic decrement method [71]. For the SDOF system described in equation (4.5), the real part of the solution defines the envelope of the oscillatory part of the solution. At a unity cosine factor then equation (4.6) reduces to the exponential function,

$$p(t) = Ce^{-\xi\omega t} \tag{4.7}$$

Assuming that using the peaks of the solution for the tangential points to the decaying exponential envelope, does not introduce a large error, then the logarithmic decrement δ between two successive peaks can define the damping ratio ξ, as given in equation (4.8):

$$\delta = \ln\left(\frac{p(t_1)}{p(t_2)}\right) = \xi\omega T_d \qquad \therefore \qquad \delta = \frac{2\pi\xi}{\sqrt{(1-\xi^2)}} \tag{4.8}$$

where T_d is the damped period, measured from consecutive response peaks.

Alternatively the damping ratio may be derived by curve-fitting the peak points of $p(t)$. From equation (4.7) it follows that

$$\ln(p) = \ln(C) - \xi\omega t \tag{4.9}$$

The coefficient $-\xi\omega$ can be found by fitting the linear relationship in equation (4.9). If now this coefficient is designated as C_f ($C_f = -\omega\xi$), and with the damping coefficient relationship between damped and non-damped natural frequencies, $\omega_d = \omega(1-\xi^2)^{1/2}$, a relationship for the damping ratio is derived:

$$\xi^2 = \frac{C_f^2}{C_f^2 + \omega_d^2} \qquad \therefore \qquad \xi = -\frac{C_f}{\sqrt{C_f^2 + \omega_d^2}} \qquad \text{for} \quad \xi > 0. \tag{4.10}$$

It takes longer to reach a conclusive result with this equation; however, the result is much more

accurate since it considers several points from the time history. Moreover, it uses the damped frequency from the spectral analysis, rather than the time difference between two successive peaks. Nevertheless, in the computer analysis programming both methods are employed for comparison purposes, but only the outcome of equation (4.10) is presented. It should be emphasized again that the formulation is based on the linear single degree of freedom mathematical model, and therefore deviations from this formulation should be expected.

As shown in Figure 4.7 not all the responses can be modeled with such a simple approximation. As a matter of fact, in this set of experiments only case #324 has a remote resemblance to a single degree of freedom system. The curves show only the normalized (to unity) amplitudes not exceeding 0.3 for clarity reasons. In a full range plot all time responses have a similar form to the one in Figure 4.1.

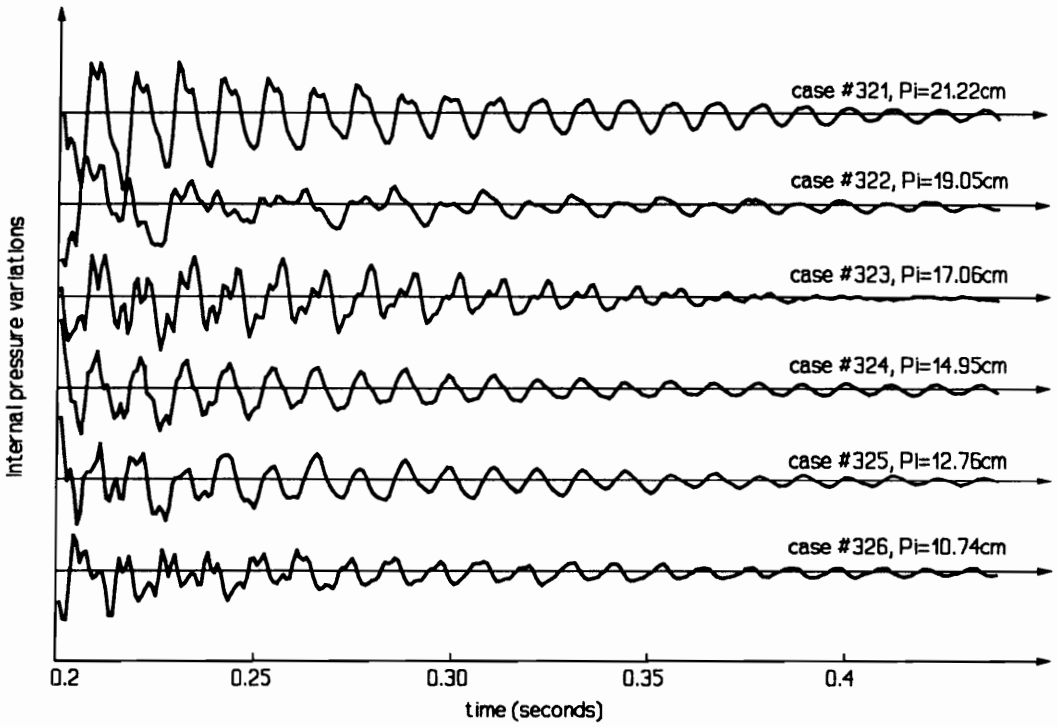

Figure 4.7 Expanded time logs of free vibrations from impact excitations, without hydrostatic loading. The peak amplitude (normalized to unity), occurs 0.0125 seconds before the first point shown.

Curve-fit analysis based on the least squares method shows that the results here cannot be sufficiently approximated by an SDOF system. The damping ratio, ξ, is found to be between 0.043 and 0.22 as shown in Figure 4.8 upper and lower graphs, respectively. The first ratio is very

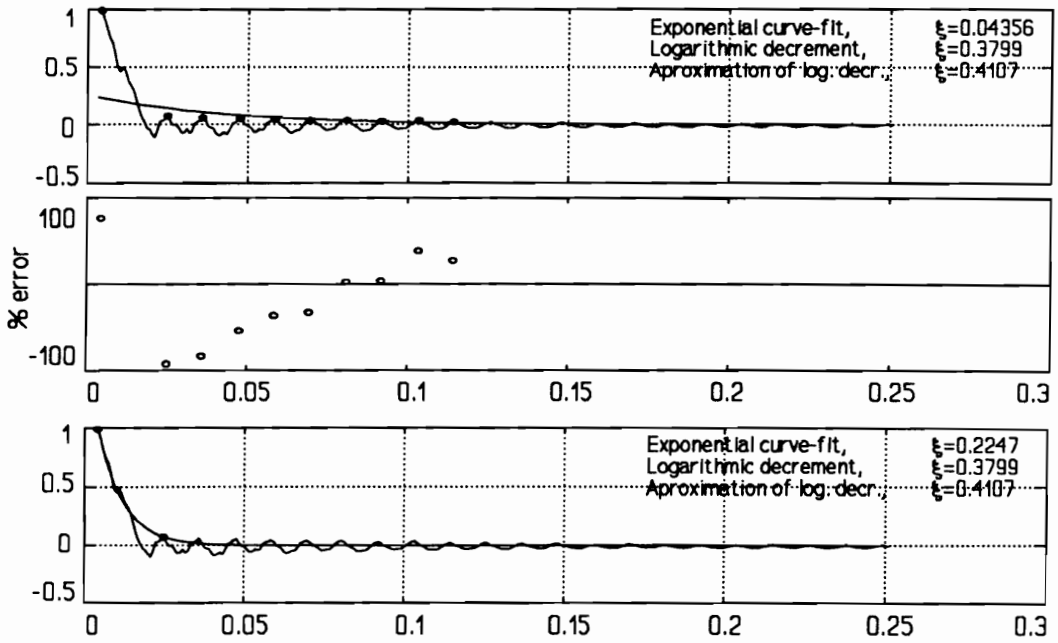

Figure 4.8 Exponential curve-fit, on the normalized time response at P_i=14.95cm. *Upper:* Nine-point fit. *Middle:* Residual error of 9-point fit. *Lower:* Two-point fit. [C234]

low to be considered correct, while the second ratio suggests a reasonably damped system which it may be the case here. However, neither curve-fit analysis is even close to the real data and therefore any approximation to the real damping ratio may just be coincidental. The other two methods are based on the SDOF approximation again and there are questions about their validity, since they only consider the decrement of the first two peaks.

Concluding, the results of the linear single oscillator approximation are far away from the reality. However, the conclusion can not be propagated to all other loading cases of inflatable cylindrical membranes. As will be shown later, the dams behave completely differently under hydrostatic loading. This is in part due to the water mass contributed to the system.

4.3 Response under Hydrostatic Loading

Test cases are considered with an upstream water height h_u. This impounding water is treated as part of the inflatable dam system, as mentioned earlier in the introductory comments. Impact excitation is used to perturb the dam and record its internal pressure variations. Again, two pressure transducers are located at each end of the model. This dual setup is necessary to verify each other's measurements, and also to detect any pressure wave variations at the dam's ends.

Any effects from secondary vibration due to water surface ripples are extremely confined or non-existent. This is primarily due to the fifteen foot long upstream space available for the waves to disperse before they get reflected back. Based on the instrumentation used for the dam's response measurements, the final effect of the ripples was too small to be detected.

This section represents 120 response measurements from 60 cases. There are two sets of experiments acquired at different time periods, and this is where the significance of distinguishing the two case sets stops. All cases deal with the internal pressure variations from the two ends of the model, L/H=27. The two responses are identified as previously, X and Y, and their power spectra are identified by Pxx and Pyy, respectively.

4.3.1 Natural Frequencies

The natural frequencies are obtained through spectral analysis on the pressure variation response of the dam to impact excitation. Data acquisition sampling rate is set at 600 samples per second for a duration of ten seconds. The acquired data are post-processed to achieve a spectral resolution of 0.001Hz, based on curve smoothing techniques. For most of the cases (combinations of internal pressure and upstream water depth), there is no other significant frequency component but the primary frequency which is within the 10-20Hz range. At low internal pressures additional frequencies appear to gain in their energy levels. A frequency component of negligible energy level around 90Hz is always present, as was mentioned in the previous section.

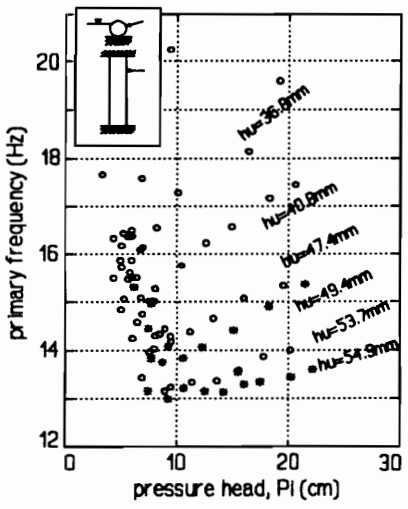

Figure 4.9 Internal pressure water-head (cm) versus the primary oscillation frequency, for various upstream heads. [C261-278, C279-320]

The internal pressure head, P_i (cm), of inflatable dams is a very significant variable as shown in Figure 4.9. Of equal importance is the impounding water level, or else, upstream water-head, h_u (mm). These are noted along the line notions made from the data points generated for each specific upstream head.

Figure 4.9 is generated by including only the peaks of the power spectra, for a series of different internal pressures and upstream water depths. If all the points from the power spectra would have been included, then these would have been placed vertically based on their upstream

water depth. The graph does not identify the energy level for each frequency component shown. This can only effectively be presented for all the variable combinations shown, by using color coded symbols. The star (*) and circle (o) symbols are used to signify the two sets of experiments that took place at different time periods.

Frequency components decrease with a decrement of internal pressure, or an increment of impounding water. It is also apparent that the rate of frequency decrement with respect to internal pressure, decreases with an increment of the depth of the impounding water. Therefore the significance of the internal pressure decreases with an increasing upstream water-head. The internal pressure factor never diminishes at higher upstream water levels, but it certainly does not show the tremendous frequency shift shown at h_u=40.8mm (or even at h_u=36.8mm). This statement is made clearer during the discussion of overflow vibrations in the next chapter.

The height of the dam for these tests, H, is 6.7cm, and the aspect ratio is 27. It is already clear that the results must be presented in non-dimensional parameters, in a way that critical variables and sizes are taken into account. These variables are identified to be the internal pressure, the upstream water depth, and the height of the dam. Additional variables are likely for different loading cases.

For the internal pressure variable, the non-dimensional *pressure ratio* P_i/h_u is considered here, where P_i is the internal pressure water-head as defined by

$$P_i \triangleq \frac{p_i}{\rho g} \tag{4.11}$$

where p_i is the internal pressure of the dam (in force per unit area format), g is the acceleration of gravity and ρ is the water density constant. This non-dimensional parameter is an important factor in the dynamic state of the dam, for both impounding water and overflow cases. It relates the retaining strength of the dam (function of internal pressure) with the applied load (hydrostatic upstream head).

An additional parameter is also introduced, the *load ratio* h_u/H, where H is the height of the dam. Load ratio does not represent the ratio of any real loads but instead, it is a measure of the hydrostatic load on the dam with respect to the load capacity of the dam. This load capacity of the dam is defined by many parameters, the most important of which is its height, H. The height of the dam identifies the maximum hydrostatic water head physically possible, since over that height there will be overflow and the load is no longer considered simply hydrostatic.

Based on the two non-dimensional parameters just defined, it is possible to have a clear

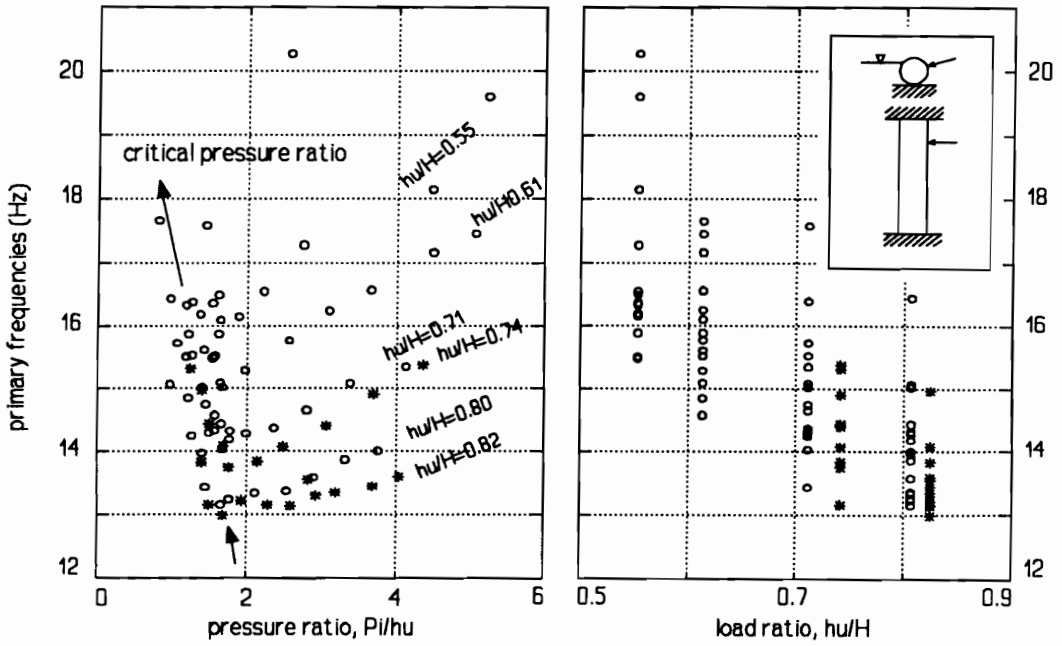

Figure 4.10 Primary frequency components of free vibration with impounding water, under impact excitation as shown in the upper right sketch. [C261-278, C279-320]

view of the frequency response characteristics of these tests. It is shown that these two parameters can definitely control the response of inflatable dams. These are not the only controlling parameters, but they are by far the most important ones. The results shown in the graphs in Figure 4.10 are based on spectral analysis using a 90% overlap Hanning window method. The maxima of the power spectra are identified in a semi-automated process.

There is little difference between the frequency versus pressure ratio and frequency versus pressure head, as shown in Figure 4.9 and the left graph of Figure 4.10. The graphs include not only the primary frequency components, but also some significant secondary components. These secondary components become amplified at a certain internal pressure range, or better, pressure ratio range. This range appears to have an upper pressure ratio limit equal to 1.8 (Figure 4.10). This limit decreases for higher impounding water heads. The two arrows in the left graph of Figure 4.10, show the approximate location of this critical pressure ratio, with respect to a variable load ratio. By observing the two graphs (which have the same frequency-axis), it is apparent that a given frequency component has different values depending on both the load ratio and pressure ratio. This multivariable dependance of the frequency components is investigated. The term "multivariable" is used to indicate that is likely to have more than two significant parameters.

There are six sets of tests, corresponding to equal number of variations of the pressure ratio. These can be identified in the left graph of Figure 4.10 by their relatively linear declining path, similarly to Figure 4.9. Lower than the upper critical pressure ratio of 1.8 (identified earlier), the picture is not clear. After that point, however, the frequencies (at given load ratio) appear to have their origin from the same frequency component.

The right graph of Figure 4.10 shows the columns created by data points from pressure ratio variations for given load ratios. Since the two graphs share the same vertical axis, it is possible to identify which point from the right graph is the same as the left graph by drawing a horizontal line. It is concluded from the load ratio graph that for higher load ratios a critical frequency may be identified around 13Hz.

It is evident that the lower the internal pressure is, the lower the natural frequencies of the system become. This is in accordance with the expectations of a typical structure, when its stiffness is reduced. In addition, the system shows a reduction of its natural frequencies with increased impounding water (Figure 4.10, right hand side), as if the mass of the system is increased. In a sense the behavior of the water-structure system is reasonable.

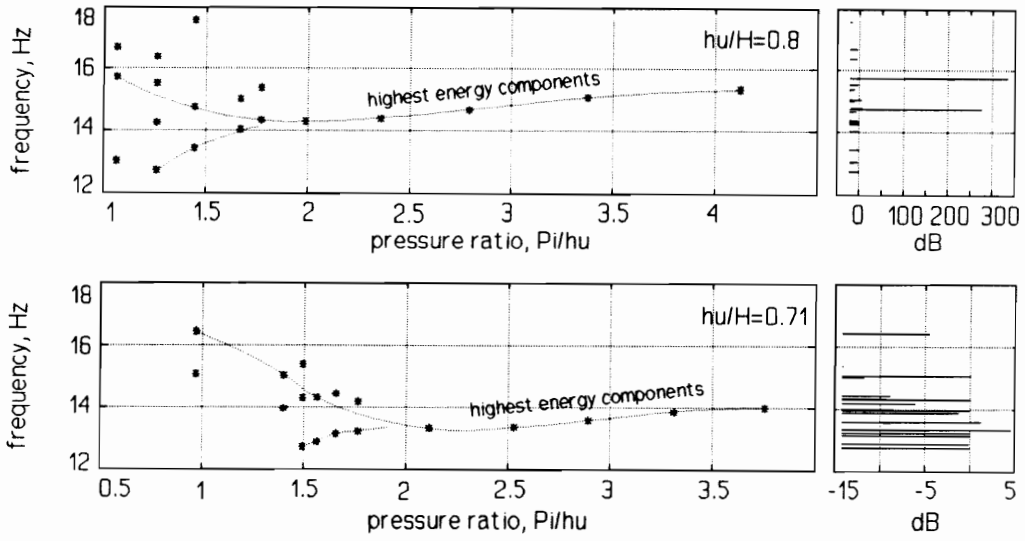

Figure 4.11 Natural frequencies versus pressure ratio distribution. The graphs at the right show the energy level for each frequency component present. [C279-289, C290-299]

There is the unusual phenomenon where the natural frequencies of the system increase with a decrease in the pressure ratio (or pressure head), as seen on the left graphs of Figure 4.11. Even more unusual, where this frequency ascent starts, another frequency path goes in the

opposite direction. Because the frequency components on the spectral plots have similar shapes (in this set of tests), it is not possible to identify which component is which.

Theorizing about the course of the phenomenon, there are two most likely events: a) There is one frequency component that later splits into two, similar to bifurcation; b) There are two frequency components, where the fundamental frequency follows a declining path all the way, and the other is initially dormant and becomes notable at a later stage with an inclining path. These points are made more clear with Figure 4.11, both upper and lower graphs. A "highest energy component" path is identified in the graphs. The path is defined by connecting high energy frequency components for consecutive spectra of pressure ratio variations.

Figure 4.11 also includes horizontal bar graphs (at the right) of the energy levels (power spectral density) for each point shown in the graph at the left. For each set of graphs, the left and the right plots have identical vertical axes. It is therefore possible to identify the frequency points of highest energy by drawing the horizontal line from the power level bar graph (right), to the frequency component graph (left). It is interesting to note the very high power levels of the two frequency components in the upper graphs. Again, this is probably the result of the added water-mass in the form of an increment on the load ratio (upstream water depth).

Although it first appeared that the principal vibration frequency drops with a drop in the pressure ratio, this is not the case as shown in Figure 4.11 and Figure 4.12. The latter graph is generated in linear units (rather than decibels), so that the highest energy peaks are apparent. It is therefore safe to claim that the frequency of oscillation with the highest energy, has a declining path with respect to the pressure ratio. At a critical pressure ratio (function of the load ratio), the frequency path ascends. This frequency path does not necessarily contain frequency values from the same mode of vibration. However, it is the frequency of largest amplitude oscillations for the given pressure ratio and load ratio combination. There is a difference here from lower load ratios, in the fact that both frequency components after the bifurcation have an increasing path.

Without any doubt there is a three-dimensional relationship between the natural frequency of oscillation, the pressure ratio, and the load ratio. The relationship is better clarified if the distinction of the same mode of vibration is made (if a same mode actually exists). Such a relationship can serve as a guideline to mathematical modeling.

Of practical use, however, is the relationship of the maximum-energy vibration frequencies versus the pressure and load ratio. This frequency may be the result of different modes of vibration, but it is the frequency of interest if the ultimate goal is to avoid high energy

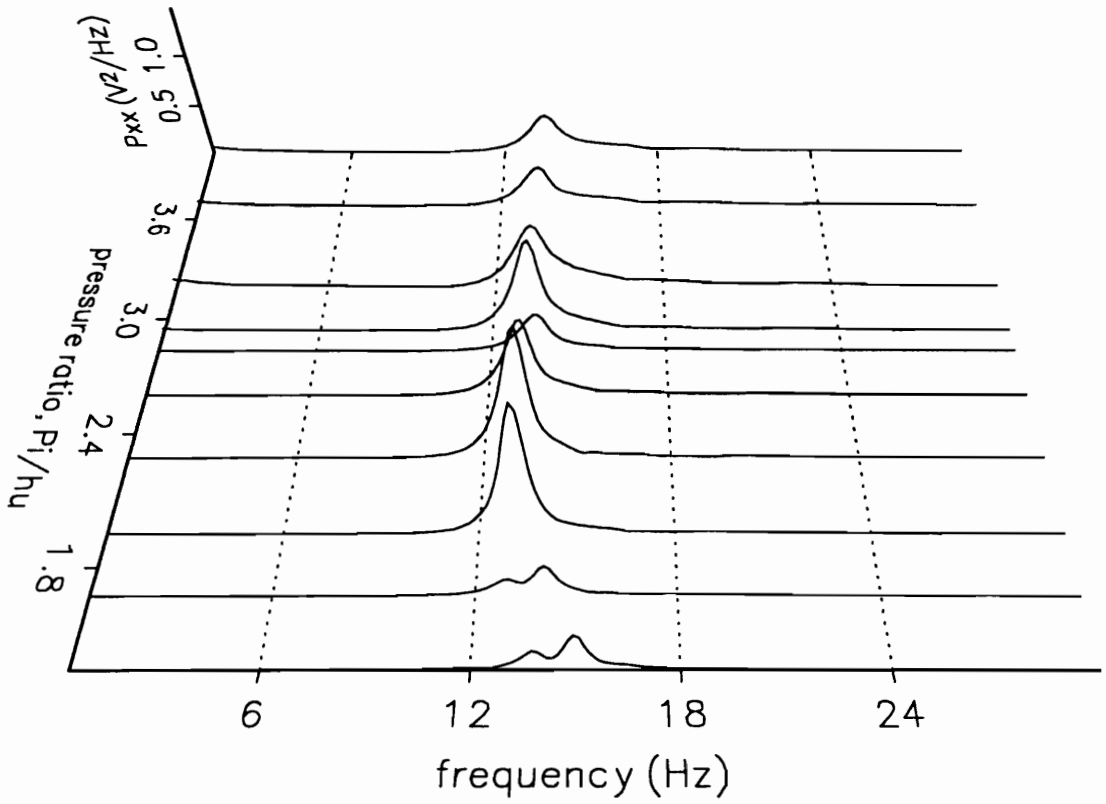

Figure 4.12 Frequency spectra waterfall graph for a load ratio of h_u/H=0.82 (H=6.7cm). Both frequency components after the bifurcation have an increasing path.

oscillations. Apparently, the lowest frequency of oscillation is not necessarily the fundamental frequency under the usual interpretation of this term.

Regression analysis of the data and parameters shown in Figure 4.10 produces a surface plot (left graph of Figure 4.13). The xy-plane is based on the pressure and load ratio variations, and the elevation of the surface plot gives the frequency values. The analysis is based on a fifth order two-dimensional polynomial function. The polynomial is generated based on the Pascal's triangle [72], and the computer algorithm involved alphanumeric programming.

A second analysis is also performed on the scattered data, based on two dimensional interpolation (right graph in Figure 4.13). This result is considered to be closer to the real data than the polynomial approximation. The reason lies in the fact that the interpolation starts from the given data and fills the empty spaces in between. Therefore, the resulting surface has the real scattered data as part of itself. Curve-fit, on the other hand, uses the actual data to approximate a best fit and it does not necessarily include them as part of its result. As a matter of fact, unless

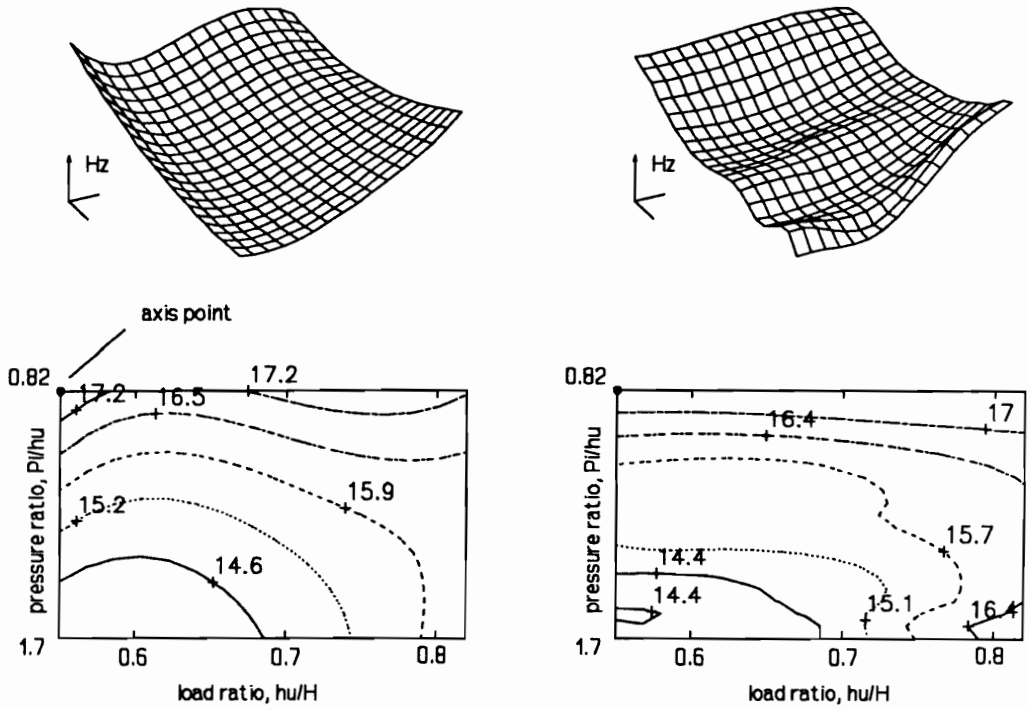

Figure 4.13 *Left:* Fifth-order polynomial approximation curve-fit. *Right:* Two-dimensional interpolation. The contour lines are equal-frequency levels. [C261-320]

the actual data can fit a polynomial function (or any function used other than a polynomial), there is always an error of fit.

The results of the two analyses are shown in Figure 4.13. They have comparable general features but they do not show adequate similarity, to claim the polynomial approximation a success. For example, the "hump" produced in the middle of the interpolation surface does not show on the polynomial surface. Moreover, the corners of the polynomial surface tend to have a higher level of error, characteristic of the polynomial curve-fit analysis.

Concluding, the frequency response of the models is indeed a function of the two non-dimensional parameters, the pressure ratio (P_i/h_u) and the load ratio (h_u/H). The relationship between this frequency of the highest energy level for a given set of these parameters, is quite nonlinear, and beyond any simplistic polynomial approximation.

These frequencies are part of the water impounding dam system, and they should be expected to appear during the overflow vibrations. The actual value of the frequency components remains a function of the pressure and load ratios.

4.3.2 Damping Characteristics

Unlike the cases without impounding water, here, the internal pressure time-response to impact excitation is much smoother. The instrumentation, the model, and the excitation method are identical to the cases with no hydrostatic loading. However, the model behaves completely differently in terms of its damping ratios. These are evaluated based on the same SDOF approximation presented earlier.

Three methods are used again, and for many of the cases they produce results with only marginal differences. The cases where the damping ratios have medium to large errors, are the cases of small load ratio, h_u/H, or the cases of very small pressure ratio, P_i/h_u. The former is a result of a reduction of the dynamic mass of the system, and the latter is the result of secondary oscillations that make the time response look like a decreasing amplitude modulated wave. These frequency characteristics were discussed in the previous section.

A typical time response ensemble is presented in the following graphs (Figure 4.14 and Figure 4.15). It is clear that the damping ratios are much lower than in the cases without impounding water. Moreover, it is evident that the response changes with respect to a reduction of the internal pressure, from a good approximation to a single degree of freedom to something other than an SDOF. During tests where the load ratio is very low, the pressure time response starts resembling the cases tested without impounding water.

The time response characteristics do change with respect to the pressure ratio. These changes are consistent with the findings in the previous section (on frequency characteristics). As a matter of fact, the reason for this behavior can only be explained by observing the spectral analyses shown in Figure 4.12. It is seen that at lower pressure ratio there are two significant frequency components. This particular pressure ratio is identified earlier as the critical pressure ratio where the frequency path (shown in Figure 4.11) separates into two paths. It therefore evident that the time responses shown in Figure 4.14 are in fact a direct result of this frequency path separation into two main frequency components.

Damping characteristics derived from an SDOF approximation, are good only for the cases in which they do not show a two degrees of freedom response. In fact, the cases that appear to be a single degree of freedom response have a very good approximation, reaching a 99.9 percent agreement in the evaluation of the damping ratio, based on three methods.

These methods are the logarithmic decrement method noted in a previous section, the exponential curve-fit method, and an approximation to the logarithmic decrement method. This

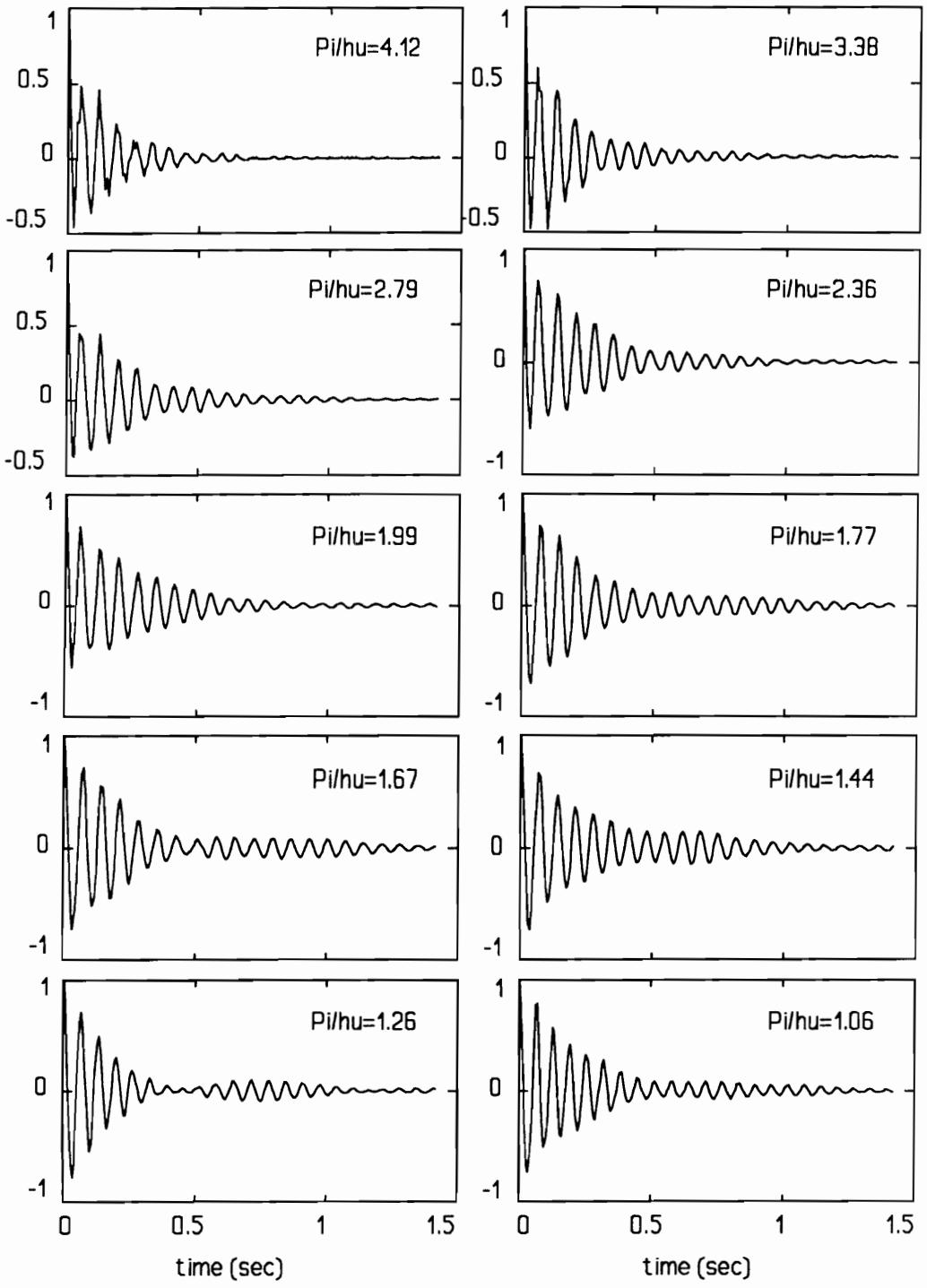

Figure 4.14 Response from impact excitation, at a load ratio h_u/H=0.71 (only a quarter of the original data resolution is displayed). The data are normalized to unity. [C290-299]

approximation is based on the assumption that the damping ratio is less than 0.2 and therefore the error does not exceed two percent.

Cases clearly showing a multi-DOF response were still analyzed with the same methods but the errors are much larger. In order to minimize this error the curve-fit method uses only the first three or four response amplitude peaks. This does not warrant correct results, but judging from the time response characteristics the error should not be large. An alternative to the SDOF approximation is of course to use two equations of motion. It is required, however, to uncouple the damping forces from the equations of motion by making certain assumptions in order to satisfy the conditions. Nevertheless, the resulting equations may offer a much better approximation than the SDOF approximation offered here.

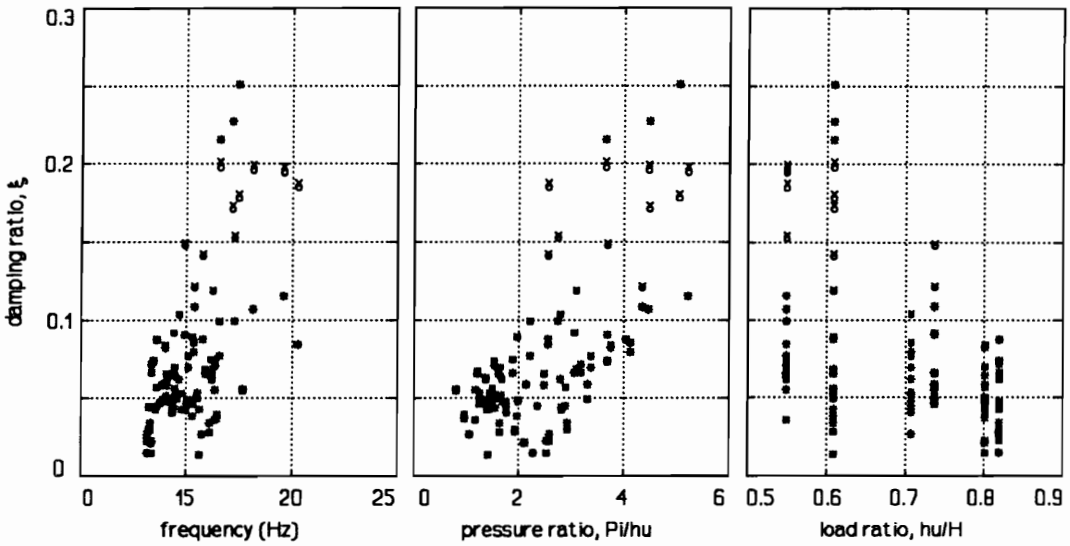

Figure 4.15 Damping ratio (ξ) distributions with respect to highest energy frequency components (left), pressure ratio (middle), and load ratio (right). [C261-320]

Cumulative damping ratio scattered point graphs are shown in Figure 4.16. There is no distinction made between the cases which are noted to be better SDOF approximations. The error between the three methods (mentioned earlier) is negligible for load ratios higher than 0.65, (h_u/H>0.65). The exponential curve-fit method is identified by asterisks, logarithmic decrement by circles, and its approximation with "x" marks. In most of the cases the three methods have a good agreement, and it is not possible to distinguish between the different symbols used.

The damping ratios show a general reduction with respect to an increasing load ratio. Damping ratios of less than ten percent are noted for a load ratio higher than 0.8. The majority

of the damping ratios are in fact lower that 10 percent, regardless of which parameter is considered (frequency, pressure ratio, or load ratio). There are not enough reliably-generated data to warrant a particular pattern of distribution for the damping ratio with respect to any of the three parameters. Therefore, the damping ratio will be considered to have a value between 0.01 and 0.1.

4.4 Water-Filled Dams

Pilot tests on water-filled dams were performed only for comparison purposes. It was shown that the oscillation amplitude was one to two orders of magnitude greater than for the water-inflated dams. The situation was more intensive under continuous excitation. Power spectral energy was also much higher and the spectral graphs had much less noise. The effect of impounding water was minimal compared with the air-inflated dams.

4.5 Comparison with Previous Work

There is no experimental work published on the dynamic response of inflatable dams without overflow. Most of the theoretical work, however, presents the response of the dams for impounding water or free of loading conditions. Unfortunately, the theoretical work done is for double anchored inflatable dams, and there are reasonable questions about the validity of a comparison with a single anchored system. Nevertheless, an attempt to establish a relationship is presented here. The static considerations of the problem are not of any interest here, as they were investigated extensively in both analytical and experimental terms by other workers.

4.5.1 Scale-Up of the Experimental Results

It was mentioned in previous chapters that the results of the experimental work here have to be scaled-up. This must be done before any comparisons are attempted since the relationship between the scaled models and prototypes is not linear. This may be easily shown from the relationships established earlier in Chapter Two, and from Table 2.1.

Only the external sizes are used, length (L) and height (H), to scale-up the results. The basic assumption of the modelling practice was that prototype material largely responds as an inextensible membrane. This holds true for the materials used in the early days of inflatable dams and for most of the dams installed today (the Sumigates). The Rubber Dams from Bridgestone have a considerable thickness and therefore they may not be represented adequately as membranes.

However, considering the additional number of parameters to be taken into consideration for material modelling, it was decided that only membrane-like dams would be studied. As a result, only dams that can be modelled as membranes are to be compared with these results. Therefore, the actual thickness and the tensile strength of the material are not of scaling concern (in this work). More information on the material used for modelling is provided in Chapter Two.

Only the scale ratio is required to scale-up any geometric quantity. The scale ratio for the model with an approximate aspect ratio L/H=27 is actually a range of scale ratios based on the prototype dams already in use, as explained in Chapter Two. The lower limit is close to 8 and the upper limit is close to 35. These numbers are derived by combining the height and length scaling processes. If the aspect ratio is considered to be irrelevant after a critical value, then the scale ratio range is further expanded, with an upper value of 45 to 50. For the current results, however, only the given aspect ratio limits will be considered, namely 8 and 35. Using these values, the length of prototype inflatable dams, L_p, is between certain minimum and maximum values as derived below,

$$\begin{aligned} (L_p)_{\min} &= L_m (L_r)_{\min} = 1.791\text{m} \times 8 = 14.3\text{m} \ (46.9 \text{ feet}) \\ (L_p)_{\max} &= L_m (L_r)_{\max} = 1.791\text{m} \times 35 = 62.7\text{m} \ (205.6 \text{ feet}) \end{aligned} \tag{4.12}$$

Similarly, the height of prototype dams (H_p) varies based on the same linear calculations (and the same scale ratios L_r) as in equation (4.12),

$$\begin{aligned} (H_p)_{\min} &= H_m (L_r)_{\min} = 0.067\text{m} \times 8 = 0.54\text{m} \ (1.76 \text{ feet}) \\ (H_p)_{\max} &= H_m (L_r)_{\max} = 0.067\text{m} \times 35 = 2.35\text{m} \ (7.7 \text{ feet}) \end{aligned} \tag{4.13}$$

Kinematic and dynamic quantities are scaled-up based on the Froude number, as was established in Chapter Two. Water pressure head is treated as a geometric quantity (height). Frequency components are scaled based on the inverse square root of the scale ratio (Table 2.1),

$$f_r \doteq \frac{f_p}{f_m} = L_r^{-1/2} \tag{4.14}$$

Therefore the frequency ratio, f_r, varies between 0.353 and 0.169 for scale ratios 8 and 35, respectively. The relationship is certainly non-linear, and this is the reason the results of this work have to be converted (or up-scaled) before any comparison is made. The relationship of the frequency ratio to the scale ratio is shown in Figure 4.16. Some confusion in this respect could

be possible if it is considered that the analytical formulation provided results in non-dimensional parameters. Therefore, the results of the analytical work are applicable to any size model (which is theoretically correct). This is not true, however, for the experimental results which have to be up-scaled. The scaling may be questioned since there is no velocity, thus, the basic scaling law (Froude law) this is based, on does not really exist (**Fr**=0). It is important, however, to keep a degree of compatibility between the results presented in this chapter with the ones presented in the next chapter.

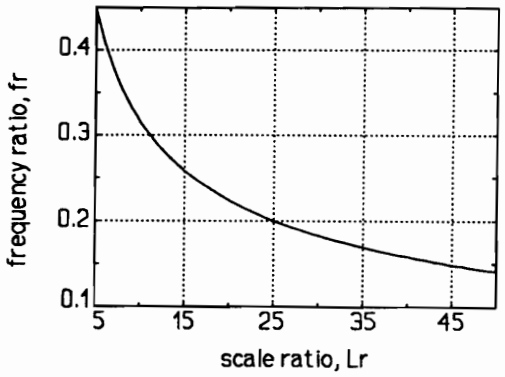

Figure 4.16 The Froude law relationship between the frequency and scale ratios.

From the relationship in equation (4.14) it follows that the prototype frequency components are smaller than the model's depending on the scale ratio value. In describing the results in the next section, both maximum and minimum values will be given, based on the respective values of the frequency ratio.

4.5.2 Comparison and Comments

The work presented by T. D. Fagan [73] in 1987 and J. C. Hsieh [74] in 1988 is perhaps the first ever that dealt with the vibrations of inflatable dams. Fagan considered the effect of membrane weight on a 2D cylindrical inflatable membrane without any external loading. The effect of material extensibility was neglected and he used a finite difference approximation to solve his equations of motion. He considered a double anchored system. The internal pressure was non-dimensionalized with the membrane unit weight, and the base length with the perimeter of the dam. Mode shapes presented are perhaps the most valuable information ever published on inflatable dams. Results that are of interest for comparison with this work are also found in Hsieh's dissertation.

J. C. Hsieh presented his doctoral work on 2D double anchored dams in a similar way. His results show graphs with various internal pressures and impounding water heights. There is not enough information presented to convert his results to the same format of this work which is by nature (double anchored) incompatible. Most of his work dealt with water-filled dams.

The current experimental results are converted so that they can be compared with the

analytical work. Several assumptions have to be undertaken which make this comparison even more unreliable. The base of the model dams (which does not really exist for single anchored dams) is assumed to be $0.1\pi H$ ($2\pi R=\pi H$). The radius R is assumed to be $0.5H$. This results in a virtual *alpha angle*[1] of 1.8π radians. It must be mentioned that what is considered a base length in the experimental tests (here) varies with respect to internal pressure, upstream water depth, method of inflation, and the amplitude of oscillations. An average value has been assumed for the purpose of this comparison. The results are transformed in terms of lambda as defined in Hsieh's work,

$$\lambda = \frac{\mu \omega^2 R}{q} \tag{4.15}$$

where μ is the membrane mass per unit area ($0.0169 kg/m^2$), ω is the natural frequency in radians per second, R is the radius of curvature (0.0335m), and $q=P_i\,\rho g$ is the internal pressure ($\rho=1000 kg/m^3$, $g=9.81 m/s^2$). Based on the information furnished thus far, the possible experimental lambda values range from 0.00229 to 0.115, for the fundamental frequency that was identified around 85 to 90Hz.

The analytical lambda value for the considered base length, is 0.0681 for the first mode of vibration, which is within the range given for the experimental results. If a frequency scale-up is not attempted then the experimental lambda value is between 3.2 and 36, which can be reasonable for an alpha angle smaller than 2.51 radians (144 degrees).

Concluding, the experimental results here include the analytical values but with a substantial margin of error. Therefore, it cannot be claimed that there is an agreement or not. This is not surprising considering that the compared results are incompatible in many aspects. Unfortunately, there are no previous results with air-inflation and impounding water, a case of particular interest to the industry. Even more important, it was not possible to locate (published) previous work for single anchored dams. It is almost certain that the industry performed such tests which were not published for competition reasons.

---

[1] In J. C. Hsieh's [74] work the *alpha angle*, α, is defined as "the central angle of the circular membrane arc", from the one base anchor to the other (pp. 13, 14). This results in α being equal to the (effective) perimeter over the radius of curvature.

Chapter Five

OVERFLOW VIBRATIONS

Much of the research done during the 1960's was initiated after the catastrophic failure of a Fabridam (inflatable dams made by Firestone), under expected or unexpected overflow conditions. It is possible to make the material of the dam strong enough to withstand any given overflow height, but at a heavy cost. As with other construction material (steel, concrete, timber) the performance of the structure is optimized with respect to its cost in order to be marketable. However, before such optimization is made possible, and going beyond any static analysis, the mechanics of large amplitude vibrations must be revealed.

5.1 Introduction to Water Overflow

Inflatable dams are used for many applications as described in Chapter One. Many of these applications do not expect overflow conditions, especially when their main installation purpose is to contain some kind of fluid (even mud). There is a significant number of cases, however, that for most of their lifespan are expected to have some degree of overflow.

Few people could have predicted the recent floods in the Midwest and the disastrous effects of rushing flood waters. There is an empirical probability for the occurrence of such an event; no doubt it has been revised. For weeks, every television station was broadcasting scenes of floodwaters forcing their way into farmlands and residential areas, creating literally billions of dollars in damage. The catastrophic power of storm floodwaters was in its full glory, a testimony to the need for considering such events beyond any simplistic probability of occurrence.

The inflatable dam used at the Mangla Dam construction, Pakistan, failed on February 12, 1966, under overflow conditions. Although much higher overflows were expected, a "minor" water-surge forced the dam into longitudinal and cross-sectional random and periodic oscillations (Binnie *et al.* [14], 1973). The design of this dam (made of three sections) was to withstand a load ratio, h_u/H, equal to 2.3, nominal. The dam was designed with an inflated height, H, of 3m (10 feet) spanning over 61m (200 feet) per section (actual sizes were 76.2m or 250 feet, 63.4m or 208 feet, and 74.4m or 244 feet long for sections one to three, respectively).

By design, the nominal operating internal pressure was not to exceed the 0.61m (two feet) head over the upstream water head. Therefore, at a load ratio of 2.3 the pressure ratio, P_i/h_u, was limited to 1.09 maximum (H=3m or 10 feet, h_u=7m or 23 feet). In cases of large amplitude oscillations the internal pressure was specified to be rapidly decreased or increased.

Failure at overflow occurred at $2m^3/s$ per unit length (74 cubic feet per second per linear foot). From the equations listed in the literature review, equations (1.1) and (1.2), it follows that the overflow height was almost 2.1m (7 feet) tall, and the upstream water head was 6.1m (20 feet) high. The internal pressure of the dam was 5.8m (19 feet) of water head. Therefore, failure occurred at a pressure ratio P_i/h_u=0.95, and a load ratio h_u/H=2. The aspect ratio of the section that failed was L/H=24.4 (third section).

Today, the companies that market inflatable dams refer to an overflow height of only four tenths of the height of the dam (recently this limit has been increased). Higher overflows are allowed with modification of the dam. The fact that the companies today are still not very convincing to some prospective buyers that their dams are stable, is not a surprise. During the last 25 years the inflatable dam industry in general, did not demonstrate sufficient research on the dynamic response of inflatable dams. It is likely that the companies contacted their own research, but nothing was ever known to be published in any engineering society at large.

In fact, one particular company has its dams equipped with a flow separation fin (patented), to force the water to land away from the dam's downstream base. It has been identified that the most important reason for the dams' vibrations is the water action at the downstream base of the dam. This fin, however, is expected to bend under heavy overflows to the point that it is no longer useful. It is currently manufactured up to 30cm (12 inches) long. It is estimated that the rubber material is the single most expensive item in the inflatable dam construction. Moreover, adding to the cost the specialized process needed for the manufacturing of the fin, this builds up

the additional cost to prospective buyers.

During overflows, there is a considerable difference in the response of the models depending whether there is a free downstream water-escape or not. It is therefore extremely important to have knowledge of the possibilities of not only a potentially large overflow but also about any downstream obstacles.

Overflow conditions must be seriously considered in the design of inflatable dams. Overdesigning the structure because of lack of understanding of the mechanisms of their vibrations is nothing else but a waste of money. Overflow conditions exciting the dam from minuscule amplitude levels to the extreme oscillations that cause membrane tearing and catastrophic failure is the basis of this work.

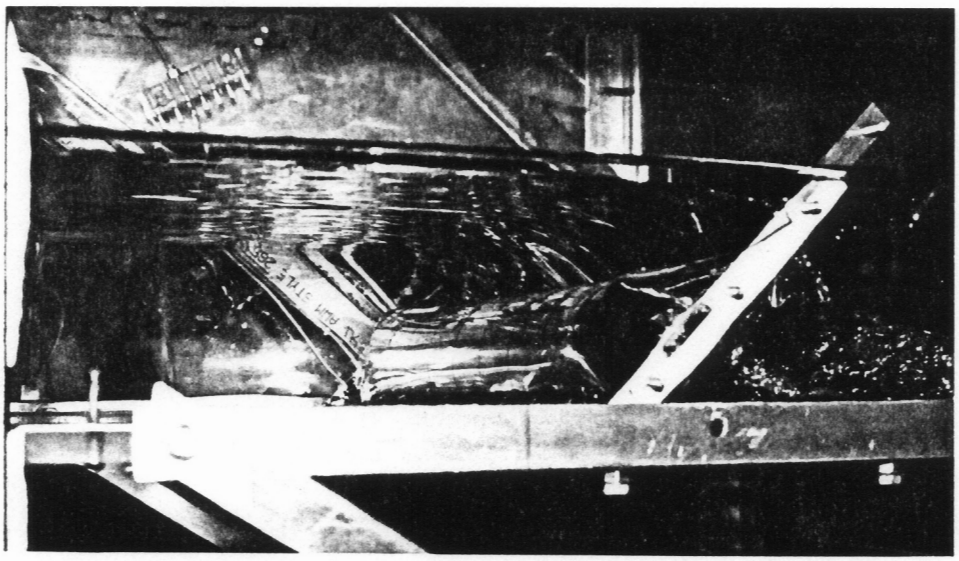

Figure 5.1 High overflow conditions at the 61x61cm (2x2 foot) test section facility. Model is made with polyester. Overflows exceeding the height of the dam were also tested, most of the time resulting in catastrophic failure.

5.2 Flow Visualization

Flow visualization of the overflow conditions is an integral part of the understanding of the fluid mechanics around the inflatable dam. The visualization technique used here, employed a Helium-Neon laser to form a laser-sheet. Natural air bubbles entrapped in the flow stream as well as suspended particles (dirt) created the moving-particles image captured by still and video cameras. The resulted pictures could also be used for stream velocity measurements, but the process was too expensive to be adopted.

The visualization took place in the 61x61cm (2x2 feet) test section, with a model length over height ratio (aspect ratio), L/H=9. With such a small ratio, the dam was not expected to show any significant longitudinal behavior, and therefore it was suitable for cross-sectional flow visualizations.

Other visualization methods used Hydrogen bubbles, and dyes. These were primarily used to check on the upstream flow conditions, with respect to the effect of the platform's leading edge, and the nature of the boundary layer.

5.2.1 Upstream Flow

Approaching the upstream side of the dam, the streamflow is forced into a significant contraction. The crest overflow height, h_o, and the upstream water head, h_u, were reported to have a relationship as the one given in equation (1.1), Chapter One. This contraction forces the flow to be streamlined around the body of the inflatable dam. While doing so, an apparently stable vortex is created at the upstream base of the model. In addition, there is no boundary layer noted by the various visualization methods, and therefore it is assumed that the boundary layer is of negligible thickness. Even if a boundary layer of substantial thickness was detected, this is not as critical as it may seem, because of the high flow contraction ratio, h_u/h_o.

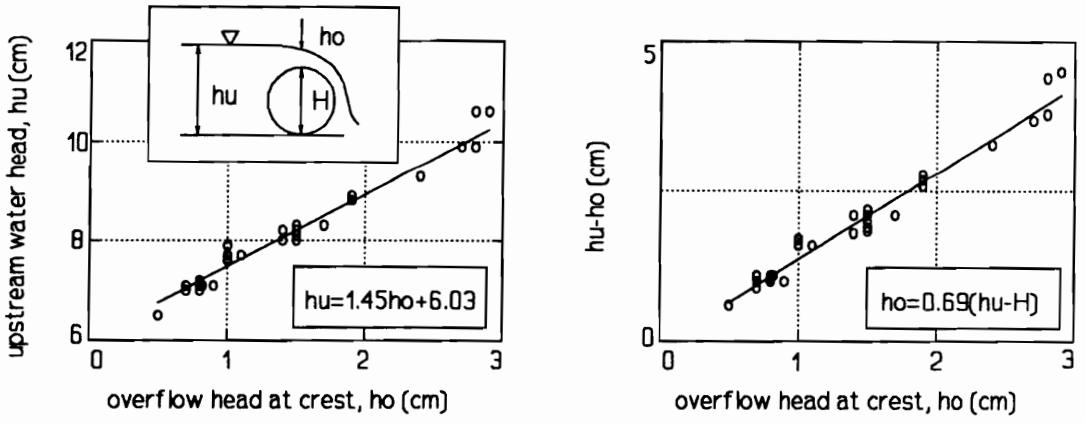

Figure 5.2 Upstream water head and overflow water head relation. The height of the dam varies up to 2% for the full internal pressure range and the flowrate range of tests, L/H=8.4. [C12-58]

The contraction relationship is found by curve-fitting the experimental data of the two parameters, upstream water head h_u, and overflow height h_o. The data are fitted to a straight line. The findings (Figure 5.2) are in agreement with Alwan's results, equation (1.1) in Chapter One.

The graph at the left considers the contraction relation, while the graph at the right considers the relation given in equation (1.1). The contraction ratio is

$$\frac{h_u}{h_o} = 1.45\left(1 - \frac{H}{h_u}\right)^{-1} \tag{5.1}$$

where h_u/H is the load ratio. For the test cases shown in Figure 5.2 the load ratio varies from 1.15 to 1.75. Therefore, the inverse load ratio H/h_u varies from 0.869 to 0.571, respectively. This results in a contraction ratio variation between 11.1 for small overflows and 3.4 for high overflows that resulted in failure. It is reasonable to assume that such levels of contraction minimize any boundary layer that might have been developed upstream of the dam. This, in addition to the flow observations, strengthens the presumption that the flow modelling is correct. There are concerns, however, with respect to the velocity profile at the crest of the dam. It is expected that a thick boundary layer upstream of the dam will produce a different velocity profile resulting in a relocation of a possible flow separation point. Relocating this point from the downstream side of the dam using a trip-wire showed only a marginal effect, as mentioned in the literature review in Chapter One. Therefore, the dam response may be indifferent to overflow velocity profile as well.

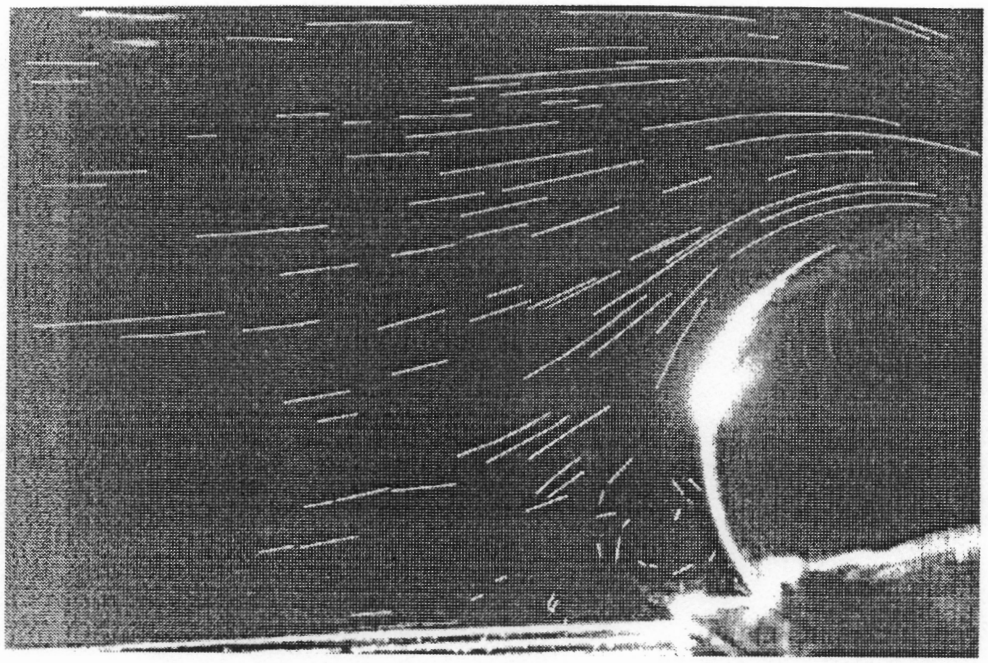

Figure 5.3 Laser-sheet flow visualization of naturally entrapped air bubbles and other suspended particles, H=6.7cm, L/H=8.4. The curved intense-white line is the upstream face of the model dam.

The vortex formed at the upstream base of the dam was observed under different velocities and internal pressures and it was not seen to have any direct effect on the dam's vibrations. Even at high amplitude vibrations, the vortex appeared to be driven from the dam motion rather than driving the dam. This is in agreement with other reports that identified the cause of the vibration to be at the downstream side of the dam.

The particle streaklines just upstream of the dam shown in Figure 5.3, follow the dam's shape and form a streamlined area of disturbance at the upstream base of the dam, as mentioned earlier. The oscillation amplitude level did not appear to have any dramatic effect on the basic flow pattern before and over the dam. Based on these visualizations alone, it can be hypothesized that the major disturbance on the dam occurs after the crest of the dam. It is possible that under a higher Reynolds number (as is the case in the prototypes), this upstream vortex plays a more significant role in the dam's oscillations. Therefore, the location of the initial disturbance may be on the upstream side of the dam.

5.2.2 Dam Oscillations and Downstream Flow Characteristics

The downstream water flow characteristics were not ideal for flow visualization. However, video movies of the oscillating dam showed some very interesting features of the vibration motion. Side views as well as plan views were studied. Plan or overhead views showed that the dam has a back-to-front oscillation. The amplitude was a function of the upstream velocity, and maximum amplitudes as large as $0.2H$ were observed.

Of particular interest are the slow motion movies of the side view vibration scenes. The video tapes were processed through a continuous frame viewer VCR (VHS), that has the ability of frame to frame advancement. Moreover, the resulting picture is completely stable, and completely free of stray lines and other visual noise.

These slow motion tapes reveal that the cross-sectional motion of the dam, has the principal axis of oscillation inclined at approximately 30 to 40 degrees. The direction of it, is from the downstream side of the dam, going upwards to the upstream side of the dam, as shown in Figure 5.4. This finding is of a particular importance, as it reveals the area (and direction) where the disturbance (or force) responsible for this motion is most likely to be applied.

Working more closely to the flow at the downstream side of the dam, it was not possible to get any flow visualization, like traveling vortices, but it was clear that the flow was highly turbulent, better described as chaotic. During very large oscillations, slow motion movies could

give the impression that the water is actually pulling the dam at its downstream base. In return the dam's elasticity causes the model to retract. This combination repeats itself, and results in the oscillatory motion seen. On the other hand, it could be said that the model dam actually pushes or "shoots" the water downstream, as a wave-maker would. Therefore, the vibrations due to water action may be much more complicated, likely to involve self-sustained oscillations under small perturbations.

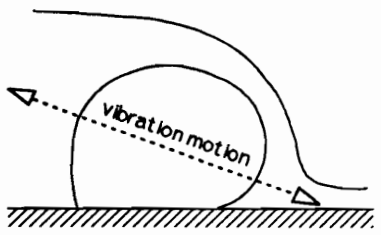

Figure 5.4 Observed motion of large amplitude vibrations.

It must be emphasized that the slow motion movies give a good indication of the motion of the vibrating models. However, they do not constitute a proof of the mechanics of vibration and therefore they should only be treated as such.

The observations made thus far are generally in agreement with other workers' reports, and also with the industry's effort (mentioned earlier), to force the water to land away from the downstream base of the dam. In a later section it will be described how vibrations are eliminated by restricting the turbulent flow action at that particular point, and therefore advancing the current hypothesis to a proposition. In addition, it will be described how the response of the dam in some cases is likely to be flow-driven, and in other cases driven by something else (perhaps the structure's own elastic forces).

5.3 Non-Dimensional Parameters

The frequency response of the inflatable dams was shown in Chapter Four to be a function of the pressure ratio P_i/h_u, and the load ratio h_u/H. Other parameters were also noted in Chapter Two (like the Froude number and the Reynolds number) because they are traditionally used in other fluid mechanics or flow induced vibrations problems, and can be used here as well.

It is interesting to note, however, that the pressure ratio and the load ratio identified in the Free Vibrations chapter due to the particular circumstances there, can be generalized for the overflow vibrations. In doing so, it is shown that some of the traditional non-dimensional parameters become obsolete, or they are simply not capable of describing the dam's response.

5.3.1 Reynolds Number

The Reynolds number $\upsilon l/\nu$, a measure of inertia forces to viscous forces, is considered here to have its velocity parameter (υ) being the upstream average velocity V, and its governing

length (l) being the upstream water head h_u. Alternatively the governing velocity may be considered to be the overflow velocity, and the governing length to be the overflow height h_o. However, there is no real difference between the two sets of parameters, since there is a linear relationship between the upstream water head and overflow head, as shown in Figure 5.2. This, in addition to the fact that this is a free surface flow which makes the average velocities linearly dependent on the flow depth, results in no advantage to either set of parameters.

Therefore, for a given flow rate (Q) the Reynolds number remains constant for any change in the upstream velocity or the internal pressure, the parameters that govern the response of the inflatable dam. This is shown by considering that

$$\mathbf{Re} = \frac{\upsilon l}{\nu} = \frac{V h_u}{\nu} = \frac{Q h_u}{A\nu} = \frac{Q h_u}{L h_u \nu} = \frac{Q}{L\nu} \tag{5.2}$$

where A is the flow cross-sectional area, and the rest of the variables are as defined earlier throughout this work. All the parameters in equation (5.2) are defined as constants for a given set of experiments (constant flowrate, Q). For different flowrates the constant is shifted analogously as will be shown later-on.

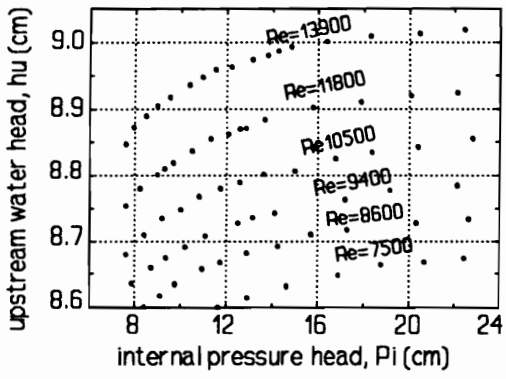

Figure 5.5 Upstream water head drop versus internal pressure head drop, under constant flowrates (Q), L/H=27. [C151-233]

It is mentioned earlier that the upstream velocity changes in a given flow rate. This is true if the internal pressure of the dam changes, which results in a change of the dam's height, which in turn results in a change in the upstream water head. The internal pressure head to upstream water head relation is shown in Figure 5.5, for different Reynolds numbers. For a given Reynolds number the flow rate is of course constant in this problem.

The upstream water head drop is equal to the dam's height drop. Therefore, it is easy to verify from Figure 5.5, that the maximum dam's height drop does not exceed 0.15cm for the given range of h_u and P_i. For a full pressurized dam height H=6.7cm this represents only 2% reduction. Regardless of the small deviation, the dam height is not considered constant. The graph obtained if the pressure ratio P_i/h_u and load ratio h_u/H are used instead, is not identical to Figure 5.5. as it would be if H was considered constant.

It was shown that the Reynolds number remains constant for some of the parameters that affect the response of the dam (internal pressure and upstream water depth). In order to make the Reynolds number more indicative of the problem, its governing velocity and length may need to

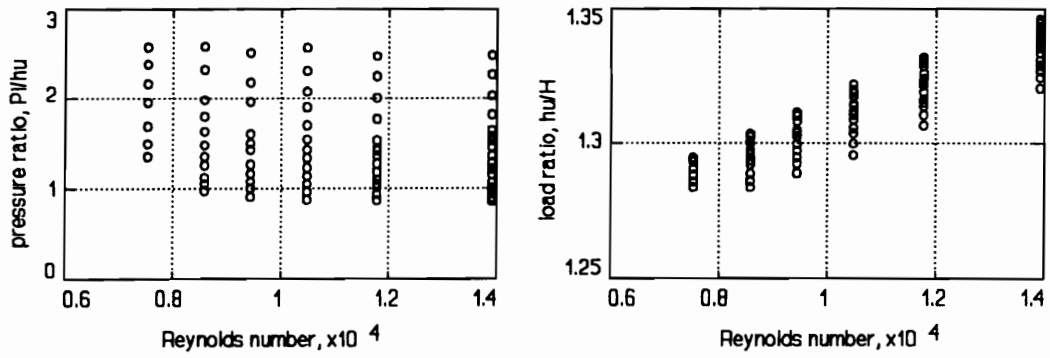

Figure 5.6 Reynolds number relationship (**Re**=Vh_u/ν) with the inflatable dam's response governing parameters, the pressure ratio and the load ratio, L/H=27. [C151-233]

be redefined. In lieu of other independent velocity and height components related to this problem, this is not possible. Therefore, it will be proposed that although the Reynolds number remains an important factor for "correct modelling practice", as noted in Chapter Two, it may not be sufficient to describe the conditions under which a specific dam response occurs. Figure 5.6 further illustrates the points made about the relationship of the Reynolds number and the response governing parameters established in the free vibrations tests.

5.3.2 Froude Number

The Froude number $\upsilon/(gl)^{1/2}$ is predominantly used for free surface flows due to the gravity forces involved. The governing velocity υ is defined as the upstream velocity V, and the governing length l as the upstream water head h_u. Unlike the Reynolds number, the Froude number does not turn into a constant, but instead it varies with the governing parameters, the internal pressure head, P_i, and the upstream water head, h_u.

The range of the Froude number's variation with respect to the response governing parameters can be seen in Figure 5.7, which presents data with the same Reynolds numbers as in Figure 5.6 and Figure 5.5. It is evident that the Froude number varies along with the parameters of interest, and therefore it is expected to be possible to describe the conditions under a specific model response occurs.

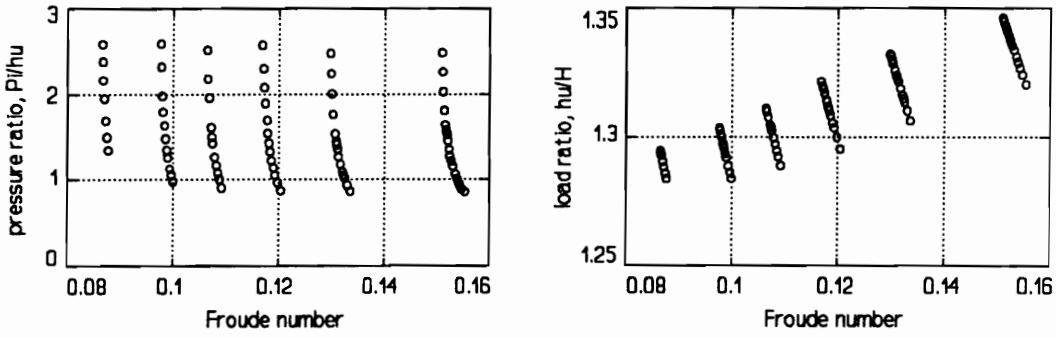

Figure 5.7 Froude number relationship ($\mathbf{Fr}=V/(gh_u)^{1/2}$) with the response governing parameters, the pressure ratio and the load ratio, L/H=27. [C151-233]

5.3.3 Load Ratio, h_u/H

Load ratio was rationalized in Chapter Four to relate the applied hydrostatic load with the maximum hydrostatic load the dam can impound. In the same definition the load ratio may still be regarded as making use of the same rationale, now that there is overflow. Therefore, the upstream water head may be considered as the static part of the total load applied on the inflatable dam, a combination of hydrostatic and hydrodynamic forces.

The relationship of the load ratio with the Reynolds and Froude numbers was described in the previous sections. It remains to be seen how useful this parameter will be in comparison with the primary oscillation frequencies resulting from overflow conditions. It must be recalled that without overflow, the frequency of oscillation versus load ratio graph presented in Chapter Four, Figure 4.9, resembles the graphs showing the Reynolds number invariance. Nonetheless, this is not the case for the overflow vibrations.

5.3.4 Pressure Ratio, P_i/h_u

The *pressure ratio* has been shown to be a good parameter for defining the free vibration response. It should be noted, however, that an inverse pressure ratio versus the frequency of oscillation of the structure, produces similar graphs as the Froude number versus frequency. An inverse pressure ratio is very close to the load ratio because of the common parameter (h_u) relation, but they are not the same. It will be shown that they produce results close to mirror images, which is deceiving. In fact, the relationship between the internal pressure head and the height of the dam is non-linear (Figure 5.5).

5.4 Primary Vibration Frequencies

As was the case for free vibrations, the frequency components are identified based on spectral analysis. There is a total of 468 response measurements of flow-induced vibrations. All cases are with air-inflated models. In addition, there are several trial tests with water-filled models, or a water/air combination inflation medium. The first eleven tests have only one response measurement per case number, at a sampling frequency of 5000Hz for 1.64 seconds. The material used is 0.0005 inch (0.0127mm) thick polyester (Mylar^R), with L/H=8.4.

For all the next 47 tests two response measurements per case are used; one pressure transducer is installed inside the model, and the other transducer is installed outside the model with a 4-5 inches long tubing (1/16 inch internal diameter). The purpose of this setup is to verify the relationship of the two signals, as illustrated in Chapter Three, Figure 3.1 and Figure 3.2. These cases have an L/H ratio equal to nine. Some of the tests showed very high amplitude oscillations, presumably due to the high flow rates possible. The sampling frequency F_s is 2500Hz for 3.28 seconds. The material used is a 0.0005 inch polyester.

The last 261 test have two response measurements as well, from pressure transducers at each end of the model. The sampling frequency F_s is 600Hz for a sampling period T_s=10 seconds. The material used is 0.002 inches thick polyethylene, with L/H=27. For a short period of time it was also possible to observe the 0.0005 inches thick polyester material.

5.4.1 Response Frequency versus Pressure Ratio

Similar results were presented in Chapter Four, Figure 4.6 and Figure 4.11. It was noted that the primary frequency of the system, increases with a reduction in the pressure ratio, for a constant load ratio. Similar graphs are produced here for the overflow test cases. The set of cases represented in this section has a moderate Reynolds number of 13,900 compared with the maximum used throughout this work, of 36,800. Regardless of the Reynolds number, however, the pressure ratio must be low enough to permit an oscillatory response.

Due to the great difference of power levels between the spectra across the pressure ratio range, a linear energy density scale is not practical. On the other hand, a decibel scale naturally amplifies the low energy frequency components, compromising the graph's clarity. Colored contour plots of the power spectra levels are therefore the best choice for a good data visualization. In lieu of color graphs in this presentation, single-level complementary contour plots are the next acceptable choice.

The first four highest power-level frequency components are presented in the left graph of Figure 5.8. The highest component for each spectra (one per pressure ratio value), is noted with

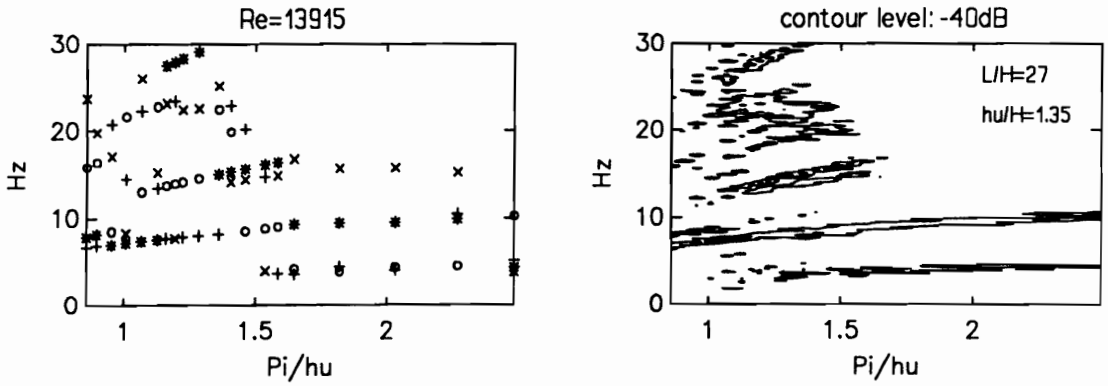

Figure 5.8 *Left:* Primary frequency components versus the pressure ratio. From high to low: *, o, +, x. *Right:* Single contour of power spectra versus the pressure ratio. [C214-233]

a star "*", the second highest with a circle "o", the third with a cross "+", and the fourth with an "x". A complementary graph to the right of Figure 5.8 shows the contour lines at the 1dB and -40dB levels. The level of 1dB just barely appears and cannot be distinguished. Colored plots on the computer screen, however, verified the 1dB level's locations to be the same as the location of the stars "*" at the left graph. The contour plot is complementary to the points-plot, because in the points-plot only the four highest frequency components are included (for clarity reasons). Therefore, some frequency-pressure ratio trends are lost, based on the modes of vibration that dominate the response of the model.

A single mode of vibration (if the same mode of vibration exists throughout the pressure ratio range) can be identified by the notion of lines the graph at the left produces (Figure 5.8), or by the contour lines in the right graph. There is a general reduction of the frequency of oscillation of a given vibration "mode", with a reduction of the pressure ratio.

This is not in full agreement with the impounding water free vibration tests in Chapter Four. In those test cases, the vibration frequency was shown to increase after a critical pressure ratio (Figure 4.9). In other cases frequency components of comparable energy, were shown to split at a critical pressure ratio, and followed ascending and descending paths thereafter (lower graph, Figure 4.9). It should be noted that the load ratio for the cases presented here (Figure 5.8), varies from 1.346 to 1.355, while the free vibration tests had a maximum load ratio of only 0.82.

The question is therefore raised, whether it is possible for the overflow vibration to exhibit

a similar response, if the load ratio is low enough. Graphs are given for all the overflow cases of aspect ratio L/H=27, comparing the frequency of vibration with the pressure ratio, as was done in Figure 5.8. Careful inspection of the graphs in Figure 5.9 and Figure 5.10, reveals that the response shown in Figure 5.8 is in fact characteristic of the system.

Another question that needs to be answered is the Reynolds dependency of the frequency of oscillation. The frequency of oscillation of a given mode of vibration, does not appear to shift with respect to the Reynolds number. This is made clear if the mode of vibration that varies between 7 to 10Hz is observed for the graphs in Figure 5.9 and Figure 5.10, which does not seem to shift (up or down) with a Reynolds number varying from 7,500 to 15,000. If in fact there is some shifting, this is too small to be detected in the given tests' range. Similar observations can be made for other modes of vibration that are clear enough across the Reynolds number spectrum.

The finding that the frequency of a given mode of vibration is independent of the Reynolds number is very significant in extrapolating the test results, to prototype scale. Moreover, this can help in the suppositions to be made about the mechanics of inflatable dams vibrations. It must be noted, however, that the findings in the given Reynolds number range may not be the same in a range of a few orders of magnitude higher as is the case of the classical flow-induced vibrations of a cylinder.

Although the frequency of vibration does not shift with Reynolds number, the intensity or the energy level does. It is evident from the contour plots in Figure 5.9 and Figure 5.10, that the contour line level must be raised from -60dB to -45dB to produce the same clarity in all the graphs. The contour levels drawn are based on a visual clarity judgment, rather than the actual energy level relationship between the different graphs. The contours are defined at a level that does not produce many lines, but can still show a significant amount of information. Nevertheless, they do correctly represent the general trend of the considered parameters. The case numbers in the graphs of Figure 5.9 and Figure 5.10, are only provided so that they can be matched with the graphs that show a similar relation but with the load ratio instead of pressure ratio.

The actual frequency energy level shifting of the vibrating model dam with respect to its Reynolds number, can be visualized by using again the most dominant frequency component, as is done for Figure 5.9 and Figure 5.10. All the points shown (circles) in Figure 5.11 are the star symbols "*" shown in Figure 5.9 and Figure 5.10, which are the highest spectral energy components per test case. The left graph of Figure 5.11 shows that the highest energy pressure variations increase in a nonlinear fashion with an increase in the Reynolds number. Apparently,

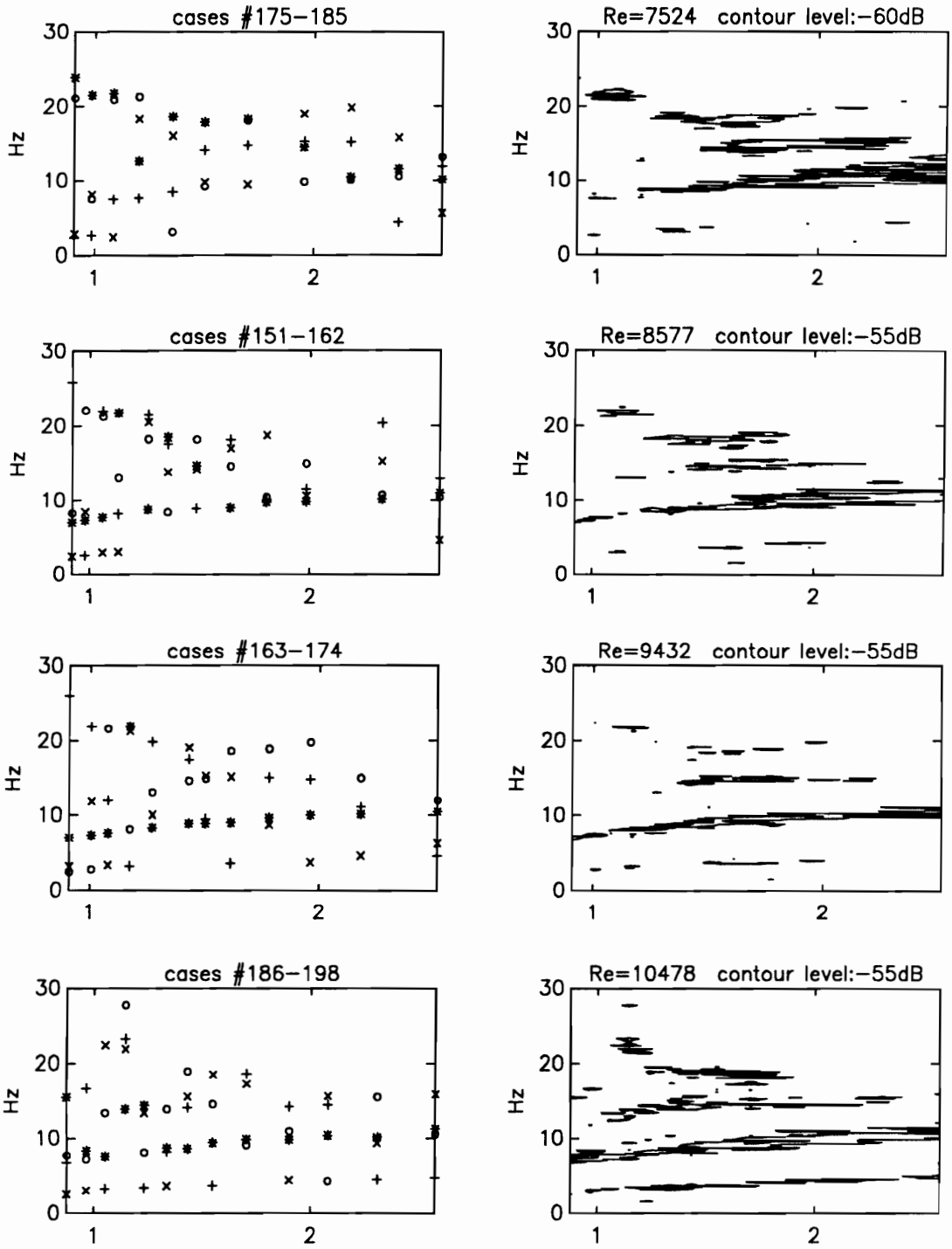

Figure 5.9 Frequency of vibration vs pressure ratio P_f/h_u (x-axis). *Left:* First four most dominant frequency components (*, o, +, x). *Right:* Single level power spectra contour plot.

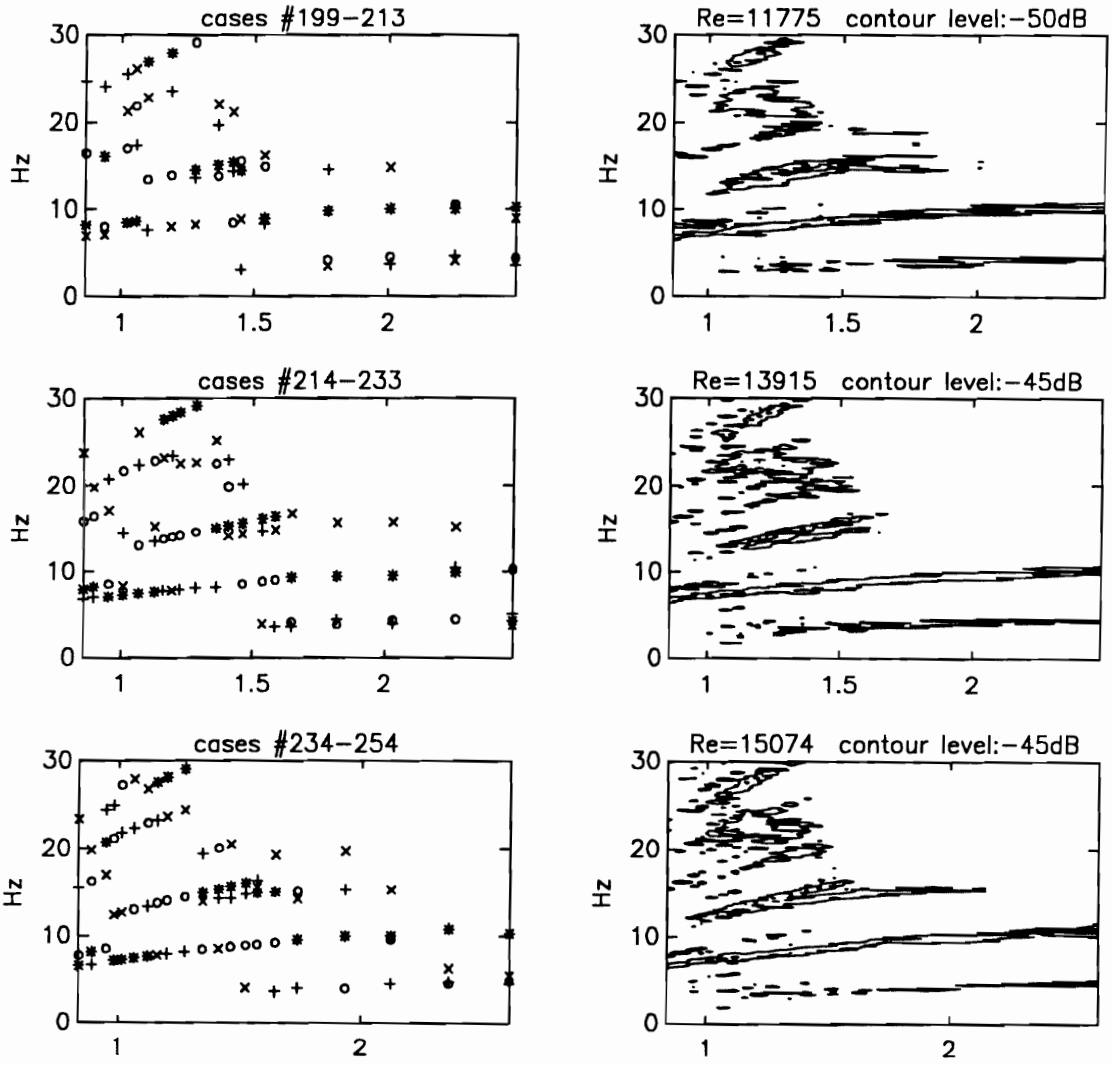

Figure 5.10 Frequency of vibration vs pressure ratio P_i/h_u (x-axis). *Left:* First four most dominant frequency components (*, o, +, x). *Right:* Single level power spectra contour plot.

the energy level starts and ends with low and high level plateaus, as shown by the dotted line. However, the range of Reynolds number is not wide enough to warrant such a conclusion. It must also be recalled that the Reynolds number is the same for equal flow rates, and this is the reason the data in the left graph of Figure 5.11 appear columnized. Each column represents data at the same flowrate (or Reynolds number), with different pressure ratios.

The right graph of Figure 5.11 shows the relation of the pressure ratio with the energy level of the dominant vibration frequency. It is clear that the vibrations suddenly intensify below

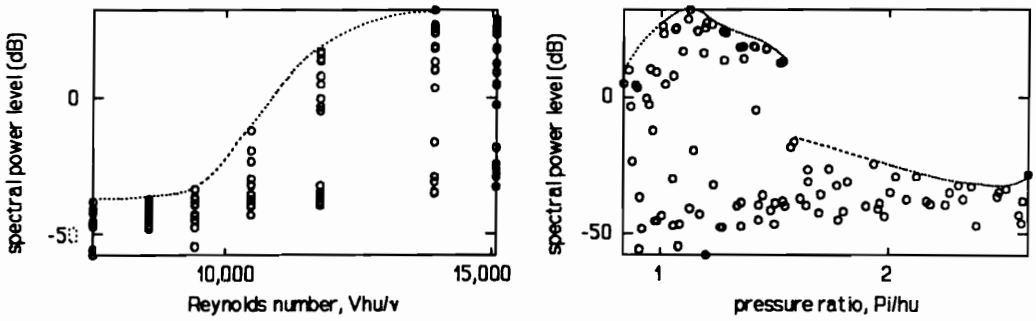

Figure 5.11 Comparison of the primary frequency energy level against the Reynolds number (left), and the pressure ratio (right), for cases #151-254 as shown in Figure 5.9 and Figure 5.10.

a critical pressure ratio of 1.5, and maximize at approximately 1.1. The vibration intensity starts to subside thereafter, but it never returns to the low levels of the pre-critical ratio of 1.5. It must be emphasized that the vibration levels shown are in the decibel scale, $dB=20log(x)$.

For the first time, the inflatable dams' response can be given a threshold point where the dam starts going through very high oscillations. It remains to be seen (in a later section) whether maximum internal pressure oscillations represent maximum displacement oscillations. It is interesting to note, however, that the current design practice of inflatable dams specifies a nominal pressure ratio range that does not exceed the critical point identified here. As a matter of fact one particular company provides typical internal pressure values of their dams, where the internal pressure head is equal to the height of the dam. Therefore, at an overflow head of $h_o=0.1H$ the pressure ratio P_i/h_u is only 0.9.

5.4.2 Response Frequency versus Load Ratio

Similar graphs produced for the pressure ratio, are repeated for the load ratio as well. It is made clear throughout the graphs in Figure 5.12 and Figure 5.13, that the frequency of oscillation (for a given vibration mode) increases for a decrease of load ratio. The load ratio drop shown is very small per set of cases, e.g., cases #214-233. Therefore, the vibration frequency appears to be more sensitive to small changes in the load ratio, than to small changes in the pressure ratio. Again, the case numbers in Figure 5.12 and Figure 5.13 are only provided so that a direct comparison with the graphs in Figure 5.9 and Figure 5.10 is possible. There is no other significance in the case numbering nor any "hidden" parameters.

Unlike the pressure ratio, the load ratio does not remain at the same level for changes in

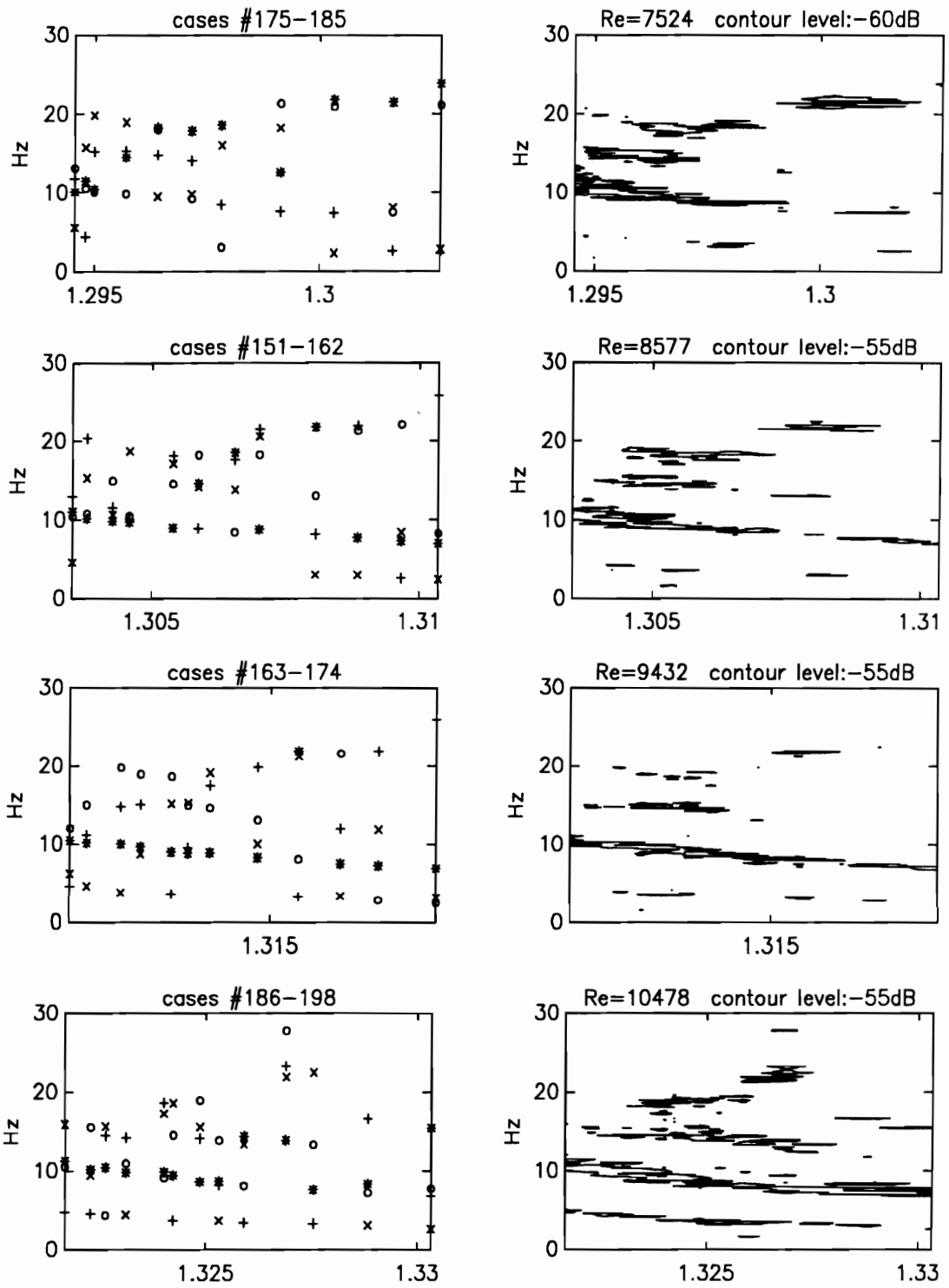

Figure 5.12 Frequency of vibration vs load ratio h_u/H (x-axis). *Left:* First four most dominant frequency components (*, o, +, x). *Right:* Single level power spectra contour plot.

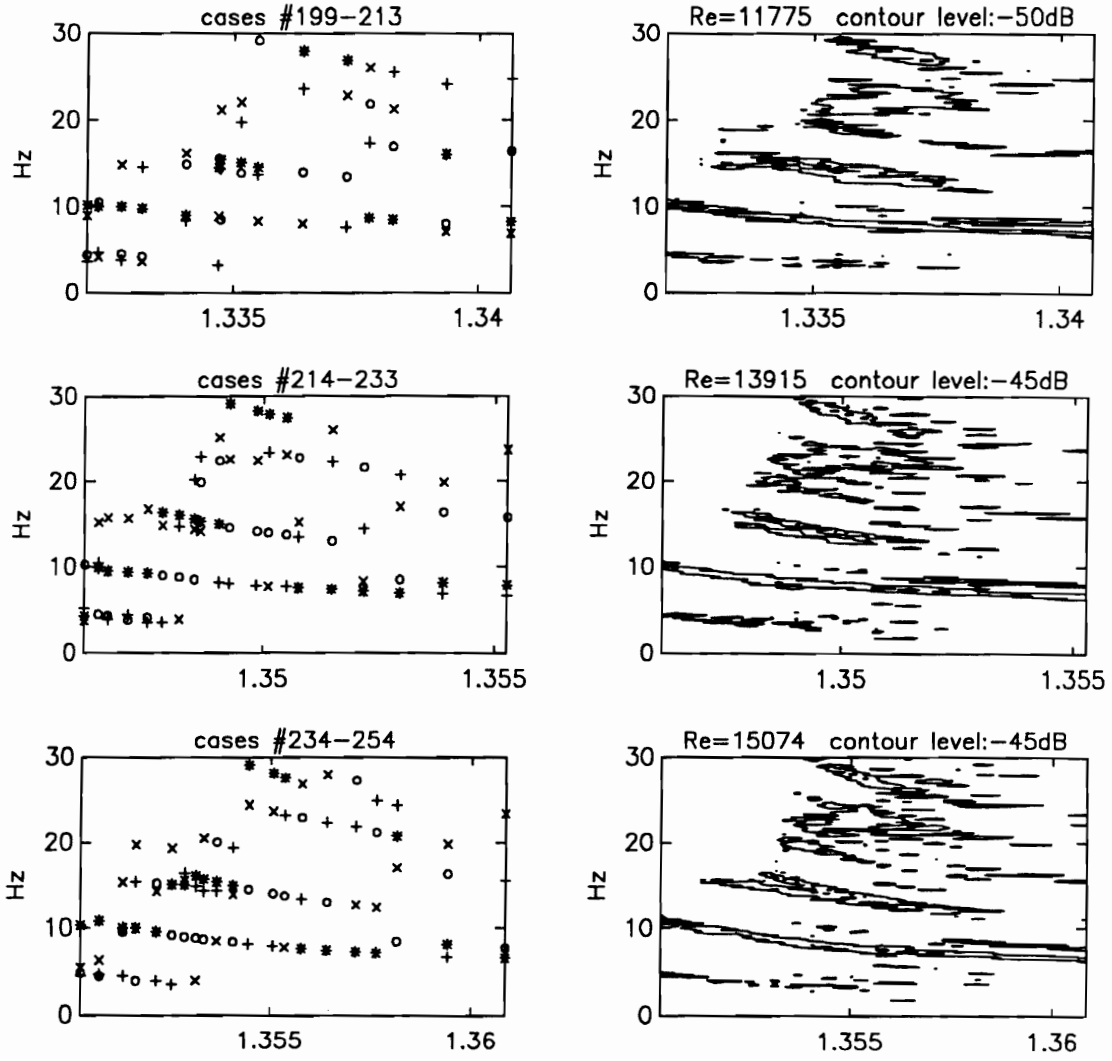

Figure 5.13 Frequency of vibration vs load ratio h_u/H (x-axis). *Left:* First four most dominant frequency components (*, o, +, x). *Right:* Single level power spectra contour plot.

the Reynolds number. This was also illustrated in the right graph of Figure 5.6. It was shown that there is a linear relationship between the load ratio and the Reynolds number. This is not a surprise given the fact that both parameters are dependent on the flowrate with a constant.

Carefully observing the graphs in Figure 5.12 and Figure 5.13, it becomes obvious that the frequency components preserve their levels and shapes throughout the Reynolds range, as is the case for Figure 5.9 and Figure 5.10. However, the horizontal axis of the graphs here shifts its values to the right. As a result, it is not easy to describe what really happens with respect to the load ratio in an xy-plot.

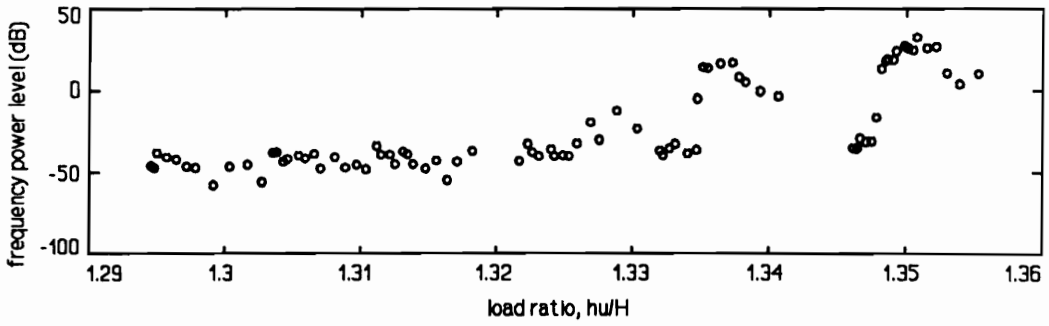

Figure 5.14 Collective plot of all the primary frequency components' power level versus the load ratio, for the cases shown in Figure 5.12 and Figure 5.13.

The highest energy levels of oscillations are expected to take place at the highest load ratio. This is shown in Figure 5.14, where the points at the higher power levels (to the right of the graph) show an expected oscillatory trend.

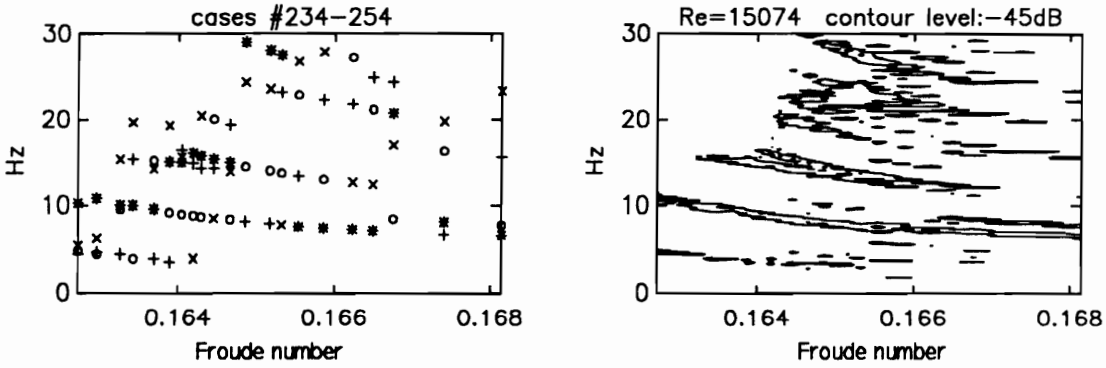

Figure 5.15 Frequency of vibration vs Froude number. *Left:* First four most dominant frequency components (*, o, +, x). *Right:* Single level power spectra contour plot.

5.4.3 Response Frequency versus the Froude Number

The frequency components have a relationship with the Froude number similar to the load ratio. Sample graphs are given in Figure 5.7, Figure 5.15. As a matter of fact the difference between the two parameters is linear in nature as was shown in Figure 5.7, Figure 5.15. Therefore, it is possible to describe the conditions of the model by using only one of the two non-dimensional numbers. In other words, if the response of the dam needs to be described in terms

of the Froude number or the load ratio, either parameter will produce similar results.

5.4.4 Response Frequency versus the Strouhal number

As described in an earlier section, the Strouhal number, fl/υ, is to be used for scaling the frequencies and periodic events derived in model scale, to prototype scale. The governing length, l, may be defined as the height of the dam H, or the length of the dam L. If there is a longitudinal response then the length of the dam is chosen; if the response is cross-sectional then the height of the dam is chosen. The governing velocity may as well be the upstream velocity V. Alternatively, the governing length may be defined as the distance between the downstream surface waves, generated during the dam's vibrations. In such a case, the traveling velocity of these waves would be the governing velocity. There are, however, instrumentation difficulties associated with such phenomena measurements. Although this set of parameters appears to be appropriate to the vibrating dam, it is not practical to be implemented in this work.

Since identification between longitudinal and cross-sectional modes of vibration is not always possible (in this setup), the dam's height H is eventually chosen to be the governing length. Significant cross-sectional response is always present, but the same cannot be claimed for longitudinal response. As a result, the upstream velocity V is chosen for the governing velocity, and therefore the Strouhal number is defined as $\mathbf{St}=fL/V$.

It would be proper to describe any frequency response results (like the ones presented earlier) with respect to the Strouhal number, rather than the model's frequency. However, the relationship between the two variables is linear again, and therefore there is no real advantage in using the Strouhal number to describe the results. Figure 5.16 shows this relationship, as (notions of) lines starting from zero with various angles of inclination. These inclination angles are associated with the flow rate (Reynolds number) of a particular set of cases. Presenting the results with the actual frequency component values, there is the advantage of comparing these results with the free vibration tests in Chapter Four. Those results are without any overflow, and therefore the Strouhal number would have been equal to zero.

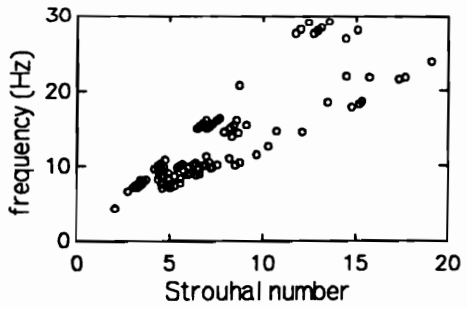

Figure 5.16 Frequency versus Strouhal number relationship for cases #151-254.

It will not be attempted here to scale-up the frequency component results as was done in Chapter Four. Additional data ranges will be generated due to the possible scale ratio values. This will create confusion for the graphs presenting the results of this work.

5.5 Vibration Modes

The "vibration modes" this chapter refers to, are not used in the usual sense of a physical shape with which a structure vibrates at a fixed frequency. Rather, it refers to vibration with a certain frequency that shifts slightly, by slightly changing any of the parameters of the system. The system has been earlier defined as the combination of structure and water. The parameters that govern the system were identified to be the pressure ratio and the load ratio. It is possible that the mode of vibration for such a frequency component remains the same throughout its shift path. However, no evidence is presented that will support such a speculation. Nevertheless, the term "vibration mode" will be used in lieu of any other adequate expression.

In several of the graphs given earlier, it was shown that the primary frequency of oscillation does not stay within the same mode of vibration. For example, the graphs in Figure 5.9 and Figure 5.10, have the highest energy-level oscillation frequencies noted with a star, * ; the star symbols appear at all frequency levels. The same characteristic pattern exists almost along the entire Reynolds range used, where the primary frequency "jumps" from one mode of vibration to the other. This behavior will therefore be considered typical across the Reynolds range. Case set #234-254, is the longest set of cases for a given Reynolds number. Moreover, these cases have a relatively high Reynolds number, therefore, they are ideal for further investigation.

The response frequencies versus the pressure ratio graphs of cases #234-254, are given again in Figure 5.17 in an expanded form to enhance clarity. The graphs, use the highest energy frequency components (stars) to identify the current mode of vibration per pressure ratio value, as was done earlier. Only four frequencies are selected again, and it is possible to see that each pressure ratio case has a column made of the four symbols, that are used to identify the order of the frequency components. There are many more frequency components distinguishing themselves in a given spectral analysis, but as explained in an earlier section, only the first four are possible to be shown based on their energy levels in this graph format. The clarity of the picture would have been compromised if additional symbols were included.

There are some very interesting characteristics in these modes of vibration, that are not found in common structures. There is a general trend shown (Figure 5.17), in which the highest

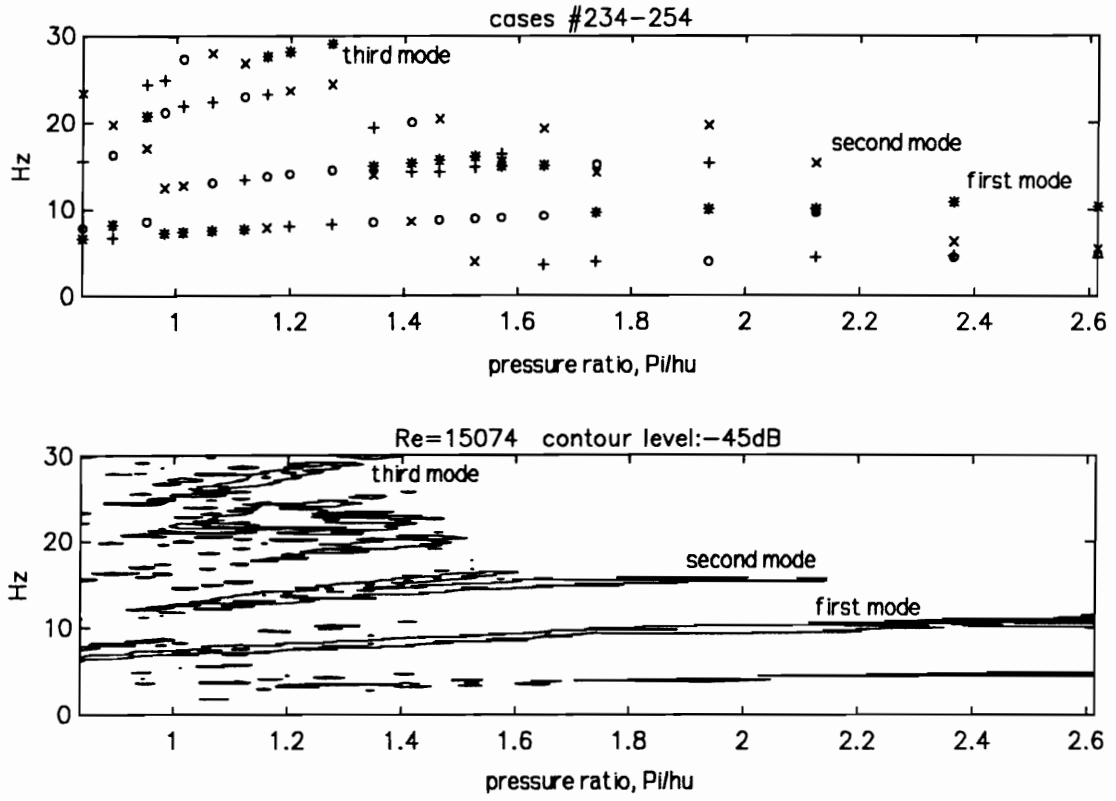

Figure 5.17 Identification of modes of vibration, based on the response frequency paths and the highest energy level frequency component. Energy levels are in a descending order noted with: *, o, +, x.

energy frequency component (noted by *), shifts itself at higher frequency modes with a decreasing pressure ratio. This trend stops at a pressure ratio of approximately 1.15 (* is now located at the third mode). Then, the highest energy mode of vibration plunges into almost a third of the previous vibration frequency, to what is identified as the first mode. After this frequency reduction, the primary vibration mode is one of the high frequency modes again, and after that, it falls back to a lower frequency mode of vibration. All these peculiar frequency shifts could be a result of a highly non-linear system, and/or different excitation mechanisms.

It is possible to identify at least five distinct types of oscillation based on the pressure time response alone. This, in combination with Figure 5.17 and the individual spectral analyses, makes a very good response identification tool. Parts of the time response records are given in Figure 5.18, Figure 5.19 and Figure 5.20.

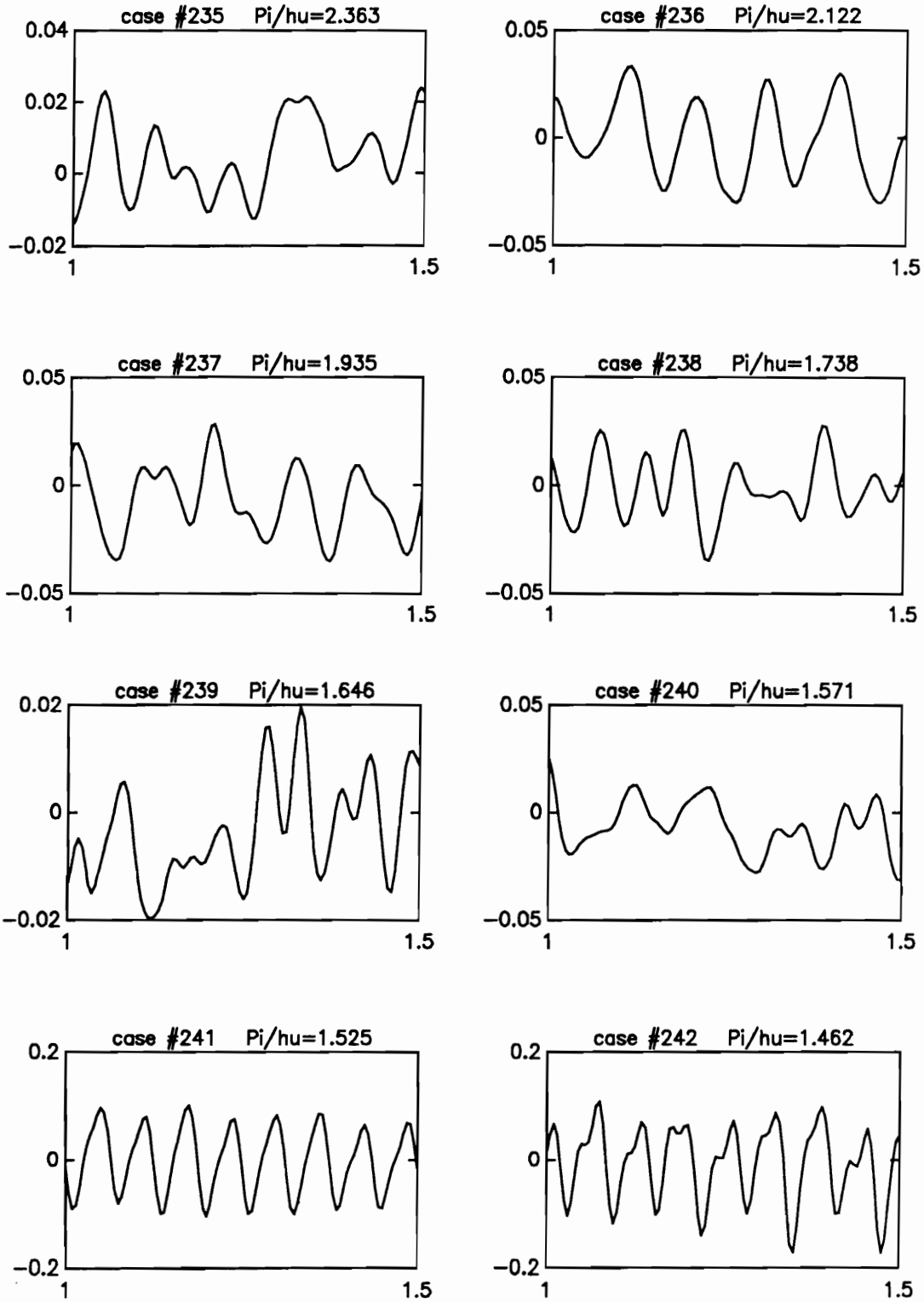

Figure 5.18 Time (x-axis) response of internal pressure variations (y-axis).

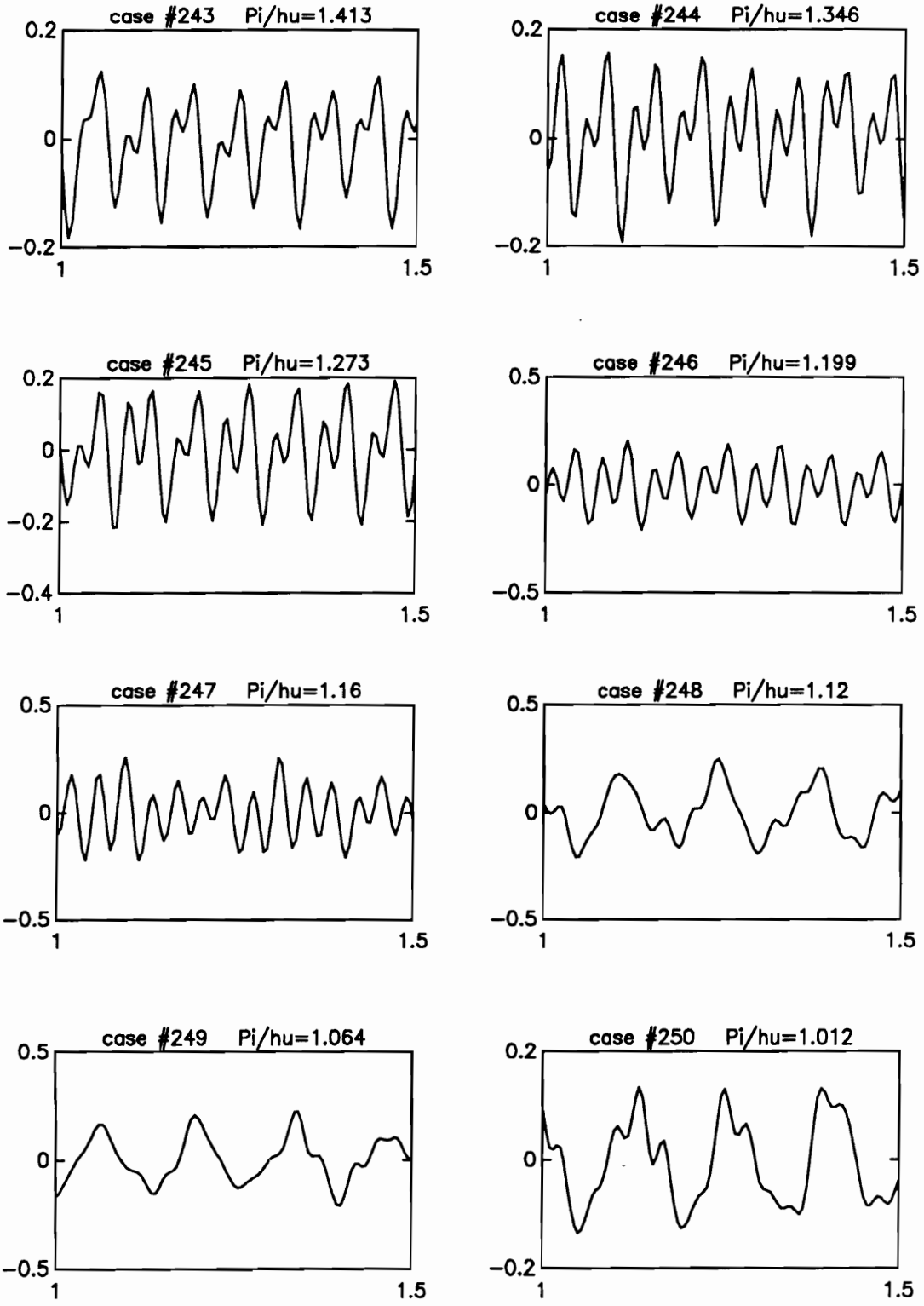

Figure 5.19 Time (x-axis) response of internal pressure variations (y-axis).

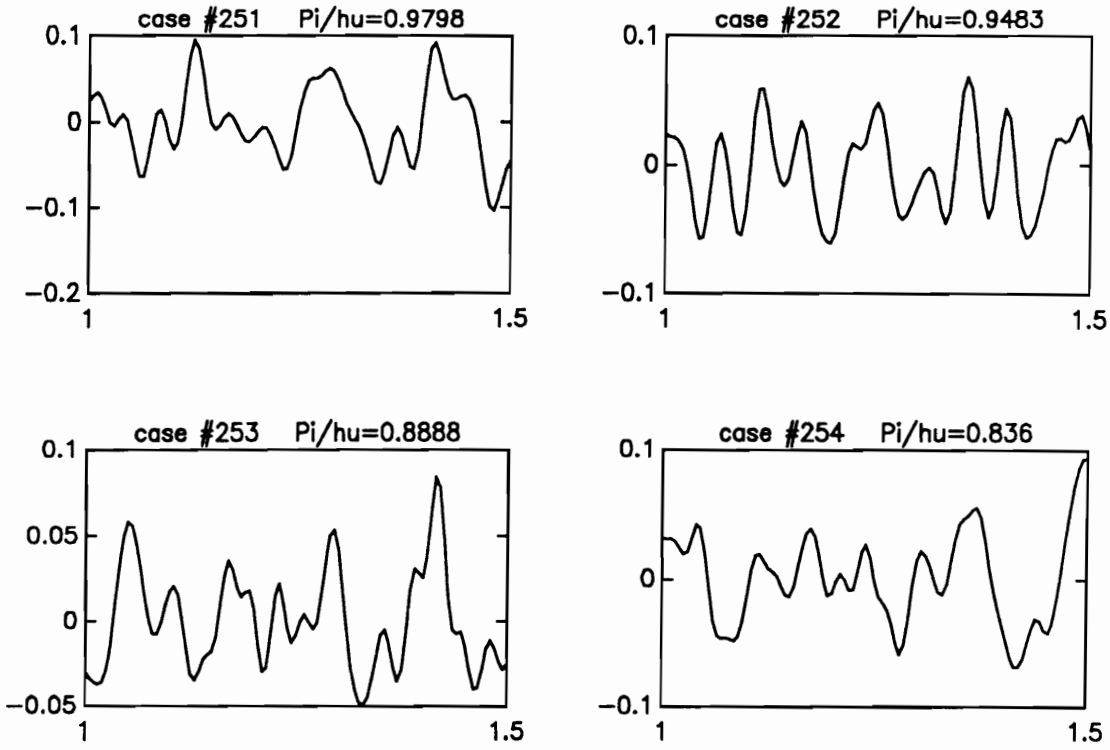

Figure 5.20 Time (x-axis) response of internal pressure variations (y-axis).

The first five time responses in Figure 5.18 are very weak signals (first mode). At a pressure ratio of 1.571 to 1.525 (cases #240-241), there is a transition to a different vibration mode shown in cases #242-244 (second mode). Then, the primary vibration frequency shifts to the harmonic of the second mode frequency, cases #245-247 (identified as third mode). After another transition, the first mode of vibration is shown again for cases #248-251 (Figure 5.19 and Figure 5.20). At a pressure ratio of 0.9483 (case #252 Figure 5.20), the vibration frequency shifts to a mode shown below the third mode (Figure 5.17). The last two time responses shown in Figure 5.20 have similar waveforms to the first mode time response, but they seem to form another mode of vibration.

The highest pressure variations exist in cases #243-250, which include the second, the third, and the first modes of vibration, for a pressure ratio between 1.413 to 1.012. During the tests it was noted that the maximum oscillation amplitudes appeared to be in the second and third modes of vibration. However, the first mode (at a pressure ratio between 0.98 to 1.12) showed the maximum phase difference between the two pressure signals from each end of the dam. Below a pressure ratio of unity, the function of the structure may be at question.

Additional parameters of the graphs presented in Figure 5.18, Figure 5.19 and Figure 5.20 can be identified from the respective graphs in Figure 5.9 and Figure 5.10. Again, case numbers are only provided for identification purposes between the various graphs presented.

5.5.1 Fundamental Mode of Vibration

The order of a specific vibration mode is determined based on the order of the highest energy frequency location, starting from the highest pressure ratio. The first mode of vibration is the one that varies within the 7-11Hz region (Figure 5.17). This particular mode is clearly noted across the whole pressure ratio range. Moreover, it exists at very low signal levels (see the appropriate time response), and it is the lowest significant frequency. Therefore, it can be assumed that this is the fundamental mode of vibration of the system. A vibration mode noted within the 4-5Hz range (lower than the identified fundamental frequency), may as well be a subharmonic vibration mode due to non-linearities in the system, as was suggested for the free vibration tests for a similar phenomenon.

At high pressure ratios the vibration energy is very low. This can be seen from the related time responses, as well as from the right graph of Figure 5.11. The system in these cases consists of a well-pressurized dam that shows a minimum response to the flow disturbances. These disturbances were identified in a previous section to be located at the downstream base of the dam. When the internal pressure is reduced and the pressure ratio reaches 1.15, these disturbances have a more significant effect on the dam.

The time responses for the two ranges of pressure ratios, 1.75-2.6 and 0.98-1.15, have a certain degree of similarity. During the laboratory experiments it was possible to identify the mode of vibration at the pressure ratio range of 0.98-1.15, to be a longitudinal standing wave with a (stable) node at the middle. This is in agreement with the internal pressure phase difference reported at the ends of the dam. It was not clear if the vibration mode was symmetric or antisymmetric. The phase differences, though, point to the conclusion that the vibration mode was antisymmetric. The same response was observed over and over for all the high Reynolds number case sets.

5.5.2 Other Modes of Vibration

During the free vibration tests it was shown that a system with impounding water has a fundamental frequency that varies proportionally with the pressure ratio and inversely proportional

with the load ratio (Figure 4.9). Similar results were also reported for the overflow conditions in a previous section.

Carefully inspecting Figure 4.9 again, it will be seen that at a load ratio of 0.82 the fundamental frequency varies between 13 and 14 Hz, according to the pressure ratio. From Figure 4.10 it can be seen that the critical pressure ratio is between 1.5 and 1.8. After that ratio, impact excitations result in higher energy power spectra frequencies.

In a similar manner, Figure 5.17 displays a frequency component which is identified as the second mode of vibration. This frequency starts with a relatively small energy level (as the frequencies in Figure 4.10), and at a critical pressure ratio of 1.65 it produces high energy oscillations. The primary frequency then shifts to its harmonic frequency.

Although it is not possible to extrapolate the impounding water cases response to the overflow region (Figure 4.12), there are similarities between the two cases mentioned here. Based on these similarities it will be assumed that the second and third modes of vibration as defined in Figure 5.17, are related to the impounding water cases with a high load ratio.

5.5.3 Vibration Mechanisms

Earlier in this chapter it was shown that the Reynolds number has no effect on the frequency of vibration (Figure 5.9 and Figure 5.10), but only on the energy level of the frequency of oscillation (left graph of Figure 5.11). Since the Reynolds number is defined as the ratio of inertia forces to viscous forces, it may be inferred that the viscous forces do not control the period of the phenomena observed. On the other hand, the increase of the oscillation energy levels is merited to the increase of upstream water head, or the increase of the flowrate in general.

Based on flow visualization, it was mentioned earlier that the vibration mechanism may be related to the turbulent flow action at the downstream side of the dam. This random turbulent action, in combination with flow separation phenomena at the downstream side of the dam and the elastic properties of the dam, gives a viable excitation hypothesis.

The frequency of oscillation is greatly affected by the pressure ratio, and the level of the energy of oscillation is affected by the load ratio. Both parameters are controlled by the structural characteristics of the dam, internal pressure and dam height, as well as from the applied load (upstream water head). Therefore, it should be expected that a particular vibration mechanism is more related to the structural characteristics and the applied hydrostatic load, rather than the flow characteristics alone.

The first vibration mechanism proposed is related to the fundamental frequency defined earlier. Viscosity has only a minor effect, and the dam is not driven into a large-amplitude oscillation based on the original disturbance at the downstream base of the dam. Instead, large-amplitude oscillations pre-exist the first mode's large amplitude vibrations. When the dam has a critical pressure ratio between 0.98 and 1.15, it is forced into a structurally driven flow-sustained longitudinal mode of vibration. The major forces in this mode, are the elastic forces of the dam. The fact that the dam has a longitudinal behavior, further supports the proposition that this is not a flow-separation sustained oscillation.

Another mechanism of vibration that is proposed is related to the natural frequencies of the system. These were indicated to be related with the fundamental frequency of the water impounding system. The turbulent action at the base of the dam drives the dam into a two-dimensional behavior. Flow separation generates a negative pressure at the downstream side of the dam. The dam responds by a forward displacement. The random turbulent action at some critical point diminishes the effect of the negative pressure and the dam responds with a backward displacement. The steps are repeated and the dam is put into oscillatory motion. The frequency and the energy level of oscillation are controlled by the internal pressure of the dam and the overflow height.

5.6 Comparison of Different Aspect Ratios

Two aspect ratios are used in this work, L/H=8.4 in the first phase of experiments, and L/H=27 for the second phase of experiments. During the first phase of experiments it was possible to drive the models to failure, given the right conditions. Both phases used models with the same perimeter to maximize their respective aspect ratio. The quantities compared were already presented previously for the L/H=27 aspect ratio. Both aspect ratio graphs are presented here for clarity of the comparison comments.

It was shown earlier that there is a critical pressure ratio, P_i/h_w, where high energy oscillations commence and a second critical pressure ratio where the oscillation energy maximizes. The first difference to observe between the two graphs in Figure 5.21 is the critical pressure ratio value. High energy oscillations maximize at $P_i/h_w \approx 2.2$ (for $L/H=8.4$) instead of 1.15 as was identified earlier for L/H=27. This is in accordance with several observations made throughout the tests. More specifically, it was noted that very high oscillation amplitudes existed at a particular pressure ratio (by changing only the internal pressure). At higher or lower pressure ratio values

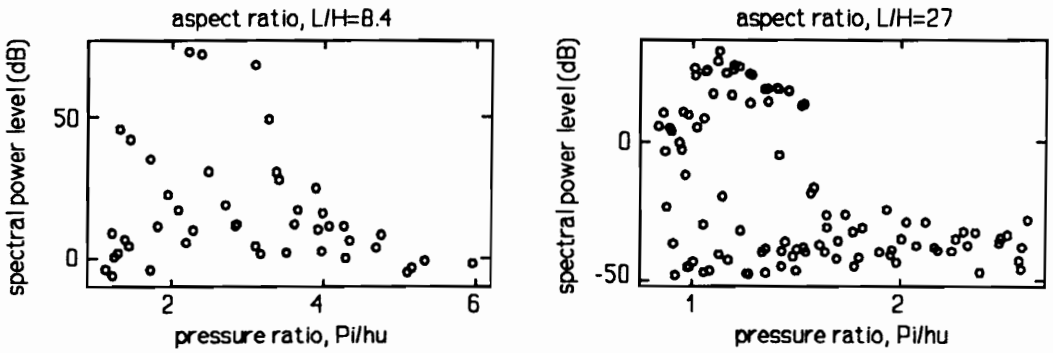

Figure 5.21 Comparison of the energy of oscillation between different aspect ratios, with respect to the pressure ratio parameter.

these high oscillations would dampen but they were eliminated only at higher pressure ratios. The same phenomenon was not visible in the L/H=27 aspect ratio case, because the flow capacity was not high enough to drive the dam to very high oscillation amplitudes. Since flowrate is directly related with the load ratio, it is necessary to look at the load ratio relationship as well.

The graphs in Figure 5.22 show an expected increasing trend in the energy of oscillation with an increase of the load ratio. This is simply interpreted that the higher the upstream water head the higher the vibration energy is. The same conclusion was reached in Chapter Four and

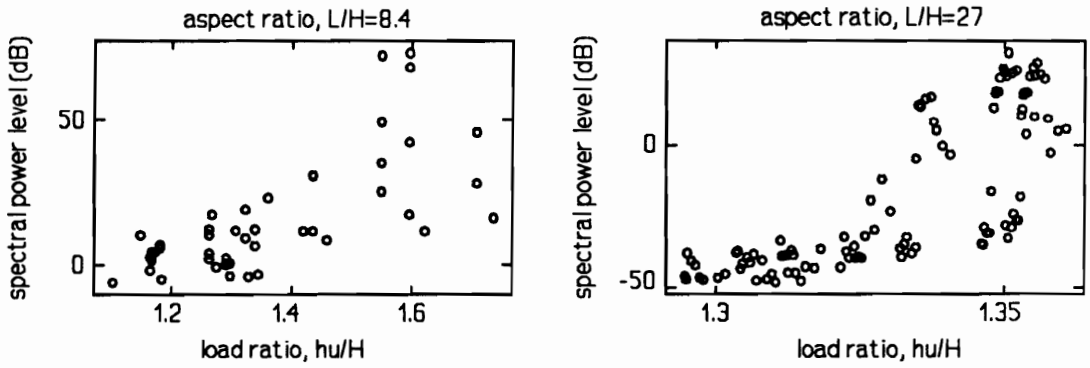

Figure 5.22 Comparison of the energy of oscillation between different aspect ratios, with respect to the load ratio parameter.

it was credited to the increase of the system's mass. Considering that both models have approximately equal heights, it is not surprising that for the L/H=8.4 aspect ratio (where failures occurred) the load ratio is higher. It appears that for failure to occur it requires a critical load ratio

between 1.55 and 1.6 or higher (given the critical pressure ratio). Although actual failure is dependent on a wide range of material characteristics, in this type of problem failure is also associated with high oscillation amplitudes. Therefore, it is fair to claim that such amplitudes will occur at a critical load ratio h_u/H=1.55 and thereafter. This type of response is two-dimensional and dams that can exhibit a 3D response (like those with L/H=27) may have lower critical load ratios. It must be clarified that a critical pressure ratio exists for every load ratio (that is why there is an oscillatory trend in Figure 5.22, better shown in Figure 5.14).

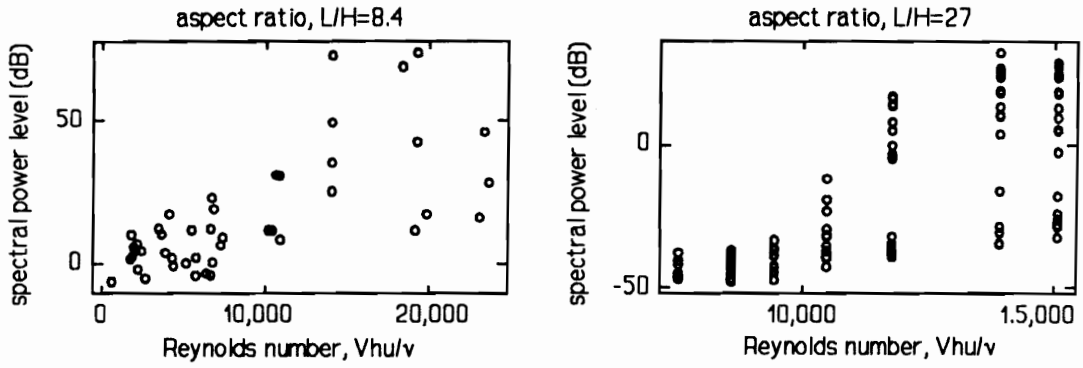

Figure 5.23 Comparison of the energy of oscillation between different aspect ratios, with respect to the Reynolds number, **Re**=Vh_u/ν.

Since the upstream head alone does not adequately describe the flow conditions as the Reynolds or Froude number would, it is appropriate to show the energy of oscillations pattern with respect to those parameters as well. The graphs in Figure 5.23 show the same trend. In fact, the left graph complements the right graph. It was mentioned earlier (in a previous section) that

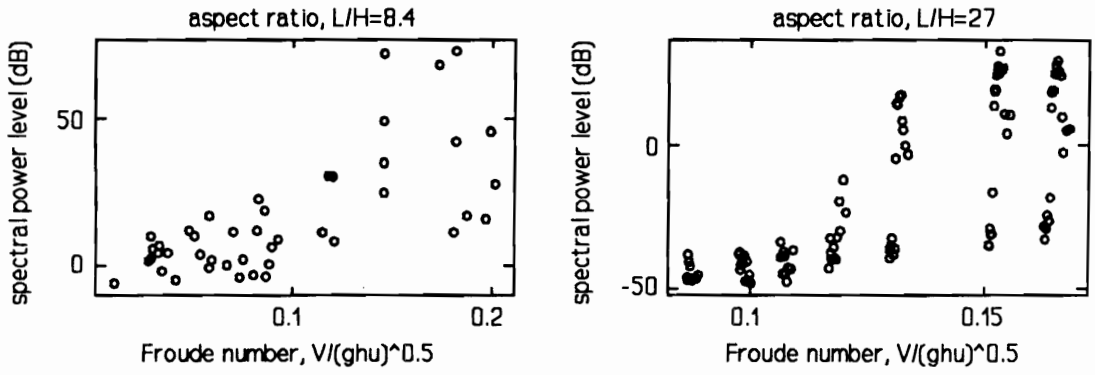

Figure 5.24 Comparison of the energy of oscillation between different aspect ratios, with respect to the Froude number, **Fr**=$V/(gh_u)^{1/2}$.

there are probably two plateaus in the Reynolds number relation to the energy of oscillations, with the upper plateau starting around **Re**=14,000. This holds true for both graphs. In this respect the graphs showing the Froude number relationship in Figure 5.24, produce a similar picture. The critical Froude number in this case is approximately **Fr**=0.15, for both cases as well.

Concluding, the critical numbers (where the energy of oscillation maximizes) for pressure and load ratios depend on the aspect ratio L/H as well. On the other hand, the critical Reynolds number and Froude number are independent of the aspect ratio. These conclusions further amplify the choice made earlier to use the pressure ratio and load ratio for describing the dynamic characteristics of inflatable dams.

5.7 Water-Fill Effect

As mentioned in previous sections in various chapters, water-filled dams were used only for comparison purposes. Early during the preliminary tests it was identified that water-filled dams have one to two orders of magnitude higher oscillation amplitudes. It is for this reason alone that further tests on water-filled dams were discontinued.

During additional tests on the 1.82 meters (6 feet) long model, it was possible to measure a considerable decrease of the natural frequencies. In addition to the oscillations' energy level increase, it was possible to visualize traveling waves along the dam under impact excitation. This further solidified the air-inflated measurements which showed phase differences between measurements at specific loading conditions.

5.8 Vibration Control

Vibration control is considered to be the next logical step, after unwanted oscillations are observed in a structure. In the case of an inflatable dam, it is important to alleviate the small disturbances before the dam is put into a large-amplitude high-energy oscillation. This is a crucial point, since with the huge water-mass involved in a prototype scale, it will be impossible to stop an already progressed case of vibrations.

5.8.1. Stable Air-Pockets

Previous workers reported that full nappe aeration stabilizes an oscillating inflatable dam. Instead of an end-to-end aeration of the downstream base of the dam, air bubbles were introduced.

These bubbles created a series of stable air-pockets at the downstream base of the dam. This resulted in a complete stabilization of the dam, regardless of the internal pressure ratio and the current mode of vibration.

There were concerns regarding probable surface tension forces due to the small model scale. These concerns were addressed by adding liquid soap into the water channel and therefore any surface tension forces were eliminated. The only effect from the addition of the soap was a 10-20% reduction in the size of the air-pockets, which remained stable at the downstream base of the dam. Large volumes of soap-foam generated at the recalculation pipe outlet did not create any problems, as most of the foam was captured and diluted in the several upstream filters.

The air-pockets work as a buffer between the dam membrane and any random turbulent excitation. Moreover, they streamline the downstream side of the dam and otherwise flow separation phenomena do not exist. Either because flow separation is the driving force or the perturbation force, the result is that it does not exist any more. The method used here for vibration control may not be applicable in prototypes, but it helped to identify the flow disturbances at the downstream side of the dam to be the only cause of vibrations.

5.8.2 Internal Pressure Variations

Active control was not performed in this work. However, there is strong evidence from preliminary work, that controlling small internal pressure oscillations in the dam can damp its vibrations. In a prototype scale dam, it is unlikely that small internal pressure variations can actually stop large-amplitude vibrations. It is possible, however, to be able to stop small disturbances from driving the dam into large oscillations.

5.9 Comparison with Previous Work Done

There is no previous analytical or numerical work known that would consider the overflow case of inflatable dams. As mentioned in the "Literature Review" section of Chapter One, experimental work that was reported dealt with a 2D response, or simply it did not detect a 3D response. Moreover, the only work that considered mapping the high energy vibrations of inflatable dams (Baker *et al.* [15], 1965), provided only vague regions instead of specific points.

Nevertheless, an attempt is made here to compare the results of this work with Baker's results. An upscaling of the current work was done following the same steps as done for the "Free Vibration" cases in Chapter Four. Baker used the scale ratios L_r=20 and L_r=24, considering only

the dam's height. For dynamic similarity he used the Froude law, without any regard to the aspect ratio, L/H. The aspect ratios are estimated to be 3.75 and 12, and the results were applied to prototypes with aspect ratios in excess of L/H=20. This is inappropriate as shown in an earlier section, where the pressure ratio and load ratio critical values were seen to be dependent on the aspect ratio. In addition, Baker's results apply to water-filled dams, and their application to air-inflated dams is questionable.

The results of this work are converted to prototype values as found in Figure 4 [#]. Since the scale ratio for this work is actually a range of scale ratios, then the 6.7cm (0.22 feet) high model is scaled-up for a 3.05 meter (10 feet) high prototype. This results in a scale ratio L_r=45 which is somewhat beyond the possible scale ratio range (as explained in Chapter Four), if the aspect ratio L/H is taken into consideration. Based on Table 2.1 in Chapter Two, the flowrate ratio, Q_r (L^3T^{-1}), is

$$Q_r = L_r^{5/2} \tag{5.3}$$

The flow rate per unit length q_r ($L^3T^{-1}L^{-1}=L^2T^{-1}$) is therefore

$$q_r = \left(L^2T^{-1}\right)_r = L_r^2 L_r^{-1/2} = L_r^{3/2} \tag{5.4}$$

Therefore, the prototype flow rate per unit length of the model tests here, is up to q_p=71 cusecs per foot length compared with 166 cusecs per foot length of Baker's work. In his report it is shown that vibrations would start at 53 cusecs per foot length for well-pressurized water-filled dams, and 63 cusecs per foot length for dams with a small air quantity. Baker's vibration regions were also a function of another parameter equivalent to pressure ratio, as the results of this work.

Concluding, it can be said that the results here are incompatible with Baker's results, primarily due to the inflation medium (air versus water). Unfortunately there is no other experimental report known, on the dynamics of inflatable dams.

Chapter Six

CONCLUSIONS

This work presented some of the response characteristics of inflatable dam models under dynamic loading. Free vibrations were considered, with and without impounding water under impact excitation. Overflow conditions were studied under various flowrates. For the most part, the experiments dealt with a model long enough to exhibit longitudinal as well as cross-sectional behavior. The membrane material was chosen to have virtually no bending stiffness, and it was considered as an inextensible membrane. For most of the test cases the dams were air-inflated. Internal pressure and upstream velocity were the primary variables studied. The response of the dam was given in terms of its internal pressure variations.

6.1 Concluding Remarks

The most important response parameters of inflatable dams, were identified to be the *pressure ratio* and the *load ratio*. The pressure ratio is a measure of the ratio of the stiffness of the inflatable dam to the applied forces (P_i/h_u). The load ratio is a measure of the hydrostatic forces applied on the dam (h_u/H). Both ratios are non-dimensional parameters and therefore can be used for models and prototypes alike.

It was shown that there is a critical pressure ratio where the energy of oscillations maximizes. In addition, it was shown that this critical ratio is dependent on the aspect ratio L/H. There is an additional critical pressure ratio that signifies the entry of the dynamic system (structure and flow) into a high-energy oscillation range.

The pressure ratio was shown to be an important parameter. The frequency of oscillation under dynamic excitation is proportional[1] to the pressure ratio. The relation is slightly non-linear with a progressive rate proportional to the frequency. It has been identified that there is a critical pressure ratio in addition to those mentioned earlier where the longitudinal response maximizes its displacement amplitudes. These frequency components have higher harmonics and the energy level of each frequency fluctuates with the pressure ratio. Moreover, these higher harmonics showed a better linear relationship between the frequency of oscillation and the pressure ratio.

The vibration energy was identified to increase with the load ratio. The higher the load ratio, the higher the spectral energy. The relationship shows a progressively increasing oscillatory trend. This oscillatory trend is in fact related to the pressure ratio fluctuations. In other words, for a given load ratio there is a critical pressure ratio. If the load ratio is high enough and the pressure ratio is at its critical value, then catastrophic failure was shown to occur. The load ratio was also shown to be inversely proportional to the frequency of vibration.

It was possible to identify two modes of vibration, due to their large-amplitude displacement and the low frequency of oscillation. The first, in the 0.6 meters wide channel, was a cross-sectional back and forth motion, with an approximate angle of inclination to the horizontal of 20 to 40 degrees. It was during this mode of vibration that catastrophic failures occurred. The second mode of vibration was identified in the 1.8 meters wide channel as a longitudinal response. The shape of the dam was like a standing wave with a stable node at the middle and antisymmetric bows. It occurred at a pressure ratio lower than the critical one where maximum energy oscillations occurred.

The mechanics of vibrations were associated with the flow action at the downstream base of the dam. Two possible vibration mechanisms were suggested. The first considers the possibility of the flow action to be the driving force. The second considers the water action only as perturbation forces that tune the inflatable dam motion to its natural frequencies.

Hopefully this study will further enhance the understanding of the mechanics of inflatable dams, and that it will be considered another building block among the work done by previous workers. Inevitably, with this knowledge additional questions arise.

---

[1] The term "proportional" is used here with a loose definition. It does not imply a linear relationship, but only that the first parameter increases with an increment of the second parameter. Similarly for "inversely proportional".

6.2 Need For Additional Work

There are two main questions directly related with this work that were not answered. The first one seeks the mode shapes of the various natural frequencies shown. It is likely that the mode shapes do not remain the same throughout the frequency variations with respect to pressure ratio and load ratio variations. These variations were identified as "vibration modes" in a loose definition of the term.

The second question is related with the effect of material bending stiffness. There are inflatable dams already installed with some bending stiffness that cannot be ignored. The effect of such a material can be a significant reduction in the energy of oscillations, for given pressure ratios and load ratios.

Additional experimental parameters may be included in future experimental tests. The number of cases generated from all possible parameter combinations is enormous. Therefore, future research should look at one additional parameter at a time.

Appendix A

LIST OF SYMBOLS

The following is a list for most of the symbols used in this work. An effort was made to eliminate any concept conflicts by using non-traditional lettering. However, the subject itself being in between several disciplines (primarily Structures, Fluid Mechanics, and Instrumentation Science), is a natural consortium of conflicting symbols. Most of them are generally accepted in the format used here. In some occasions the same symbol is used for more that one concept. The explanation for each symbol is given repeatedly at key points in the document to avoid confusion, and enhance clarity. Greek characters are given in a separate list after the English characters. Some abbreviations are presented at the end of the symbols list.

A = general area, m^2 (ft^2)
= cross-sectional area of the channel normal to average velocity, m^2 (ft^2)
A_v = voltage gain (dimensionless)
C = discharge coefficient
= capacitance, μF, micro-farads
E = voltage differential, V, volts
$\mathbf{F}$ = any force vector
F = any force, N (lb)
f = general frequency, Hz
$\mathbf{Fr}$ = Froude number = $V/(gL)^{1/2}$ (dimensionless)
f_r = frequency ratio (dimensionless)
g = gravity acceleration constant = 9.81 m^2/s (32.16 ft^2/s)
H = height of the inflatable dam
H_f = height of the dam, free of loading
h_o = dam's overflow water head, m (ft)
h_u = upstream water head, m (ft)
k = general system's stiffness, N/m (lb/ft)

L = general length, m (ft)
= length of an inflatable dam, m (ft)
L_m = length of model dam, m (ft)
L_p = length of prototype dam, m (ft)
L_r = scale ratio or length ratio = L_p/L_m (dimensionless)
m = general mass = weight over acceleration of gravity, kg (slugs)
P = general pressure, N/m^2 (lb/ft^2 or psi)
p = general pressure, N/m^2 (lb/ft^2 or psi)
P_i = internal pressure water head = $p_i/\rho g$, m (ft)
p_i = dam's internal pressure, N/m^2 (lb/ft^2 or psi)
Q = flow rate, m^3/s (ft^3/s or cusecs)
q = flow rate per unit length (or unit width), m^2/s (ft^2/s or cusecs/ft)
R = gas constant, N·m/(kg·°K) or ft·lb/(slug·°R)
= radius, m (ft)
Re = Reynolds number = $LV/\nu = LV\rho/\mu$ (dimensionless)
R_g = ground or gain resistance, Ω, ohms
R_f = feedback resistance, Ω, ohms
St = Strouhal number = fL/V (dimensionless)
T = temperature, °C or °K (°F or °R)
V = general volume, m^3 (ft^3)
= mean velocity of the stream = Q/A, m/s (ft/s)

α = phase angle
= central angle of the circular membrane arc, rad
γ = specific weight, N/m^3 (lb/ft^3)
μ = absolute or dynamic viscosity, N·s/m^2 (lb·s/ft^2)
= non-dimensional parameter of the natural frequencies of analytical results
ν = kinematic viscosity = μ/ρ, m^2/s (ft^2/s)
π = 3.14159.... radian
ρ = density = γ/g, kg/m^3 (slug/ft^3)
ω = natural frequency, rad/s
ω_d = damped frequency, rad/s
ξ = damping ratio = c_s/c_{cr} = system damping over the critical damping (dimensionless)

h_u/H = load ratio (dimensionless)
L/H = aspect ratio (dimensionless)
mils = thousandths of an inch = 0.0254mm
mm = millimeters, thousandths of a meter
P_i/h_u = pressure ratio (dimensionless)
psi = pounds per square inch, 1psi = 27.69 inches (70.3cm) of water head
V = volts

Appendix B

BESSEL APPROXIMATION

It was mentioned in the Instrumentation chapter, that the acquired data were conditioned with active filters using Bessel approximation. This particular approximation was chosen because of its favorable dynamic characteristics. There are many possible functions and choosing the appropriate approximation requires many considerations. Here, the possible effects on the input signal will be shown to justify the use of the Bessel function.

B.1 Low-Pass Filter Approximations

The purpose of a filter is to eliminate an unwanted subset in a sample space. In this case the sample space is defined as the operational frequency bandwidth, and the subset is the frequency range to be suppressed (attenuated). In most applications an absolute elimination of the unwanted subset is not possible, thus, practical reduction is of our concern.

For a low-pass filter the approximation generally has a passband region, a transition region, and a stopband region. The cutoff point, ω_c, is defined as the point where the response magnitude is decreased by 3dB, or it is $2^{-1/2}$ times its initial value (Figure B.1). The function presented in Figure B.1 is a second order Butterworth approximation.

Low-pass filters can be realized with all-pole networks employing approximation functions such as the Butterworth, Chebyshev, Bessel, synchronously tuned, transitional (a compromise between Bessel and Chebyshev), and other. Elliptic function filters may also be used, who have poles as well as zeros at finite frequencies.

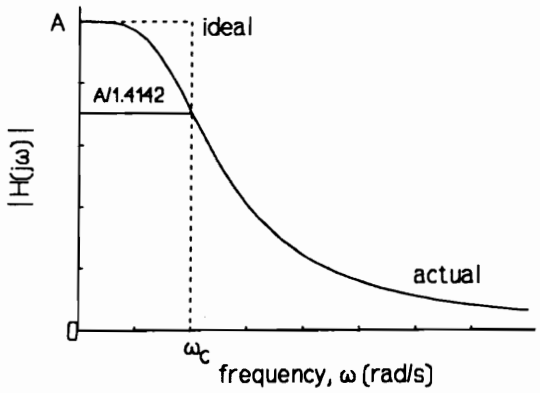

Figure B.1 Ideal low-pass filter comparison with a realizable approximation function.

A specific function is chosen based on the use of the filter. For example, the elliptic function filters offer the steepest rate of descent theoretically possible for a given number of poles. The use of finite transmission zeros in the stopband reduces the transition region dramatically. They have, however, a ripple behavior in the passband. Instead, a Butterworth filter is optimized for a maximally flat passband. Chebyshev has a much better cutoff characteristics than Butterworth, and Bessel is optimized for a maximally flat delay.

B.2 Response Characteristics

Ideally a filter has a linear phase response, zero loss in its passband and infinite loss in its stopband. A Butterworth filter has a maximally flat response curve in the passband. Such a flat response ensures an objective comparison between signals within the passband. Butterworth has inferior (to Chebyshev) cutoff characteristics, but it exhibits a better phase response. If a sharp cutoff is not critical but the phase response is of primary concern then neither should be used.

Bessel approximation filter is optimized to obtain a linear phase which results to a maximally flat time delay, $T(\omega)$. Therefore, all frequency components in the passband are delayed the same. Since the output signal is used for frequency components identification and phase shift measurements, a constant delay filter characteristic is critical. Bessel response to a step function has no overshoot (or ringing), and its response to an impulse input lacks an oscillatory behavior (characteristics useful for very high frequencies). One drawback is that its cutoff characteristics are inferior to any other approximation mentioned. This results to higher order filters which makes the electronic circuit design more demanding.

A Bessel filter transfer function, $H(s)$, of order n, employs the polynomial expression $B_n(s)$, where

$$H(s) = \frac{B_n(0)}{B_n(s)}$$

$$B_n(s) = s^n y_n(1/s) \ , \tag{B.1}$$

$s=j\omega$, and $y_n(s)$ is called a Bessel polynomial due to its relationship to the Bessel spherical functions $J_{\pm(n+1/2)}(x)$. An approximation to the Bessel transfer function is

$$H(s) = \frac{V_{out}(s)}{V_{in}(s)} = \frac{k}{s^n + b_{n-1}s^{n+1} + \ldots + b_1 s + b_0} \tag{B.2}$$

The denominator polynomial order defines the filter's order n. For a second order filter (n=2) b_0=b_1=3, and for a fourth order filter (n=4) then b_0=b_1=105 b_2=45 and b_3=10. Constant k usually takes a value so that the response function is unity at s=0.

Figure B.2 compares the Bessel approximation with the Butterworth and Chebyshev (with 0.5dB ripple in the passband) approximations. The responses are normalized to a cutoff frequency of unity ($\Omega=\omega/\omega_c$, where ω_c is the cutoff frequency). Bessel's phase response and time delay characteristics ($T(\omega)=d\phi/d\omega$) are shown to be superior as mentioned earlier. More details can be found in a large volume of references on the theory and design of filters [75-78].

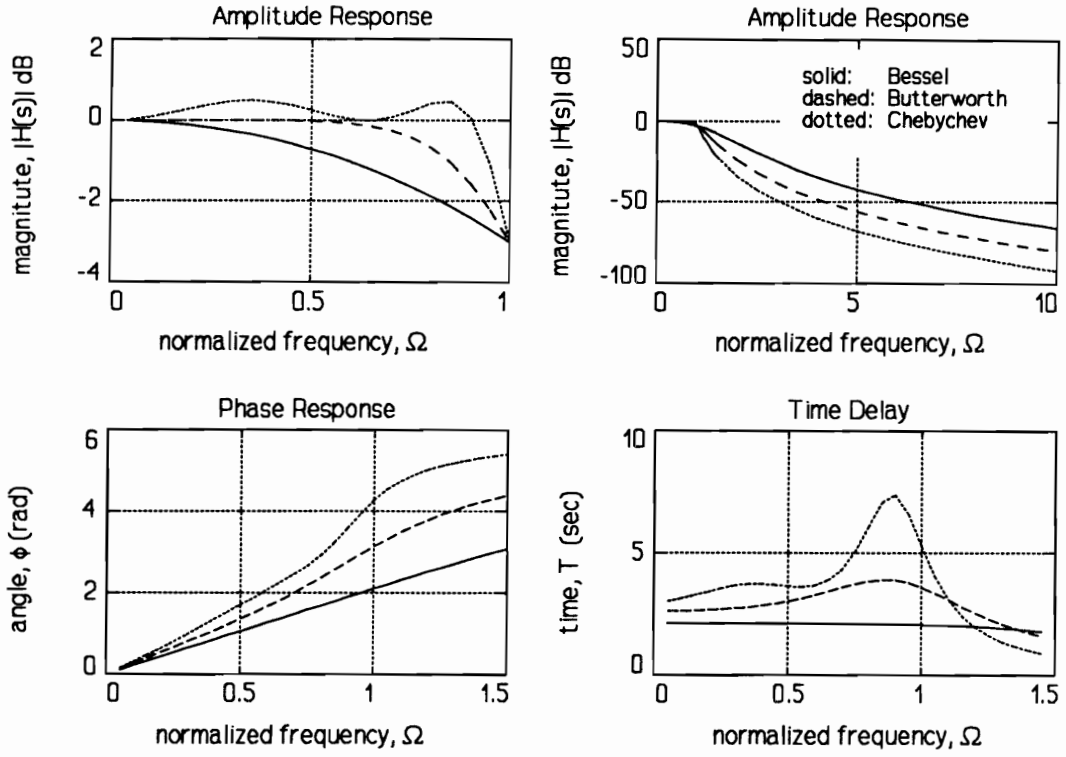

Figure B.2 Response characteristics of 4th order transfer functions with Bessel, Butterworth, and Chebyshev (0.5dB ripple) approximations.

Appendix C

IR DISPLACEMENT SENSOR

Considerable work was commissioned in the development of the Infra-Red displacement sensor/instrument. It employs an amplitude modulated Infra-Red (IR) columnized "light" sheet. An IR sensor detects the width of the IR beam. The output of the instrument (DC voltage) is proportional with the width of this beam. Therefore, by obstructing part of the IR beam with an oscillating structure, it is possible to describe the motion of that particular point of the structure in terms of the instrument's output voltage variations. Calibrating the instrument is relatively straight forward.

C.1 Design Description

The design of this instrumentation, is largely based on an IR pitch-angle measurement sensor by D. A. Walker and M. A. Walker [79] in 1988. Modifications were done to adjust the original design to the needs of this work. For an effective use of this sensor on inflatable dams research, the electronics have to be miniaturized to fit inside the model dam.

The receiver's circuit schematics is shown in Figure C.1. Beyond being an IR receiver, the circuit is also an oscillator and a signal amplitude modulator (AM). The latter is comprised by the quad-analog switch, the flip-flop circuit, and the signal splitter. In addition to that, signal conditioners are employed to clear and amplify the input voltage signal.

It is necessary to modulate the input signal so that unwanted light interference from tungsten bulbs, fluorescent tubes, or ambient sunlight is filtered out. This feature enables the

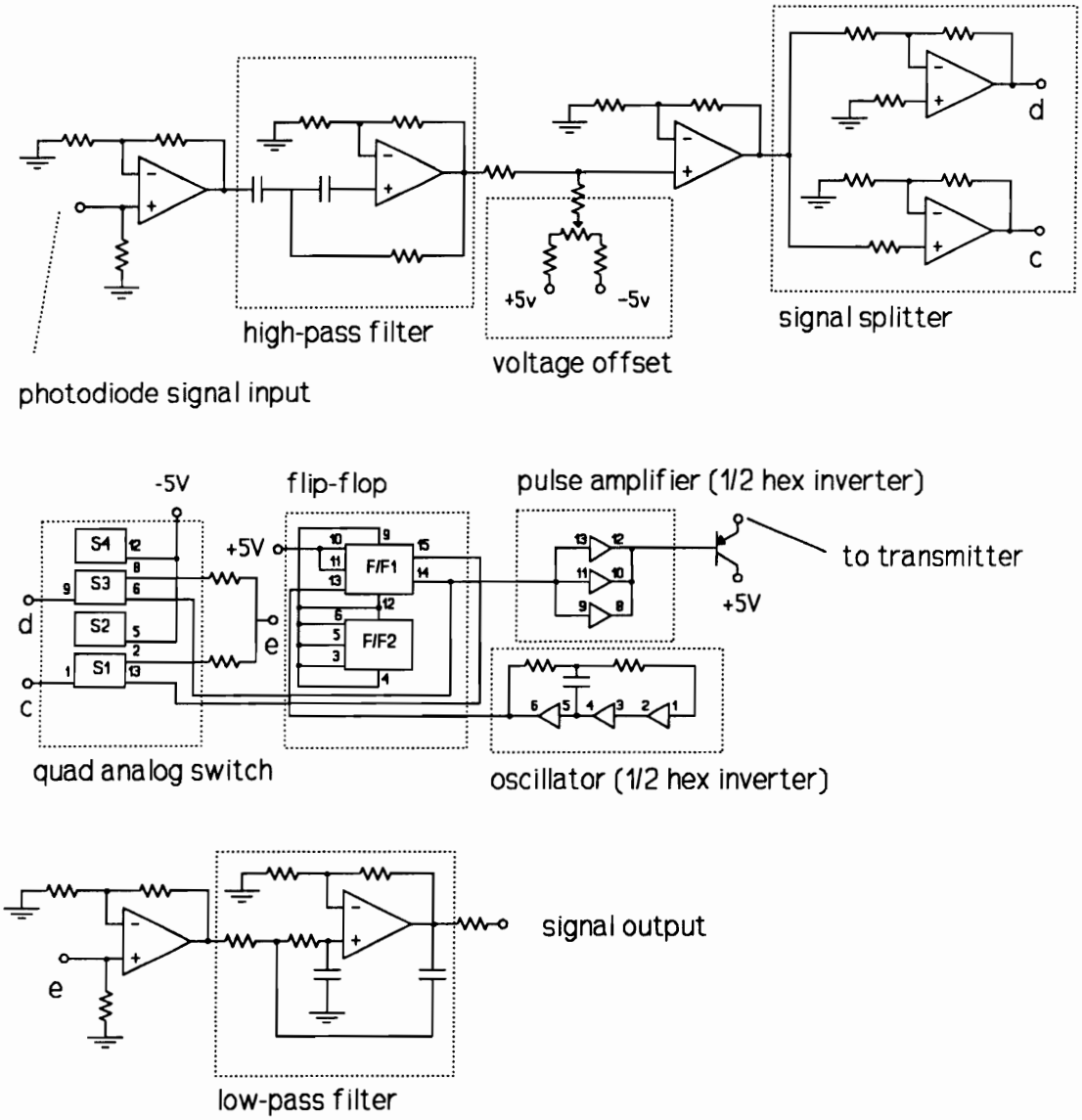

Figure C.1 Schematics of the Infra-Red displacement instrumentation receiver.

instrument to operate with the same calibration regardless the illumination conditions at various environments. The frequency of modulation is controlled by the oscillator circuit (use of the hex-inverter), a square wave function generator.

A high-pass filter overlapping a low-pass filter is used to minimize any interference, like the 60Hz AC noise from the power supply lines. The low-pass filter eliminates any interference from the high frequency modulator digital circuit, which may cross into the analog signal circuit. It is apparent that the modulation frequency must be high enough to allow the modulated signal

go through the high-pass filter without significant distortion. Most important, it allows the low-pass filter the space required to have a wide pass-range, but still have the modulation frequency well within its cutoff range. On the other hand, the modulation frequency should not be very high so that the performance of the instrument is not compromised by the individual component limitations. One way to attack this problem is to use more expensive high performance/reliability components.

The transmitter is driven with the same pulse signal that drives the signal modulation and receiver circuit. Therefore, the two circuits have simultaneous ON/OFF stages, a fundamental requirement for the instrument to operate. The transmitter is simply made by a current amplifier and an IR emitting diode. Using high frequency pulses has the additional advantage of allowing the IR emitter to operate with higher currents.

Both transmitter and receiver have voltage offset circuits for adjusting the signal away from the clamping voltage. Several operational amplifiers (including those used as filters) provide the necessary voltage amplification throughout the different stages. In order to avoid any unwanted digital interference, the analog circuits are separated from the digital circuits whenever possible.

C.2 Improvements Suggestions

Although the quality of the output signal may not be improved, the design may be simplified by including ready-made I.C. filters and amplitude modulators. This will definitely lead to the miniaturization requirement mentioned earlier, and enable the instrument to be located inside the inflatable dam models in a similar way the Hall-effect sensors were used.

Most of the circuit connections can be transferred on a printed circuit board (PCB). This will minimize any wire interferences due to wire overlaps and crisscrossing. Finally, better optics and refined adjustment mechanisms can definitely improve the instrument's performance.

REFERENCES

1. CE article (1992). "Rubber Dam Holds Water", ***Civil Engineering***, February, p. 88.

2. T. Kahl and S. Ruell (1989). "Rubber Dams as an Alternative to Flashboards", ***Marine and Industrial News, Bridgestone***, serial No. 27, pp. 16-23.

3. Bridgestone (1991). "Questions and Answers about the Bridgestone Rubber Dam", ***Bridgestone Engineered Products Co.***, July, pp. 30, 9, 11.

4. L. J. Connor (1969). "Fabridams-Their Application on Flood Mitigation Projects in New South Wales", ***ANCOLD Bulletin***, issue No. 29, October, pp. 56-65.

5. Firestone (1968). "Presenting the Imbertson Fabridam", ***Firestone Coated Fabrics Co.***, advertising brochure, p. 3.

6. N. M. Post and H. B. Stussman (1989). "Inflatable Rubber Makes Comeback", ***ENR***, September 14, pp. 30-31.

7. Imbertson (1993). Personal contacts, ***N. M. Imbertson and Associates***, Burbank, California.

8. Rodney Hunt (1992). "Rodney Hunt Company", advertisement brochure, 11905KPA, p.1.

9. J.-C. Hsieh (1988). "Free Vibrations of Inflatable Dams", ***Doctoral Dissertation, Virginia Polytechnic Institute and State University***, April, p. 5.

10. Bridgestone (1990). "International Supply Record of Bridgestone Rubber Dams", ***Bridgestone Engineered Products Co.***, April 25.

11. Sumitomo (1990). "'90 Complete List of Installations", ***Inflatable Rubber Gate Sumigate, Sumitomo Electric Industries, LTD., Hybrid Products Division***, CATFD-No. 16 (88.6).

12. Bridgestone (1993). Personal contacts, ***Bridgestone Engineered Products Co.***, August.

13. A. E. Wickham and P. K. McMahon (1969). "Proston Weir and Fabridam", ***ANCOLD Bulletin***, No. 29, October, pp. 66-74.

14. G. M. Binnie, A. R. Thomas and J. R. Gwyther (1973). "Inflatable Weir Used During Construction of Mangla Dam", ***Proceedings of the Institution of Civil Engineers***, Vol. 54, pp. 625-639.

15. P. J. Baker, D. H. Buxton and R. C. Worster (1965). "Model Tests on a Proposed Flexible Fabric Dam for the Mangla Dam Project, Pakistan", ***The British Hydromechanics Research Association***, R.R. 803 & 827, February.

16. M. P. Paidoussis (1965). "Pressure Waves in Horizontal Liquid Flexible Tubes", ***Journal of Mechanical Engineering Science***, Vol. 7, No. 4, pp. 380-390.

17. H. O. Anwar (1967). "Inflatable Dams", ***Journal of the Hydraulics Division, Proceedings of ASCE***, Vol. 93, No. HY3, May, pp. 99-119.

18. E. M. Shepherd, F. A. McKay and V. T. Hodgens (1969). "The Fabridam Extension on Koombooloomba Dam of the Tully Falls Hydro-Electric Power Project", ***The Journal of The Institution of Engineers, Australia***, Vol. 41, January-February, pp. 1-7.

19. C. van Beesten (1974). "Discussion of Inflatable Weir Used During Construction of Mangla Dam", ***Proceedings of the Institution of Civil Engineers***, Part 1, Vol. 56, pp. 189-191.

20. A. M. Stodulka (1974). "Discussion of Inflatable Weir Used During Construction of Mangla Dam", ***Proceedings of the Institution of Civil Engineers***, Part 1, Vol. 56, pp. 191-193.

21. A. Nemura (1986). "Dynamic Behavior of Inflatable Dams", ***Progress Report, Civil Engineering Department, Virginia Polytechnic Institute and State University***, February 14, pp. 2-3.

22. A. D. Alwan (1986). "Modal Analysis of Inflatable Dams Under Hydrodynamic Conditions", ***Proceedings of the 4th International Modal Analysis Conference***, Los Angeles, California, pp. 1502-1509.

23. A. D. Alwan (1988). "Modal Analysis of Flexible Structure Used for Flood Control", ***Proceedings of the 6th International Modal Analysis Conference***, Kissimmee, Florida, pp. 1180-1185.

24. L. H. McCarty (1990). "Inflatable Arm Segments May Lighten Shuttle's Manipulator System", ***Design News***, April 4, pp. 150-151.

25. H. O. Anwar (1971). "Discussion of the Analysis and Behavior of Inflatable Membrane Dams Under Static Loading", ***Proceedings of the Institution of Civil Engineers***, Vol. 48, pp. 131-137.

26. R. Watson (1985). "A Note on the Shapes of Flexible Dams", ***Journal of Hydraulic Research***, Vol. 23, No. 2, pp. 179-194.

27. H. B. Harrison (1970). "The Analysis and Behavior of Inflatable Membrane Dams Under Static Loading", ***Proceedings of the Institution of Civil Engineers***, Vol. 45, pp. 661-676.

28. K. Ogiwara, T. Tateishi and G. Furuya (1970). "The Shape of the Rubber Dam", ***Proceedings of the Japan Society of Civil Engineers***, (in Japanese), Vol. 179, No. 7, pp. 37-47.

29. A. M. Binnie (1973). "The Theory of Flexible Dams Inflated by Water Pressure", ***Journal of Hydraulic Research***, Vol. 11, No. 1, pp. 61-68.

30. R. D. Parbery (1976). "A Continuous Method of Analysis for the Inflatable Dam", ***Proceedings of the Institution of Civil Engineers***, Part 2, Vol. 61, December, pp.725-736.

31. R. D. Parbery (1978). "A Continuous Method of Analysis for the Inflatable Dam", ***Proceedings of the Institution of Civil Engineers***, Part 2, Vol. 61, December, pp.725-736.

32. N. M. Hitch and R. Narayanan (1983). "Flexible Dams Inflated by Water", ***Journal of Hydraulic Engineering***, ASCE, Vol. 109, No. 7, July, pp. 1044-1048.

33. R. H. Plaut and T. D. Fagan (1988). "Vibrations of an Extensible, Air-Inflated, Cylindrical Membrane", ***Journal of Applied Mechanics***, ASME, Vol. 55, September, pp. 672-675.

34. R. H. Plaut and M. J. Leeuwrik (1988). "Non-Linear Oscillations of an Inextensible, Air-Inflated, Cylindrical Membrane", ***International Journal of Non-Linear Mechanics***, Vol. 23, No. 5/6, pp. 347-353.

35. J.-C. Hsieh, R. H. Plaut and O. Yucel (1989). "Vibrations of an Inextensible Cylindrical Membrane Inflated with Liquid", ***Journal of Fluids and Structures***, No. 3, pp. 151-163.

36. J.-C. Hsieh and R. H. Plaut (1990). "Free Vibrations of Inflatable Dams", ***Acta Mechanica***, No. 85, Springer-Verlag,pp. 207-220.

37. R. H. Plaut (1990). "Parametric Excitation of an Inextensible, Air-Inflated, Cylindrical Membrane", ***International Journal of Non-Linear Mechanics***, Vol. 25, No. 2/3, pp. 253-262.

38. W. Szyszkowski and P. G. Glockner (1985). "Finite Deformation and Stability Behavior of Cylindrical Membranes Subjected to Symmetric Line Loads", ***International Journal of Non-Linear Mechanics***, Vol. 20, No. 3, pp. 177-198.

39. V. Firt (1983). "Statics, Formfinding and Dynamics of Air-Supported Membrane Structures", The Hague: Martinus Nijhoff.

40. H. Demiray and M. Levinson (1972). "The Long Fluid Storage Bag; a Contact Problem for a Closed Membrane", ***International Journal of Mechanical Sciences***, Vol. 14, pp. 431-439.

41. C.-Y. Wang and L. T. Watson (1981). "The Fluid-Filled Cylindrical Membrane Container", ***Journal of Engineering Mathematics***, Vol. 15, No. 2, April, pp. 81-88.

42. D. J. Malcolm and P. G. Glockner (1981). "Collapse by Ponding of Air-Supported Spherical Caps", ***Journal of the Structural Division***, Proceedings of the ASCE, Vol. 107, No. ST9, September, pp. 1731-1742.

43. C.-Y. Wang (1984). "The Filling of a Long Membrane Container", ***Journal of Structural Mechanics***, Vol. 12, pp. 1-11.

44. R. Maaskant and J. Roorda (1985). "Stability of Cylindrical Air-Supported Structures", ***Journal of Engineering Mechanics***, ASCE, Vol. 111, No. 12, December, pp. 1487-1501.

45. V. Namias (1985). "Load-Supporting Fluid-Filled Cylindrical Membranes", ***Journal of Applied Mechanics***, ASME, Vol. 15, pp. 1-6.

46. W. Szyszkowski and P. G. Glockner (1987). "On the Statics of Large-Scale Cylindrical Floating Membrane Containers", ***International Journal of Non-Linear Mechanics***, Vol. 22, No. 4, pp. 275-282.

47. M. D. Thomas and A. D. D. Craik (1988). "Three-Wave Resonance for Free-Surface Flows Over Flexible Boundaries", ***Journal of Fluids and Structures***, Vol. 2, pp. 323-338.

48. R. D. Blevins (1990). ***Flow-Induced Vibration***, Van Nostrad Reinhold, New York, pp. 67, 132, 48.

49. J. C. Kotz and K. F. Purcell (1987). "Synthetic Polymers: Plastics, Fibers, and Elastomers", ***Chemistry and Chemical Reactivity***, Saunders College Publishing, Philadelphia, pp. 933-941.

50. R. L. Daugherty, J. B. Franzini and E. J. Finnemore (1985). i) "Similitude and Dimensional Analysis", ii) "Fluid Measurements", ***Fluid Mechanics with Engineering Applications***, eighth edition, McGraw-Hill Co., pp. 185-202, 407.

51. Du Pont (1990). ***MYLAR LB Polyester Film, Summary of Properties***, #195067A, Du Pont Polymers, October.

52. Du Pont (1987). ***Mylar Polyester Film, Safety in Handling and Use***, #E-60737, Du Pont Polymers, November.

53. W. C. Percival (1990). ***Material Safety Data Sheet***, #MYL001A, E. I. Du Pont De Nemours & Co., January, pp. 1-4.

54. P. M. Gerhart and R. J. Gross (1985). "Organizing the Experimental Approach to Flow Problems: Dimensional Analysis", ***Fundamentals of Fluid Mechanics***, July, Addison-Wesley Co., pp. 343-400.

55. G. F. Round and V. K. Garg (1986). "Open Channel Flows", ***Applications of Fluid Dynamics***, Edward Arnold Ltd., Great Britain, pp. 283-318.

56. R. H. Sabersky, A. J. Acosta, and E. G. Hauptmann (1989). "Similitude", ***Fluid Flow A First Course in Fluid Mechanics***, third edition, Macmillan Publishing Co., pp. 145-153.

57. P. A. Kolkman (1989). "Models for Study of the Dynamic Behavior of Structures in Flow and Waves", ***Recent Advances in Hydraulic Physical Modelling***, R. Martins editor, NATO ASI Series, series E: Applied Sciences - Vol. 165, Kluwer Academic Publ., pp. 65-100.

58. W.-J. Yang (1989). "Introduction", ***Handbook of Flow Visualization***, W.-J. Yang editor, Hemisphere Publishing Co., p. 4.

59. D. N. Roy (1988). "Steady Flow in Open Channels", ***Applied Fluid Mechanics***, Ellis Horwood LTD, Chichester, p. 185.

60. J. J. Carr (1986). ***Elements of Electronic Instrumentation and Measurement***, second edition, Prentice Hall, pp. 224-276.

61. G. H. Olsen, revised by F. M. Mimms III (1980). "", ***The Beginner's Handbook of Electronics***, Prentice Hall, pp. 86-113, 123-128.

62. J. J. Carr (1983). ***Linear IC/OP Amp Handbook***, TAB Books Inc.

63. Burr-Brown (1992). "Instrumentation Amplifiers", ***Integrated Circuits Data Book Supplement***, vol. 33c, Burr-Brown Corp., pp. 3.1-3.121.

64. NSC (1993). "Instrumentation Amplifiers", ***Operational Amplifiers Databook***, National Semiconductor Corp., pp. 4.3-4.11.

65. Motorola (1983). "Amplifiers", ***Linear/Interface Integrated Circuits***, series D, Motorola Inc., pp. 3.236-3.242.

66. A. B. Williams and F. J. Taylor (1988). "Selecting the Response Characteristics", ***Electronic Filter Design Handbook, LC, Active and Digital Filters***, second edition, McGraw-Hill, pp. 2.1-2.79.

67. H. M. Berlin (1985). "Multivibrators", ***Digital Electronics. Fundamentals, Applications, and Experiments***, Prentice-Hall Co., pp. 103-142.

68. T. Economides (1989). ***Modal Analysis of a Damaged Structural Frame***, Master's Thesis, University of Mississippi, August.

69. EXAR (1992). "Telecommunication Products", ***EXAR Databook***, EXAR Corp., pp. 2.297-2.301.

70. D. J. Ewins (1986). ***Modal Testing: Theory and Practise***, Research Studies Press LTD., England, Bruel & Kjaer.

71. M. Paz (1985). "Logarithmic Decrement", ***Structural Dynamics Theory & Computation***, second edition, Van Nostrand Reynhold Comp. Inc., pp. 29-32.

72. W. Weaver Jr., P. R. Johnston (1984). ***Finite Elements for Structural Analysis***, Prentice Hall Inc., pp. 41-42.

73. T. D. Fagan (1987). ***Effect of Membrane Weight on Vibrations of Air-Inflated Dams***, Master's Thesis, Virginia Polytechnic Institute and State University, March.

74. J.-C. Hsieh (1988). ***Free Vibrations of Inflatable Dams***, Doctoral Dissertation, Virginia Polytechnic Institute and State University, April.

75. A. B. Williams and F. J. Taylor (1988). ***Electronic Filter Design Handbook, LC, Active, and Digital Filters***, second edition, McGraw-Hill.

76. W.-K. Chen (1986). ***Passive and Active Filters Theory and Implementations***, John Willey & Sons.

77. J. L. Hilburn and D. E. Johnson (1979). ***Manual of Active Filter Design***, second edition, McGraw-Hill.

78. D. E. Johnson (1976). ***Introduction to Filter Theory***, Prentice Hall.

79. D. A. Walker and M. A. Walker (1988). "Optical Pitch Angle Measuring System", personal notes, August.

VITA

T. A. Economides was born in Nicosia, Cyprus, in October of 1964. He holds a Civil Engineering Diploma from the Higher Technical Institute of Nicosia-Cyprus (June 1987), a Bachelor's degree in Civil Engineering (August 1988), and a Master of Science in Engineering-Civil Engineering (August 1989) from the University of Mississippi. His Master's thesis dealt with experimental structural dynamics, modal analysis, and finite element development towards damage identification of open cracks in steel structures. He has experience as a construction engineer and reinforced-concrete design engineer, from the H.T.I.'s co-op program and from post-master's professional experience. He joined the Department of Civil Engineering (Structures Division), at Virginia Polytechnic Institute and State University for his doctoral work, and he worked in the Department of Engineering Science and Mechanics as a research assistant. He will continue his research in the area of inflatable dams as a post-doctoral research associate, in the Department of Civil Engineering and the Department of Engineering Science and Mechanics. Economides' mailing address for the near future will be P.O. Box 722, Blacksburg, Virginia 24063-0722.

T. A. Economides